

**COMPARISON OF MODEL
INFRARED AND SOLAR FLUXES WITH
AIRCRAFT-BASED RADIOMETER MEASUREMENTS**

by

ILANA RACHEL STERN
B. S., University of Maryland
(1984)

SUBMITTED TO THE DEPARTMENT OF
EARTH, ATMOSPHERIC, AND PLANETARY SCIENCES
IN PARTIAL FULFILLMENT OF THE REQUIREMENTS
FOR THE DEGREE OF

MASTER OF SCIENCE IN METEOROLOGY

at the

MASSACHUSETTS INSTITUTE OF TECHNOLOGY
September 1988

© Massachusetts Institute of Technology 1988

Signature of Author _____
Department of Earth, Atmospheric, and Planetary Sciences
September, 1988

Certified by _____
Reginald E. Newell
Thesis Supervisor

Accepted by _____
Thomas H. Jordan
Chairman, Departmental Committee on Graduate Students

Lindgren
WITHDRAWN
FROM

CONTENTS

Abstract	4
1. Introduction	5
2. A brief description of the radiometers	9
2.1 The infrared radiometer	9
2.2 The solar radiometer	10
3. Description of the model	11
3.1 Introduction	11
3.2 Thermal infrared region	13
3.3 Solar region	16
3.4 Modifications to the model for this comparison	19
Figures	21
4. Data	24
4.1 Introduction	24
4.2 Temperature and water vapor profiles	25
4.3 Ozone profiles	26
4.4 Cloud profiles	28
Figures	30
5. Sensitivity of the model	43
Figures	46
6. Comparison of computed and measured fluxes	56
6.1 A first comparison	56
6.2 Comparison over maximum cloud	59
6.3 Less dense cloud	64
6.4 The clear air flight	64
Figures	65
7. Concluding remarks	90

Acknowledgements	93
References	94

COMPARISON OF MODEL INFRARED AND SOLAR FLUXES WITH
AIRCRAFT-BASED RADIOMETER MEASUREMENTS

by

ILANA RACHEL STERN

Submitted to the Department of
Earth, Atmospheric, and Planetary Sciences
in September, 1988 in partial fulfillment of the requirements
for the Degree of Master of Science in Meteorology

ABSTRACT

Radiative fluxes obtained from a numerical model were compared with those obtained from aircraft-based radiometers. Separate comparisons were made for thermal infrared (wavelength $\lambda > 2.9\mu$) and solar ($2.9\mu > \lambda > 0.6\mu$) radiation. The model ignores atmospheric scattering, and assumes that H_2O , CO_2 , O_3 and O_2 are the only absorbers. Clouds are assumed to be black bodies in the thermal region, while in the solar region they are assumed to be non-emitting and partially reflecting. The radiometer data were taken from four flights of the high-altitude ER-2 aircraft during the STEP experiment in Darwin, Australia in January 1987. Both radiometers had hemispheric fields of view. The infrared instrument recorded both upward and downward flux, from which the net upwelling flux was calculated; only the upwelling component of the net flux was obtained from the solar instrument.

The model results correspond to the measured thermal infrared and solar fluxes in a cloudy atmosphere to within instrument error. A solar value computed for a cloudless atmosphere was low compared to the single set of measurements taken in clear skies; this could be due to either unreported low cloud, or a low assumed albedo.

1. Introduction

Solar radiation is the prime energy source of the atmosphere. Climate changes perturb the structure and composition of the atmosphere, which alters its radiative response. In order to understand the consequences of such changes, it is important that the radiative processes be accurately modeled. Over the past 80 years, meteorologists have constructed increasingly sophisticated models of radiation exchange in the atmosphere. These models have been used in many studies of the global radiation balance (e.g. London and Sasamori, 1971, and Dopplnick, 1972) and in speculative studies on the effects of major changes in atmospheric composition, such as the doubling of CO₂ (e.g. Manabe and Weatherald, 1967, and Newell and Dopplnick, 1970). Measurements of radiative flux at several levels within a column can be used to calculate local radiative heating rates. Because radiative flux measurements (other than upwelling radiation measurements from satellites) are not regularly made, some studies have cited heating rates from computed fluxes as evidence for possible rising motion (e.g. Doherty et al, 1984).

Because of this wide usage of radiative transfer models, it is important that some assessment of their accuracies be made. A project to compare various models, the Intercomparison of Radiation Codes in Climate Models (ICRCCM), was initiated in 1984. Preliminary results from ICRCCM, for a prescribed cloudless atmosphere, show generally good agreement among models which explicitly account for the contribution to the transmission function from each absorption line (Luther et al, 1988). Fluxes from less detailed models, which average over bands of absorption lines, vary

by 10-20 percent. ICRCCM is currently doing another intercomparison which includes the effects of clouds. ICRCCM also compared a single observed profile from an aircraft-based radiometer with a subset of the radiation models and found good agreement at pressures greater than 500 mb, but large differences between measured and calculated upward fluxes at lower pressures (Luther, et al). This result, along with the spread of differences among the models, suggests that intercomparison between radiative transfer programs is not enough; for a comprehensive evaluation of these models, they must be compared to observations of radiative fluxes in the real atmosphere.

The present study is a comparison of radiative fluxes obtained from a numerical model with those obtained from aircraft-based radiometers. It should be stated from the outset that neither the observational data nor the calculated values can be considered "truth".

The numerical model used here is Dopplick's (1970) program, which was based on previous work by Rodgers (1967) and Kennedy (1964). The Dopplick model was included in the ICRCCM study; the fluxes calculated with this model are within a few percent of the median value for models of the same type (band models) for all of the various model atmospheres used. There are several reasons for critical examination of the applicability of its results. First of all, because of the complicated nature of the radiative transfer equations, and the many integrations required, a number of approximations and simplifications were incorporated into the model. Some of these approximations have been justified by other workers,

but others are clearly inappropriate to the real atmosphere (discussion of the validity of the various approximations will be deferred until Section 3). Secondly, the model can only be as good as its input data. Although radiosondes provide the fairly complete (albeit coarse) picture of the vertical temperature and water vapor structure required by the model, it must be remembered that radiosonde profiles are not truly spatially or temporally homogeneous. Also, the inclusion of clouds introduces large uncertainties; the optical properties of clouds are highly variable and not necessarily related to geometric thickness. Neither the geometric nor optical thickness is easily inferred from visual observation. Even if the actual cloud properties were known precisely for a given atmospheric profile, the model might not be able to take advantage of that information because the treatment of clouds in the model is very crude.

The largest errors in the model's calculations are due to the simplified cloud model used (Hoffman, 1981). Because of this, discrepancies between computed and observed fluxes due to other approximations (e.g., no scattering or absorption by aerosol) will be masked, both by the effects of assuming cloud heights and thicknesses which may be different from those of the actual clouds, and by the effects of the assumptions made about the cloud optical properties. For this reason, not much will be said about the non-cloud-related approximations, since their effects can only be assessed from comparisons in cloudless atmospheres, and nearly all the data used was from cloudy days.

Unfortunately, it was discovered in an earlier version of this study that the available radiometer observations are not accurate enough to use as benchmarks for a radiative transfer model. Early radiation measurements were tested against flux obtained from radiation charts, which had the advantage of simplicity, but made many approximations. Comparisons such as those by Brewer and Houghton (1956) and Suomi et al (1958) found good agreement with these charts. Advances in computing technology have led to very sophisticated models; measurement technology has not made such rapid improvement, and errors in measured fluxes are still very large.

For this reason, the present study cannot really assess the accuracy of the Dopplick radiation model. Nevertheless, these results can serve as guidelines for the appropriateness of its usage.

2. A brief description of the radiometers

2.1 The infrared radiometer

The infrared fluxes used in this report are obtained from the hemispheric field of view radiometer which was located on the right wing of a high altitude research aircraft, the NASA ER-2. The optical heads of the instrument are rotated in flight, and take data when facing directly up or directly down. The net flux is the difference between the measurements in the up (measuring downwelling flux) and down (measuring upwelling flux) positions. Because the position of the instrument is fixed with respect to the aircraft, the data are only reliable when taken while the plane is flying horizontally. The measurements presented here are for stepped profiles; legs flown at constant altitudes are connected by rapid, steep ascents or descents. The ER-2 banks sharply in turns, however, and this may lead to fluctuations on apparently horizontal flight legs.

The radiometer is sensitive to radiation from approximately 2.9μ to 50μ ($1\mu = 10^{-6}$ meter); the transmission rolloff on the long wavelength end extends from about 35μ to 60μ . The data were adjusted to yield effective fluxes from 2.9μ to infinity. The major contributor to errors in the measurements is uncertainty about the exact shape of the long wavelength rolloff, which could cause errors of about 10%. Other sources of error are the measurement of the internal instrument temperature (used to determine the contribution of thermal emission within the instrument) and calibration errors. The resulting uncertainty in the data from all sources of error is estimated at 15%.

2.2. The solar radiometer

The solar fluxes used in this report are obtained from a solar radiometer with a hemispheric field of view, which was located on the underside of the fuselage of the ER-2. This instrument measures upwelling flux; a similar instrument on the top of the aircraft measures downwelling flux, but calibration problems prevented the release of its data. For this reason, no net solar flux measurements are available. As with the infrared instrument, this radiometer is fixed with respect to the aircraft, and therefore the data are not useable when the plane is turning or changing altitude.

The radiometer is sensitive to radiation from approximately 0.6μ to 2.9μ . Here again, the transmission rolloffs at the edges of the band pass are not precisely known. The detector also exhibits some azimuthal dependence on the direction of the incident radiation field because the instrument is not optically symmetric. No laboratory calibration measurements were made for the solar radiometers; the instruments will ultimately be calibrated from the navigation data, but an algorithm has not yet been developed. The uncertainty in the data from all sources of error is expected to be about 30%.

3. Description of the model

3.1 Introduction

The Dopplick model has been extensively documented by Hoffman (1981); only the basic features of the program's code are discussed here. The program version used in this study is essentially the same as the one described by Hoffman.

The model calculates the net radiative flux, and the heating rate due to flux divergence, at various specified levels in a model plane-stratified, nonscattering atmosphere. Thermal (terrestrial) and solar radiation are handled separately; solar radiation is in turn split into the visible (up to 0.76μ) and near infrared (0.76μ to 6.3μ) regions. In the thermal region, the absorbing gases considered are H_2O , CO_2 , and O_3 . H_2O absorbs broadly across this region, with a series of rotational bands between 0 and 1000 cm^{-1} , the dimer continuum from 720 to 1200 cm^{-1} , and a vibrational band centered on 6.3μ . (The spectral widths of the absorption bands in the model are given in wavenumber (ν) rather than wavelength (λ), where $\nu = \lambda / 0.01$.) The other important absorption bands in this region are the 15μ CO_2 band and the 9.6μ O_3 band. The solar visible region is treated as a single band in which O_3 is the only absorber. In the solar near infrared, the most important absorbers are H_2O and CO_2 , which have many absorption bands in this region, and O_2 , which absorbs in a narrow band centered on 0.76μ . Table 3.1 summarizes the spectral bands for which absorption is calculated, and the absorber(s) in each band.

CO_2 and O_2 are assumed to be evenly mixed throughout the atmosphere; vertical profiles of the concentrations of H_2O and O_3

Table 3.1. Spectral intervals used in the Dopplick radiation model for radiative transfer calculations. The first group of intervals is used for thermal calculations. The second group of intervals is considered near infrared by the model, but their contributions are added to the thermal bands for this study because the radiometer bandwidth extends to 2.9 μ . The third group is used for the solar region.

Absorption band	Spectral range (cm ⁻¹)
H ₂ O rotational	0 - 1000 (13 subintervals)
(H ₂ O) ₂ continuum	720 - 1200 (5 subintervals)
H ₂ O 6.3 μ	1200 - 2200 (9 subintervals)
CO ₂ 15 μ	567 - 767
O ₃ 9.6 μ	970 - 1110
CO ₂ 5.2 μ	1850 - 1970
CO ₂ 4.8 μ	1970 - 2200
CO ₂ 4.3 μ	2200 - 2600
H ₂ O 3.3 μ	2600 - 3340
CO ₂ 2.7 μ	3400 - 3860
H ₂ O 2.7 μ	3340 - 4600
CO ₂ 2.0 μ	4700 - 5300
H ₂ O 1.9 μ	4600 - 6100
CO ₂ 1.6 μ	6100 - 6500
CO ₂ 1.4 μ	6800 - 7200
H ₂ O 1.38 μ	6500 - 8200
H ₂ O 1.1 μ	8200 - 10000
H ₂ O 0.9 μ	10000 - 11500
H ₂ O 0.8 μ	11500 - 13000
O ₂ 0.76 μ	13000 - 13250
O ₃	> 13250

must be specified as program input. The model also requires the vertical profile of temperature, and the upper and lower boundaries, percent sky coverage, and optical properties of each cloud layer.

3.2 Thermal infrared region

The net flux of thermal radiation is obtained by integrating the radiative transfer equation over angle, frequency, and height. The intensity of radiation I_ν at a frequency ν traversing a path ds is described by

$$\frac{dI_\nu}{k_\nu \rho ds} = J_\nu - I_\nu$$

where J_ν is the source function and k_ν is the mass extinction cross section (as scattering is neglected here, this is equal to the mass absorption cross section). Integration over height and angle, for a plane stratified, nonscattering atmosphere, gives the equation for upward flux of radiation at the frequency ν at some level z_2 :

$$\frac{1}{\pi} F_\nu^\uparrow(z_2) = I_\nu(z_1) T_\nu(z_2, z_1) + \int_{z_1}^{z_2} J_\nu(z) \frac{dT_\nu(z_2, z)}{dz} dz \quad (1)$$

where level z_1 is below level z_2 . F^\uparrow is the upward flux (the hemispheric integral of the vertical component of I_ν); $T_\nu(z_2, z)$ is the angle integrated transmission function for radiation reaching z_2 from z , and is a function of k_ν . In the Dopplick model, the angle integration is not carried out; transmission functions for direct radiation are used, with the absorber amounts multiplied by Elsasser's diffusivity constant, $\beta = 1.66$. This approximation is discussed by Rodgers and Walshaw (1966).

The integration over frequency is approximated by a summation over several spectral intervals over which $I_\nu(z_2)$ and $J_\nu(z)$ are assumed constant. If there are R intervals $\Delta\nu_r$ the average transmission function in the r (th) interval is defined

$$\bar{T}_r(z_2, z) = \frac{1}{\Delta\nu_r} \int_{\Delta\nu_r} T_\nu(z_2, z) d\nu$$

The total upward flux over $\Delta\nu_r$ is similarly defined

$$F_r^\uparrow(z_2) = \int_{\Delta\nu_r} F_\nu^\uparrow(z_2) d\nu$$

Averaging (1) over the r (th) interval gives

$$\frac{1}{\Pi} F_r^\uparrow(z_2) = I_{\Delta\nu_r}(z_1) \bar{T}_r(z_2, z_1) + \int_{z_1}^{z_2} J_{\Delta\nu_r}(z) \frac{d\bar{T}_r(z_2, z)}{dz} dz$$

which must be summed over all intervals to complete the frequency integration.

The frequency averaged transmission functions are based on a combination of laboratory data and band models. The transmission depends on pressure, temperature, and the mixing ratio of the absorber being considered. In the troposphere and lower stratosphere, pressure broadening of absorption lines is more important than temperature (Doppler) broadening. In the Dopplick model the temperature dependence is incorporated in the effective mass mixing ratio of the absorber, and the pressure dependence is corrected for using the Curtis-Godson approximation.

If the radiation travels an inhomogeneous path which contains integrated mass u ,

$$u = \int_z^{z_2} \rho \, dz'$$

then $\bar{T}_r(z_2, z)$, which is a function of pressure (and also of temperature) will not be constant along the path. In the Curtis-Godson approximation, the mean pressure along the path is defined

$$\bar{p} = \frac{\int p \, du}{\Delta u}$$

where Δu is the path length defined by the integration limits, and the path is treated as though it were homogeneous, with \bar{p} replacing p in the transmission function. The errors introduced by this approximation have been estimated by Walshaw and Rodgers (1963). They concluded that the Curtis-Godson approximation is good for H₂O and CO₂ absorption but poor for O₃. A four parameter transmission model, given by Rodgers (1968), is therefore used for the 9.6 μ O₃ interval.

The actual frequency averaged transmission functions used in the model are given in Hoffman (1981). Lorentz line shape is assumed for transmission functions derived from band models. For intervals where more than one absorber is considered, it is assumed that the transmissions multiply.

Clouds, like the earth's surface, are assumed to be black bodies to thermal radiation. Houghton (1985) suggests that, while this is a good assumption for low clouds, many mid-level clouds (alto- and stratocumulus) do not radiate as black bodies. Platt (1976) found that the cloud emissivity was related to the liquid water content of a path through the cloud, which is not necessarily correlated to cloud

depth (clouds can be geometrically thick yet tenuous, or thin yet dense).

Emissivities of cirrus clouds also depend on the water content (ice content) in a column through the cloud. The emissivity of cirrus is generally below unity. This has been somewhat compensated for in previous studies using the Dopplick model by reducing the sky coverage by 50%; this is equivalent to an emissivity of .50, which is a good approximation for fairly dense cirrus but probably still too high for wispy or tenuous cloud (Houghton, 1985) and too low for thundercloud outflow (Ackerman et al., 1988).

Cloud layers which only partially cover the sky are handled by calculating fluxes for several plane stratified cloud structures and averaging them together, using the fractional coverage as a weight. Edge effects are neglected. An example, reproduced from Hoffman (1981), is shown in Figure 3.1. Because of this averaging over many cloud structures, it would be expected that the model would correspond poorly with fluxes obtained from an instrument with a narrow field of view, or from an instrument that was not very far above a cloud.

3.3 Solar region

It is assumed that radiation is not scattered or emitted by the atmosphere in this part of the spectrum. The flux at a given level depends on the original intensity at the top of the atmosphere, and on the path that the radiation followed. Calculation of the net flux at a selected level in the atmosphere requires summation over all paths, integration over frequency, and averaging over one day.

Clouds are considered to absorb, reflect, and transmit varying fractions of the incident radiation in this wavelength region, depending on the height (i.e., type) of the cloud. Because clouds are partial reflectors, different fractions of the incoming radiation will follow different paths, some quite complicated; Figure 3.2, reproduced from Hoffman (1981), shows some possible paths. The model traces the incoming radiation over all possible paths, tracing each ray until it is completely absorbed or escapes to space. The probability that a ray will interact with a cloud is equal to the fractional sky coverage of that cloud layer. Note that this implies that clouds are randomly distributed in the horizontal, since each interaction has no dependence on previous ones. This is not the same as in the thermal infrared, where the overlap of cloud layers may be prescribed. The cloud optical parameters are input by the user and are discussed further in section 4. Clearly, any variation from the actual cloud parameters will affect the net fluxes obtained.

The surface is also a partial reflector; the land reflectivity is input by the user, and the reflectivity of the ocean is taken to be 0.061 for diffuse radiation (after interaction with a cloud or the surface), and a function of solar zenith angle for direct radiation (values taken from Payne, 1972).

The vertical flux of radiation at a frequency ν , $F_\nu(\underline{u}, z)$, reaching a level z along a particular path, is given by

$$F_\nu(\underline{u}, z) = (-1)^J F_\nu(\underline{0}, \infty) T_\nu(\underline{u})$$

where \underline{u} is the vector of absorber amounts along the path, T_ν is the transmission function, $F_\nu(\underline{0}, \infty)$ is that part of the flux at the top of

the atmosphere which follows the path, and γ is the number of reflections in the path. If this is integrated over a frequency interval $\Delta\nu_r$ small enough that $F_\nu(\underline{Q}, \infty)$ may be considered constant, then

$$F_r(\underline{u}, z) = (-1)^\gamma F_r(\underline{Q}, \infty) \bar{T}_r(\underline{u})$$

where

$$F_r(\underline{u}, z) = \int_{\Delta\nu_r} F_\nu(\underline{u}, z) d\nu$$

and

$$\bar{T}_r(\underline{u}) = \frac{1}{\Delta\nu_r} \int_{\Delta\nu_r} T_\nu(\underline{u}) d\nu$$

Calculations are carried out separately for the solar visible and near infrared regions, as discussed above. In the visible region, no pressure or temperature dependence is assumed; absorption is calculated from Kennedy's (1964) table. The near infrared absorption is calculated from values given by Rodgers (1967), and corrects for pressure but not for temperature. Surface albedo is considered to be completely independent of ν ; the cloud optical properties are assumed to be independent of ν within each region.

Diurnal averaging is performed because the sun's zenith angle varies over the course of a day, lengthening the path traveled by the radiation. This is only important during the first part of the path, when the radiation is direct; after interaction with a cloud or the ground the radiation is considered diffuse, and Elsasser's diffusivity constant is employed as in the thermal portion of the spectrum. Diurnal averaging is useful for computations of time- and space-averaged radiation balances, as made by Rodgers (1967) and

Dopplick (1970). For the present comparison, the diurnal averaging code was bypassed, and the solar fluxes were computed using the actual sun position at the time of the measurements.

3.4 Modifications to the model for this comparison

In the Dopplick model, the 6.3μ water vapor band is the dividing line between thermal infrared and solar near infrared, and the 0.76μ O₂ band divides the solar near infrared and solar visible regions. The short wavelength limit of the infrared radiometer used in this comparison is 2.9μ , which is therefore within the solar near infrared region. Four absorption bands contribute to the total flux between 2.9μ and 6.3μ : the 3.3μ H₂O band and the 4.3μ , 4.8μ , and 5.2μ CO₂ bands. The bandwidths are given in Table 3.1. For purposes of this comparison, contributions from these bands were summed separately during the near infrared calculations and added to the thermal infrared flux at each level. This contribution accounts for about 5% of the resulting flux.

Several modifications were necessary for the solar calculations. The range of the solar radiometer encompasses the entire near infrared region except for the four bands discussed above. On the short wavelength end, the radiometer range extends into the model's solar visible region, to 0.6μ . Since the model treats this region as one wide O₃ band, it was not possible to simply add in the appropriate bands. Instead, using Kondratyev's (1969) table of the distribution of energy in the solar spectrum, it was determined that for direct radiation, 37% of the energy in wavelengths shorter than 0.76μ is in the region from 0.6μ to 0.76μ . The calculated flux in the visible range

was therefore multiplied by 0.37 before being added to the solar near infrared flux (with the four bands discussed above subtracted) to yield the total solar flux in the radiometer range. The contribution from the visible range is generally about a third of the total; an error is introduced because the 37% is for energy passing through the entire atmosphere, but this is small compared to the total uncertainty in the solar radiometer since the level of interest is well below the O₃ maximum.

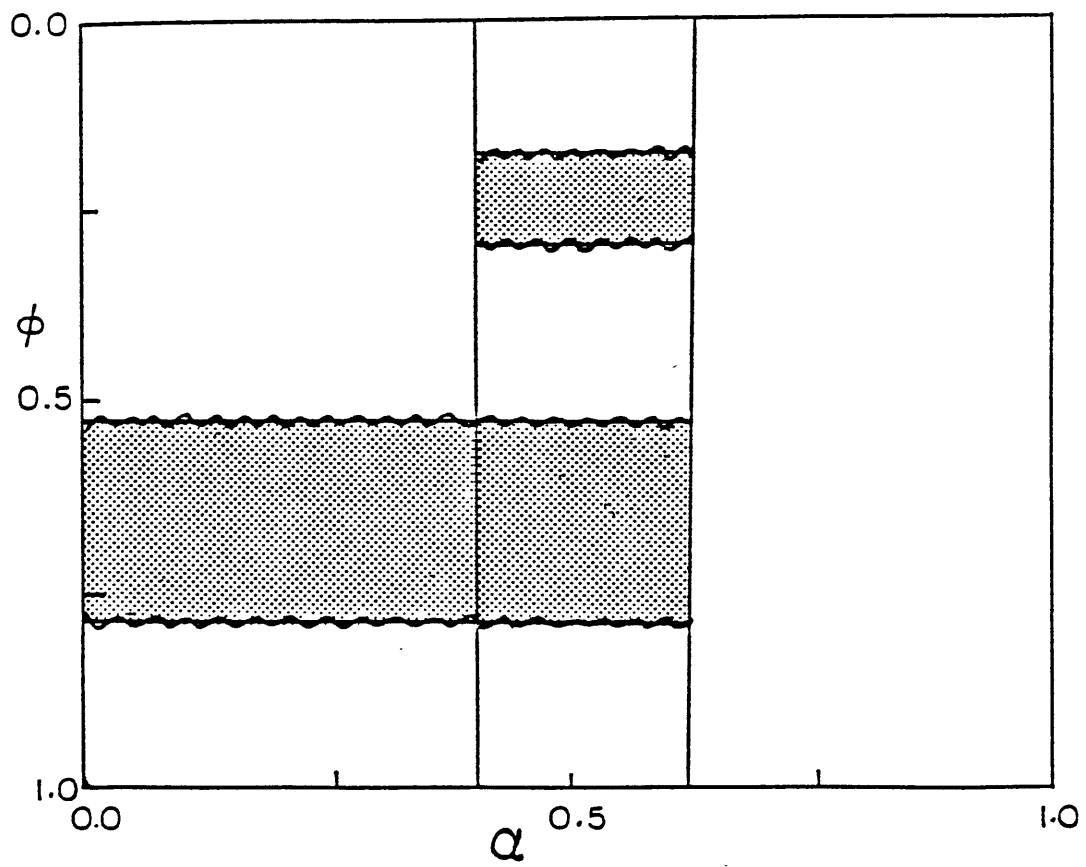
Because data from the upward-looking solar radiometer was not released, the program was modified to sum the upwelling and downwelling solar radiation separately. The comparisons between measured and computed solar flux in this paper are of upwelling flux, not net flux.

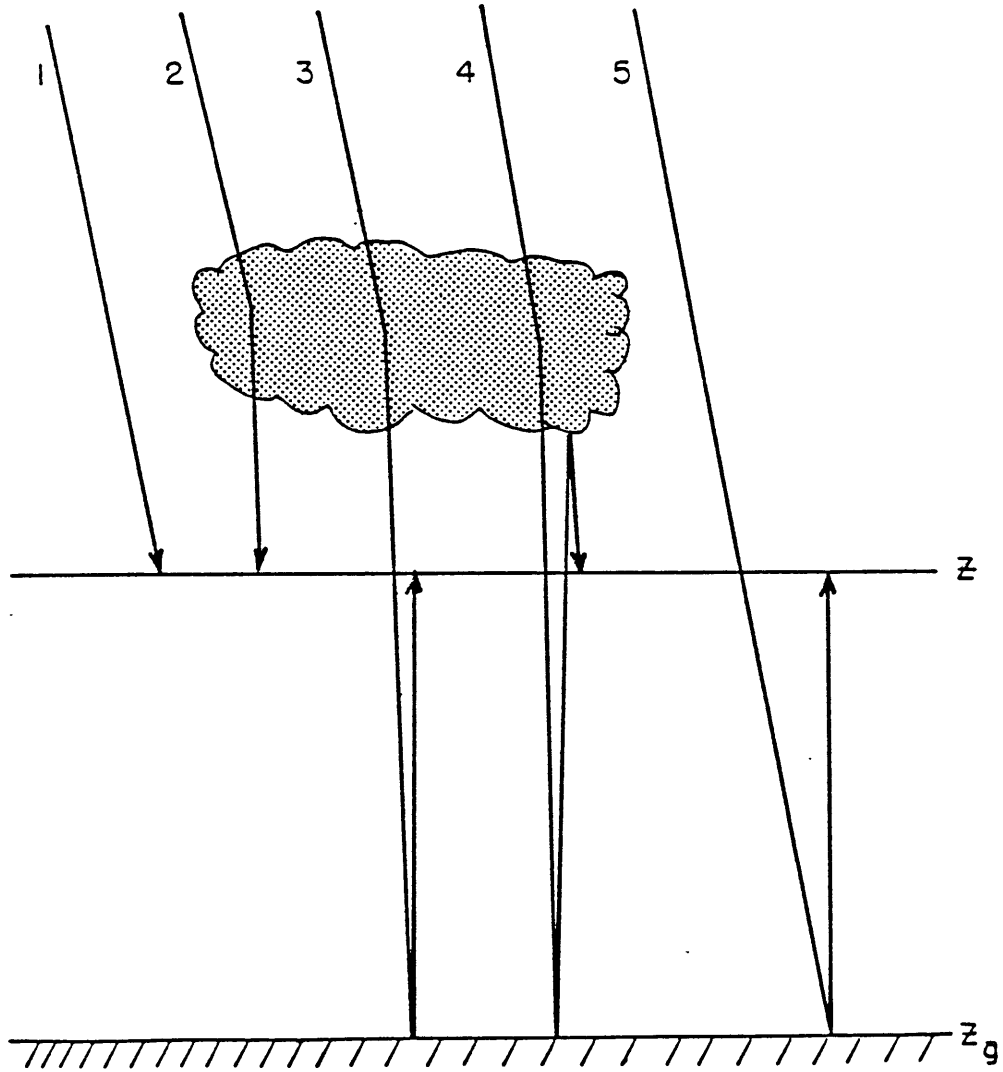
Finally, as mentioned above, diurnal averaging was not performed since the local time, and therefore solar zenith angle, was known.

Figure captions

- 3.1 A possible cloud structure for thermal radiation, from Hoffman (1981). In this example, there are three plane stratified cloud structures -- low cloud, low and high cloud, and no cloud. The effects of these are averaged together, using the fractional coverage as a weight.

- 3.2 Some possible paths for solar radiation, from Hoffmann (1981). The chance of a ray interacting with the cloud is equal to the fractional coverage of the cloud. After interacting with a cloud or the surface, the radiation is diffuse.





4. Data

4.1 Introduction

The data used were collected during the Stratosphere-Troposphere Exchange Project (STEP) deployment in January and February, 1987, in the region around Darwin, Australia. The limitation to a tropical atmosphere may affect the applicability of these results to more general cases.

The STEP experimenters conducted a series of ER-2 high altitude aircraft flights in order to examine potential dehydration mechanisms for tropospheric air entering the lower stratosphere. Because one proposed mechanism postulates stratosphere-troposphere interaction through high convective cloud turrets, most flights were in and around such clouds. Included among the instruments were three different radiometers: an infrared narrow field of view radiometer, measuring upwelling radiation intensity at 10μ and 6μ ; a broadband, hemispheric field of view infrared radiometer, measuring upward and downward fluxes; and a broadband, hemispheric field of view solar radiometer, measuring upward and downward fluxes. The latter two instruments were described in Section 2. Also on the aircraft were various meteorological instruments measuring air temperature, pressure, ozone concentration and water vapor concentration.

Broadband infrared and solar fluxes were made available for STEP flights 9, 10, and 12. Solar fluxes only were provided for STEP flight 7. All of these flights were over water; Figures 4.1-4.4 show the flight tracks superimposed on surface maps. Satellite photographs (near infrared) were obtained for each flight, and are

shown, with partial flight tracks, in Figures 4.5-4.8. The flight numbers, flight dates, and the locations and WMO numbers of the upper-air stations nearest to the flight track, are given in Table 4.1. Soundings at these stations at the time nearest to the time of the flight are plotted in Figures 4.9-4.12.

Concurrently with STEP, the Australian Bureau of Meteorology conducted Phase II of its Australian Monsoon Experiment (AMEX). As the objective of AMEX was to obtain a comprehensive aerological data set over northern Australia, the network of upper-air stations flew radiosondes four times daily, and several stations were equipped with Vaisala sondes provided by NASA. The Vaisala sondes can provide water vapor measurements at lower humidities than ordinary radiosondes, and are also capable of generating high resolution vertical profiles (Hummel et al, 1985). In addition, a Chinese research ship positioned in the Gulf of Carpentaria also flew Vaisala sondes.

4.2 Temperature and water vapor profiles

Because the ER-2 aircraft is designed for flight in a rarefied atmosphere, and because the primary purpose of the STEP flights was to collect data relevant to studies of stratosphere- troposphere interaction, the levels at which radiation measurements were made are in the vicinity of the tropopause, generally between 150 and 50 mb. Meteorological measurements made from the aircraft are obviously preferable to radiosonde data, since they are taken at the same place and time as the radiation measurements, but they do not provide a full profile to the ground. For this reason, the profiles used

in section 6 as input to the model are a combination of data from the meteorological instruments aboard the ER-2, for the tropopause region, and radiosonde data from the nearest station below the flight level. For one flight (flight 9), the ER-2 meteorological data was not available, and radiosonde data is used for the entire profile. Upper-atmosphere data above the levels of both the radiosonde and the ER-2 (generally 40 mb to the top of the atmosphere) was taken from the climatology used by Doplick (1970).

Although the aircraft flew segments of each flight at different altitudes, these levels were generally not directly above each other. In addition, the time between the first and last segment of the stepwise profile ranged from a minimum of two hours in flight 10 to a maximum of slightly more than four hours in flight 9. Use of this data requires the assumption of spatial and temporal homogeneity of the vertical temperature and humidity profiles. Analyses over the northern Australian region suggest that this is not a bad assumption over the Arafura and Timor Seas, the Gulf of Carpentaria, and the northern coast.

4.3 Ozone profiles

The Australian Bureau of Meteorology flew ozonesondes from Darwin on most STEP flight days. Values for the ozone concentration below flight level were taken from the ozonesonde flown closest to the flight date; data from the ozone measuring instrument aboard the ER-2 was used at the aircraft level.

Table 4.1. Flight dates and the station used for each flight.

Flight	Date (GMT)	Station	WMO #	S latitude	E longitude
7	23-24 Jan 1987	Chinese ship	01139	11°30'	139°00'
9	30-31 Jan 1987	Darwin	94120	12°26'	130°52'
10	2-3 Feb 1987	Gove	94150	12°16'	137°00'
12	7-8 Feb 1987	Gove	94150		

Table 4.2. Optical properties of clouds in the solar region (from Dopplick, 1970).

Cloud	Transmissivity		Reflectivity	
	Visible	NIR	Visible	NIR
High	0.79	0.77	0.21	0.19
Mid	0.46	0.34	0.54	0.46
Low	0.34	0.20	0.66	0.50

4.4 Cloud profiles

The clouds presented the greatest challenge, and two approaches were used. For the first set of comparisons, described in section 6.1, it was assumed that the aircraft was sufficiently high above the clouds that the field of view encompassed a random ensemble of the clouds present. The heights of the cloud bases and the sky coverage for each type of cloud were taken from surface synoptic reports. The geometric thickness of each cloud layer was estimated from climatology and from the observed humidity profile.

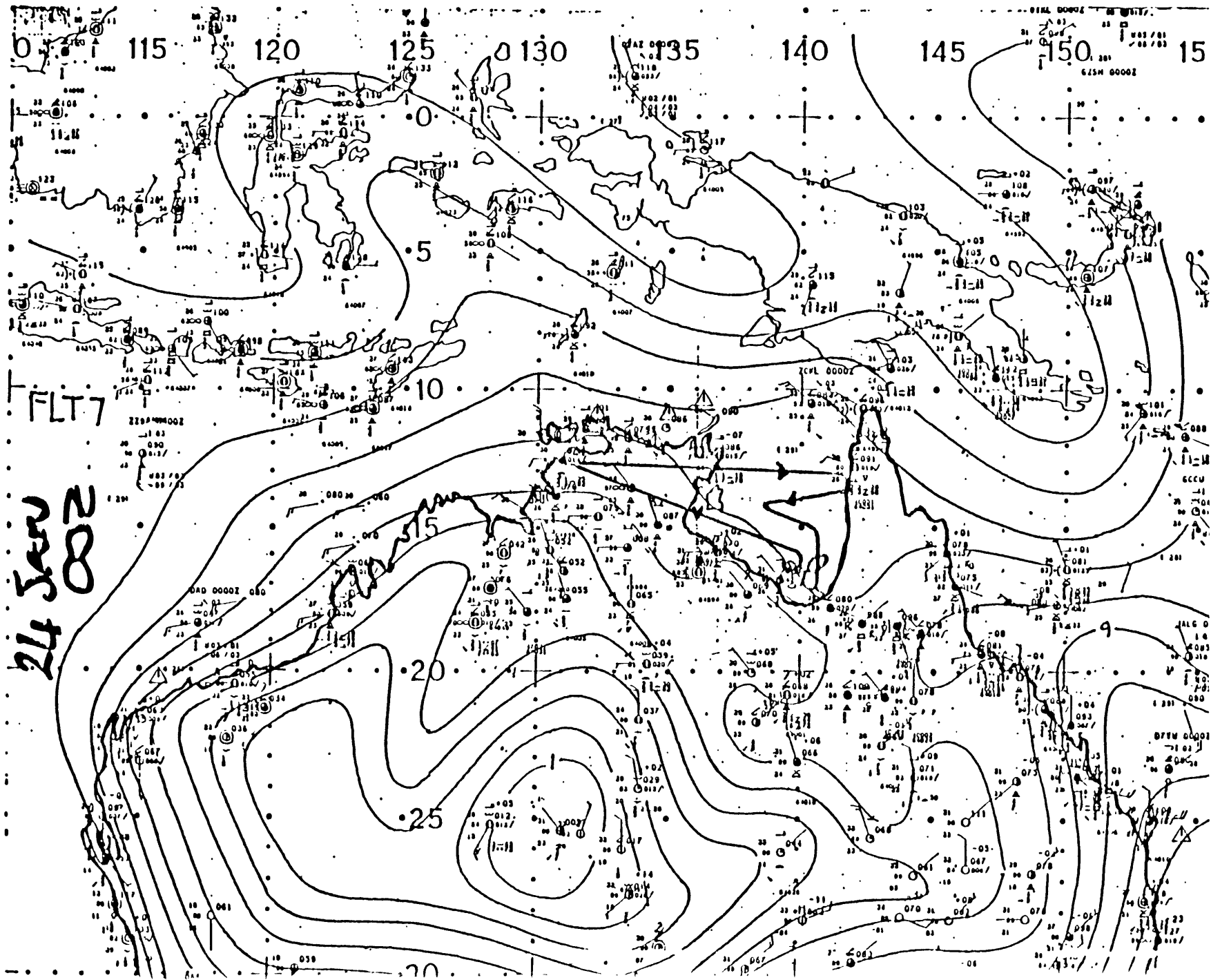
The second approach was adopted when it became apparent that the instruments' field of view was limited to whatever mass of cloud was directly below it; therefore, each layer of cloud was assumed to cover 100% of the sky. Since this method was an attempt to model the clouds local to the aircraft (rather than construction of a spatial average), and the aircraft was not directly over the surface stations during most of the flight, the surface observations were not used to determine the heights of the cloud layers. Instead, cloud profiles were constructed based on the stations' temperature and humidity profiles, on the satellite photographs, and on knowledge of the synoptic situation. These profiles were used in the comparisons discussed in Section 6.2.

The cloud optical properties in the solar spectral region were taken from Dopplick (1970); these values, which have been used in most studies using the Dopplick model, are given in Table 4.2. Clouds were considered to be black bodies with respect to thermal infrared radiation, except for cirrus clouds which were assumed to have emissivities of 0.75. This value was chosen because tropical

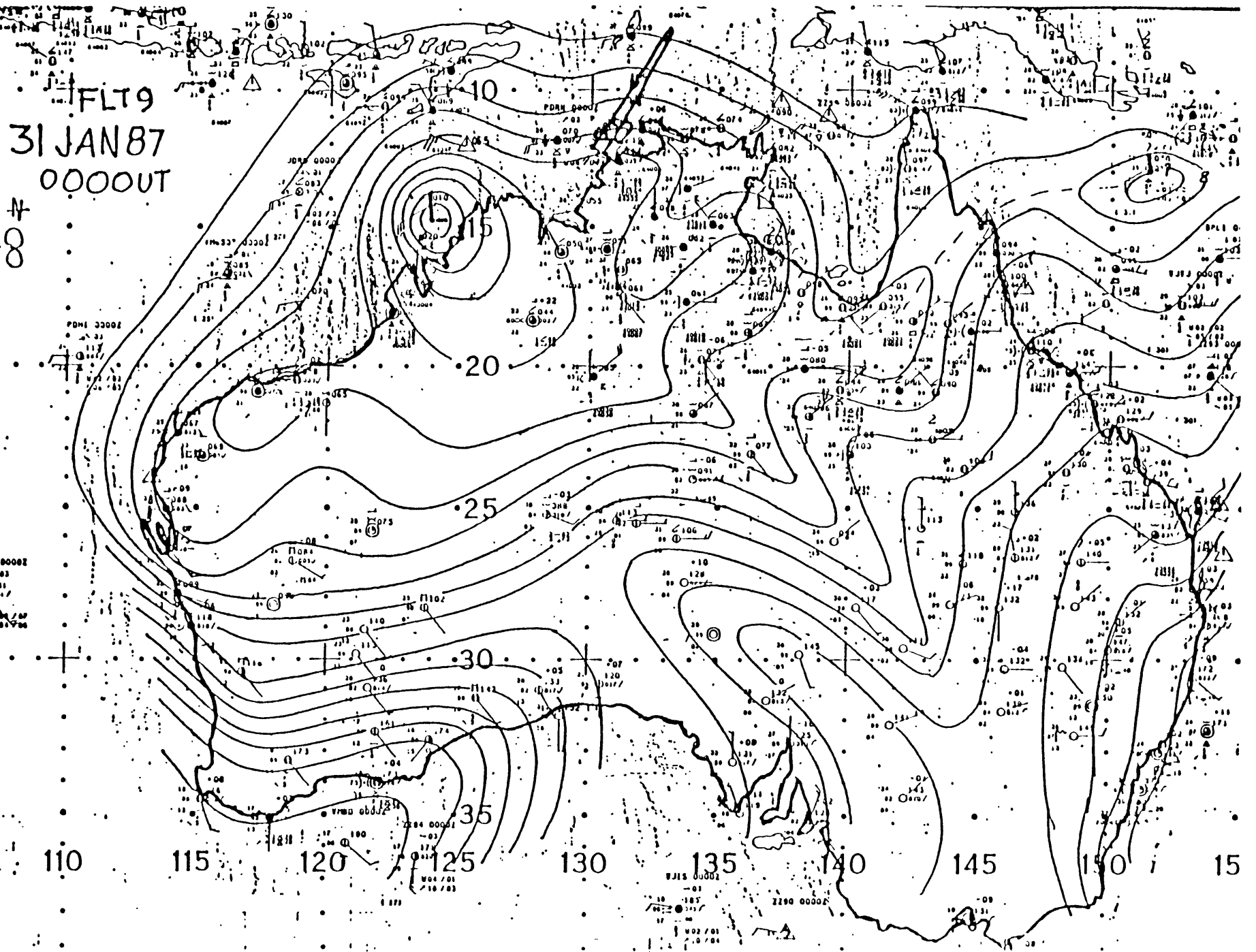
cirrus decks are typically optically thick (e.g., Ackerman et al. 1988); most other studies using this model have assigned an emissivity of 0.5 to cirrus.

Figure captions

- 4.1 Surface analysis over Australia, with the flight track superimposed, for 24 January 1987 (flight 7).
- 4.2 Same as 4.1, for 31 January 1987 (flight 9).
- 4.3 Same as 4.1, for 3 February 1987 (flight 10).
- 4.4 Same as 4.1, for 8 February 1987 (flight 12).
- 4.5 Near infrared satellite photograph of the Gulf of Carpentaria region, for 24 January 1987 (flight 7)
- 4.6 Same as 4.5, for 31 January 1987 (flight 9).
- 4.7 Same as 4.5, for 3 February 1987 (flight 10).
- 4.8 Same as 4.5, for 8 February 1987 (flight 12).
- 4.9 Sounding at the Chinese ship used in conjunction with flight 7.
- 4.10 Sounding at Darwin used in conjunction with flight 9. Cloud layers are between 975-769 mb (12.5% sky coverage), 935-769 mb (25%), and 640-433 mb (87.5%).
- 4.11 Sounding at Gove used in conjunction with flight 10. Cloud layers are between 989-879 mb (10% sky coverage), 701-675 mb (70%), and 655-508 (100%).
- 4.12 Sounding at Gove used in conjunction with flight 12. Cloud layers are between 978-955 mb (60% sky coverage) and 641-597 mb (100%).

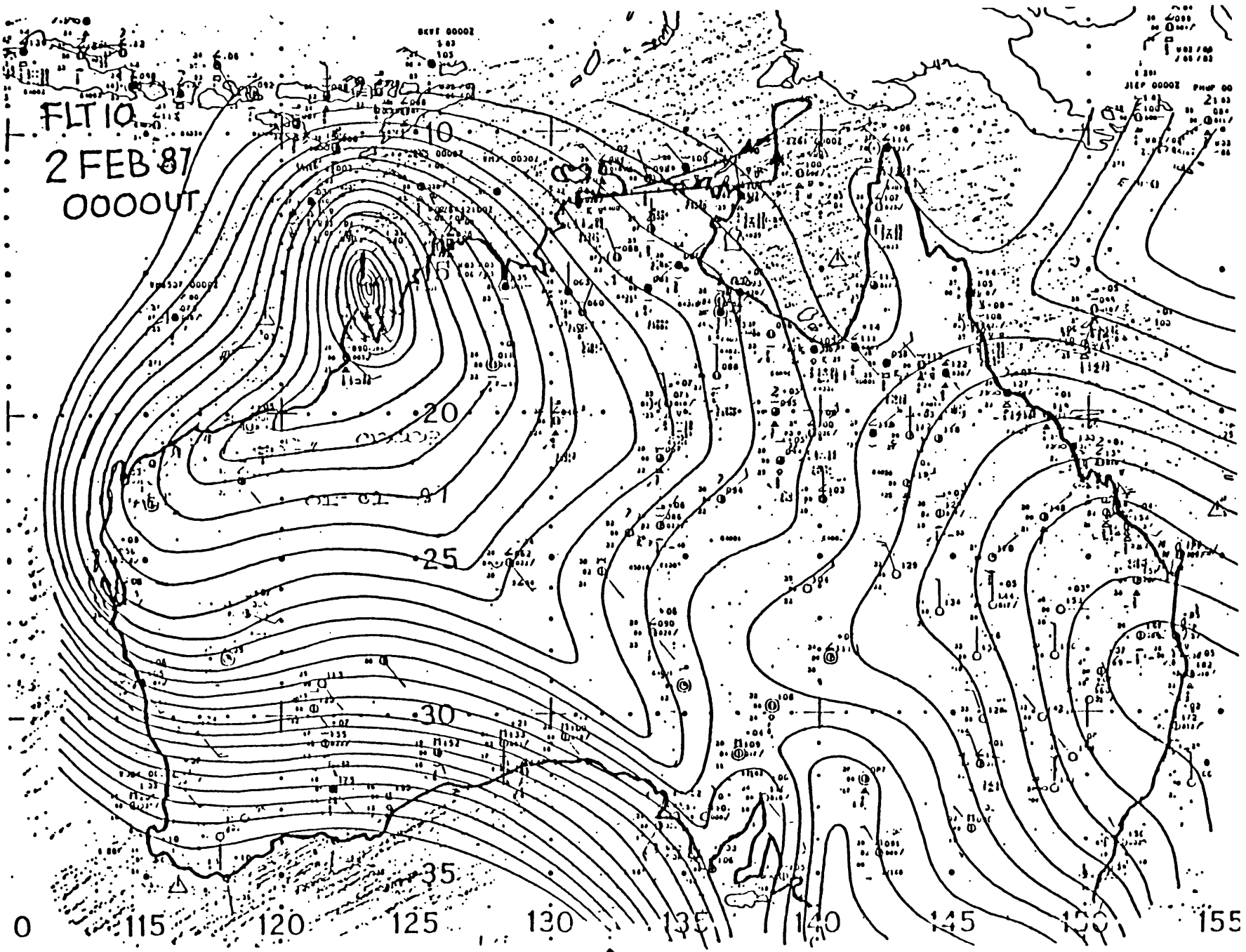


31 / Figure 4.1

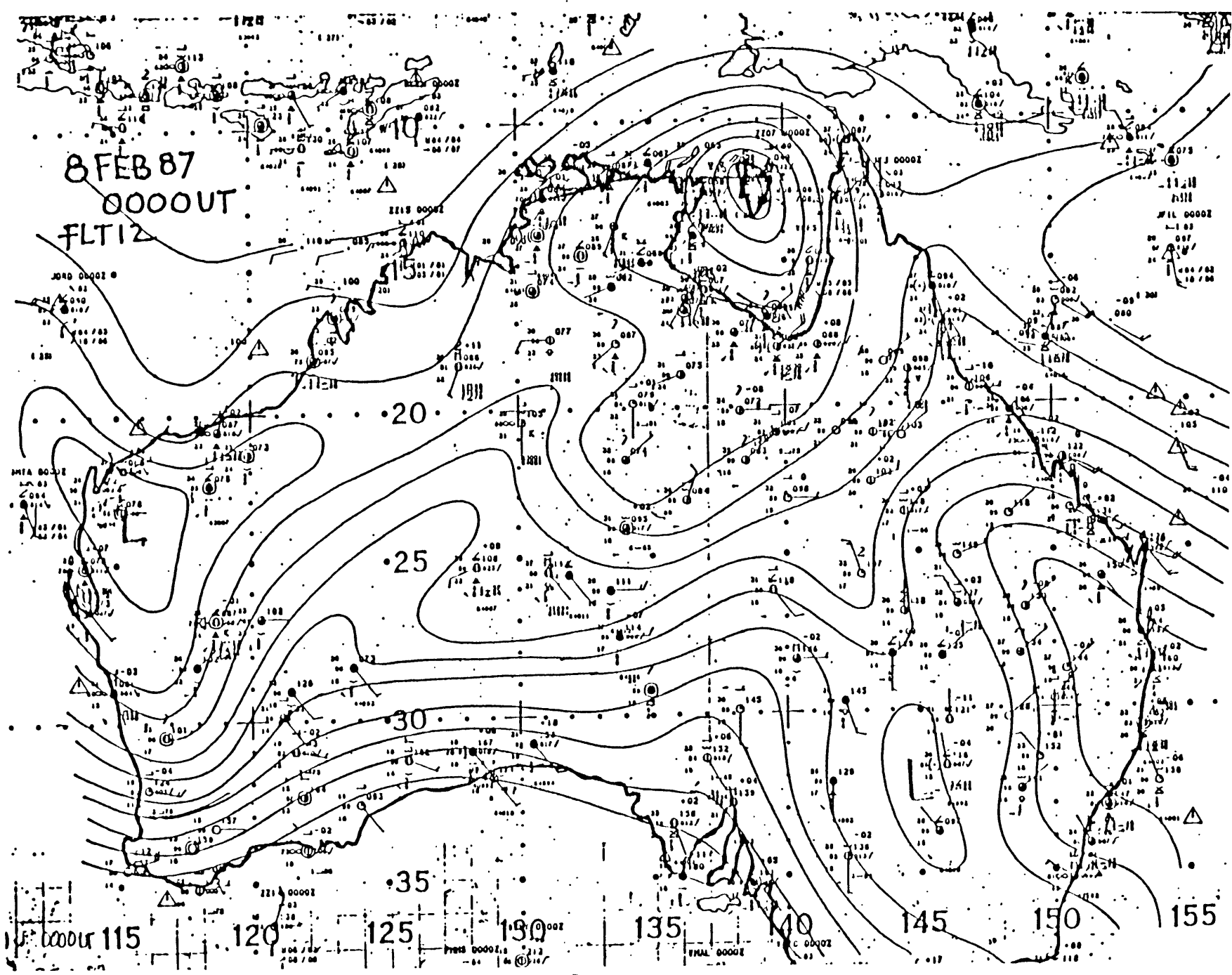


32 / Figure 4.2

FLT 10
2 FEB 87
0000UT

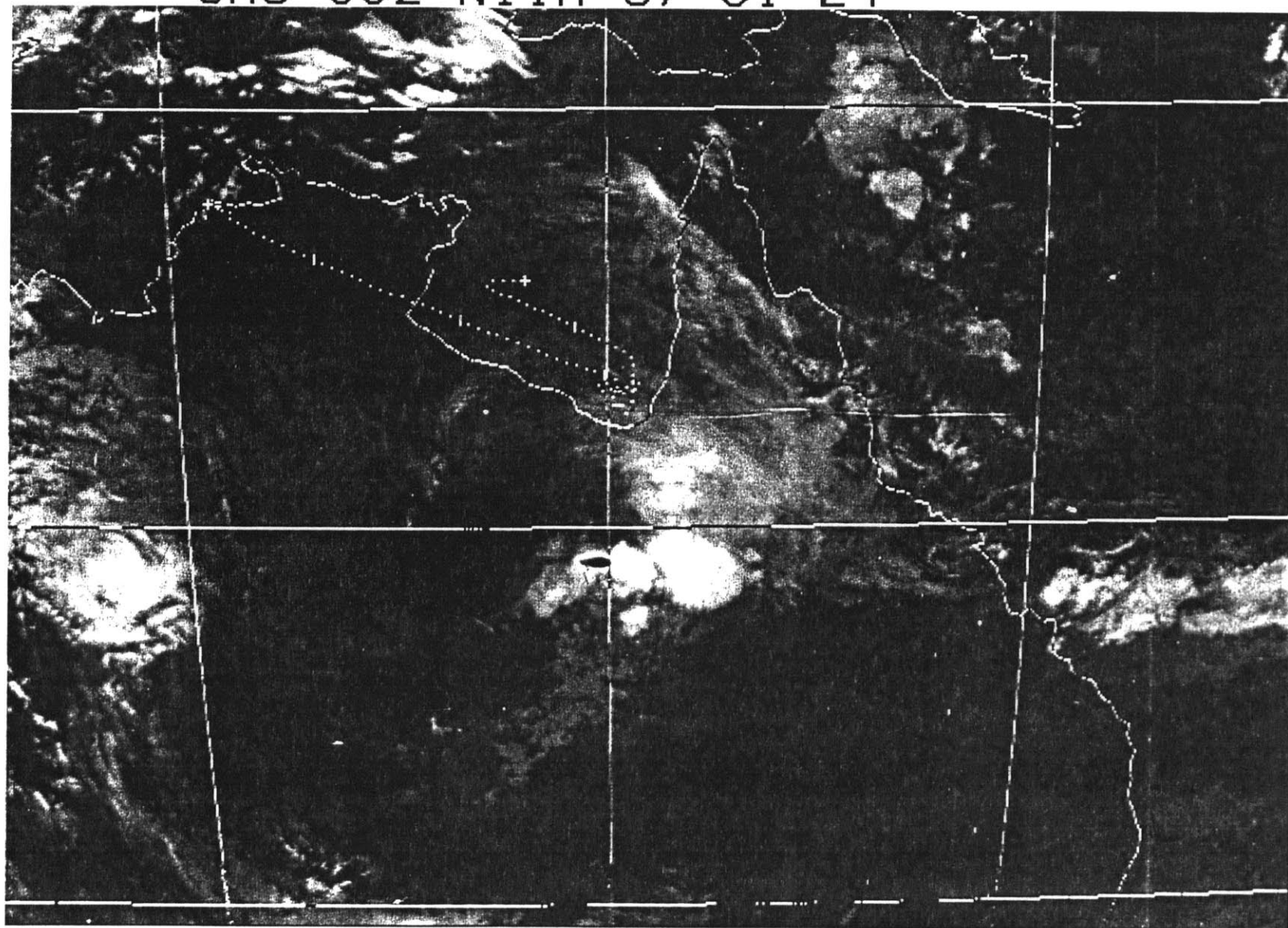


33 / Figure 4.3

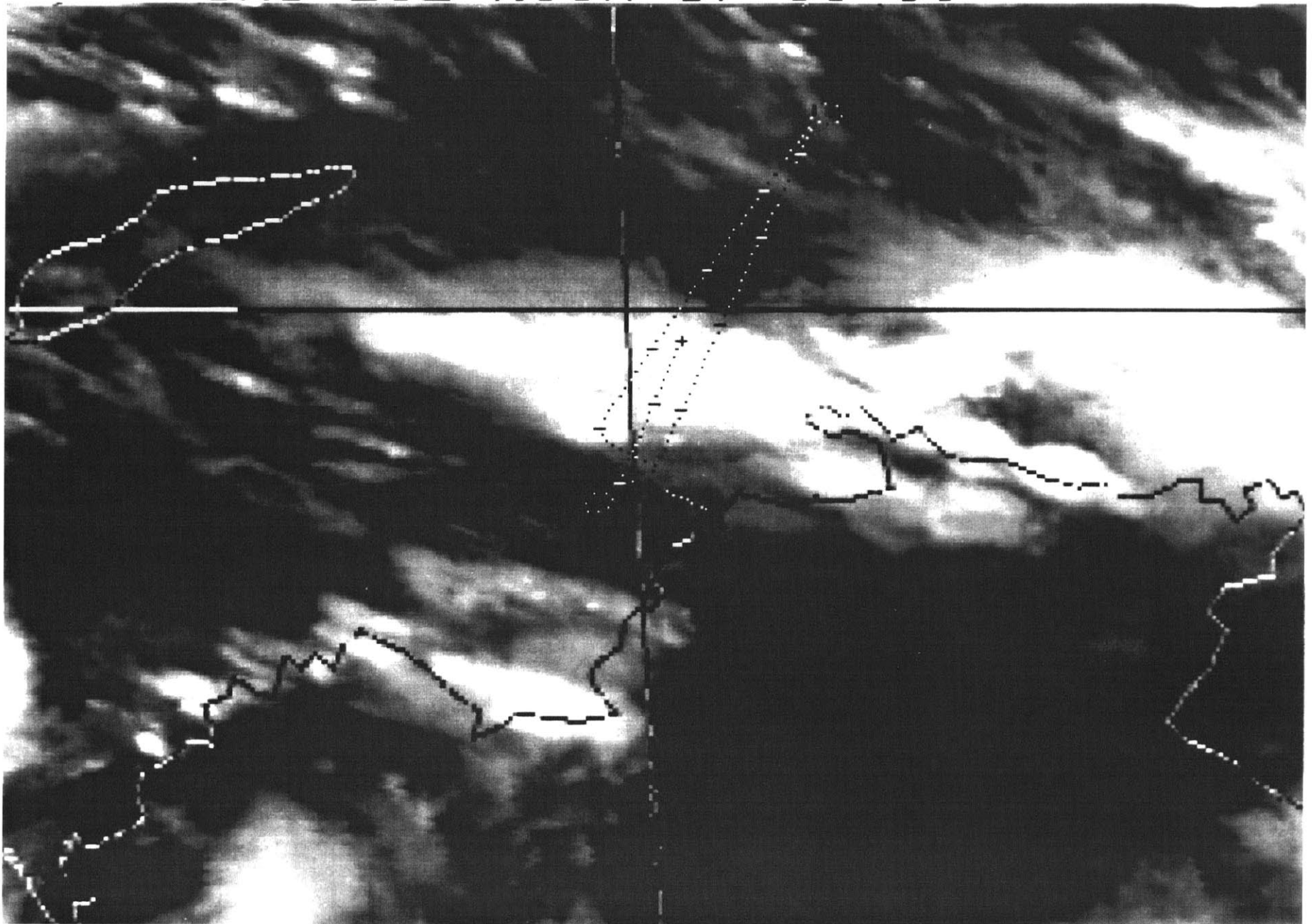


34 / Figure 4.4

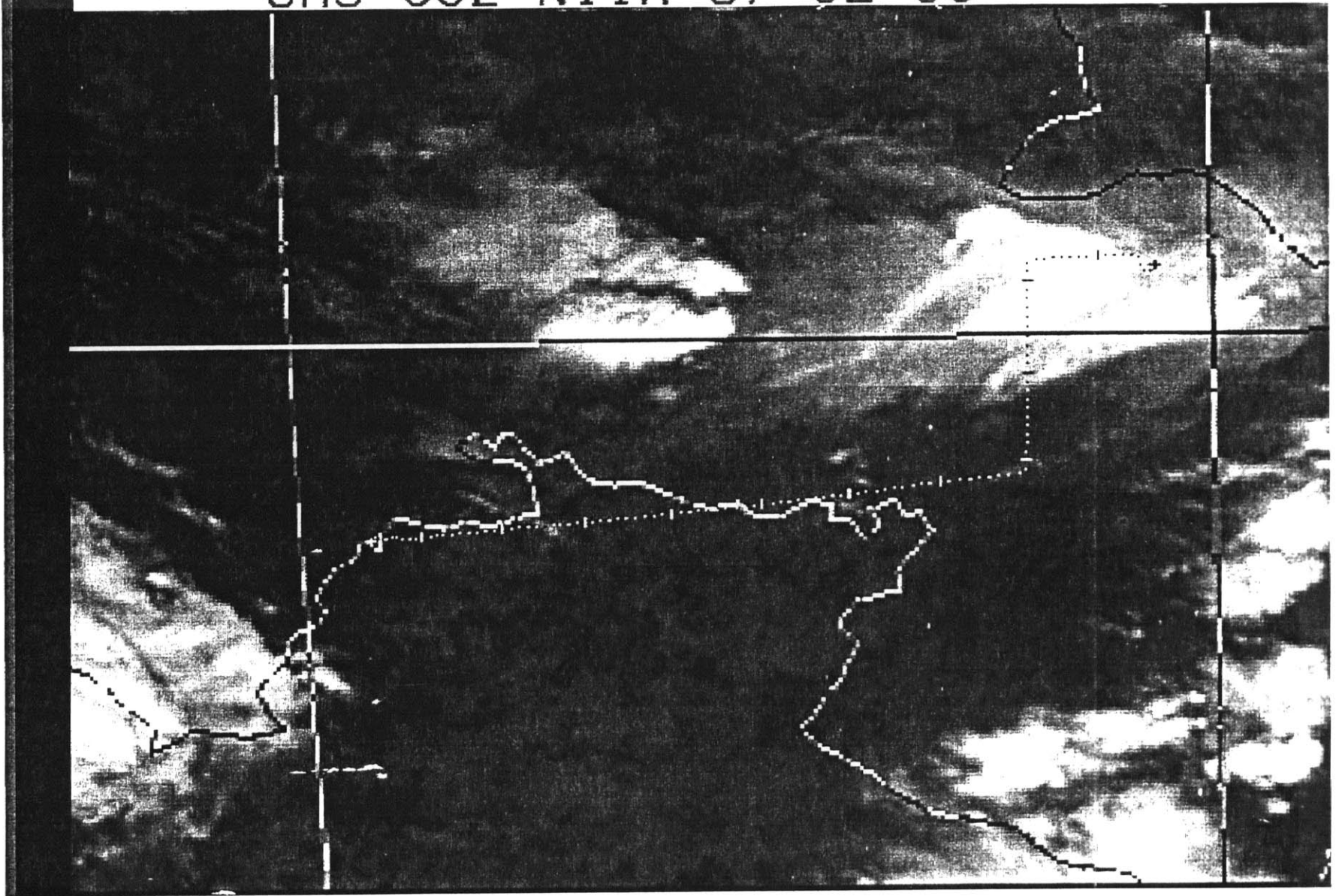
GMS 00Z NIIR 87 01 24



GMS 21Z N11R 8/ 01 31

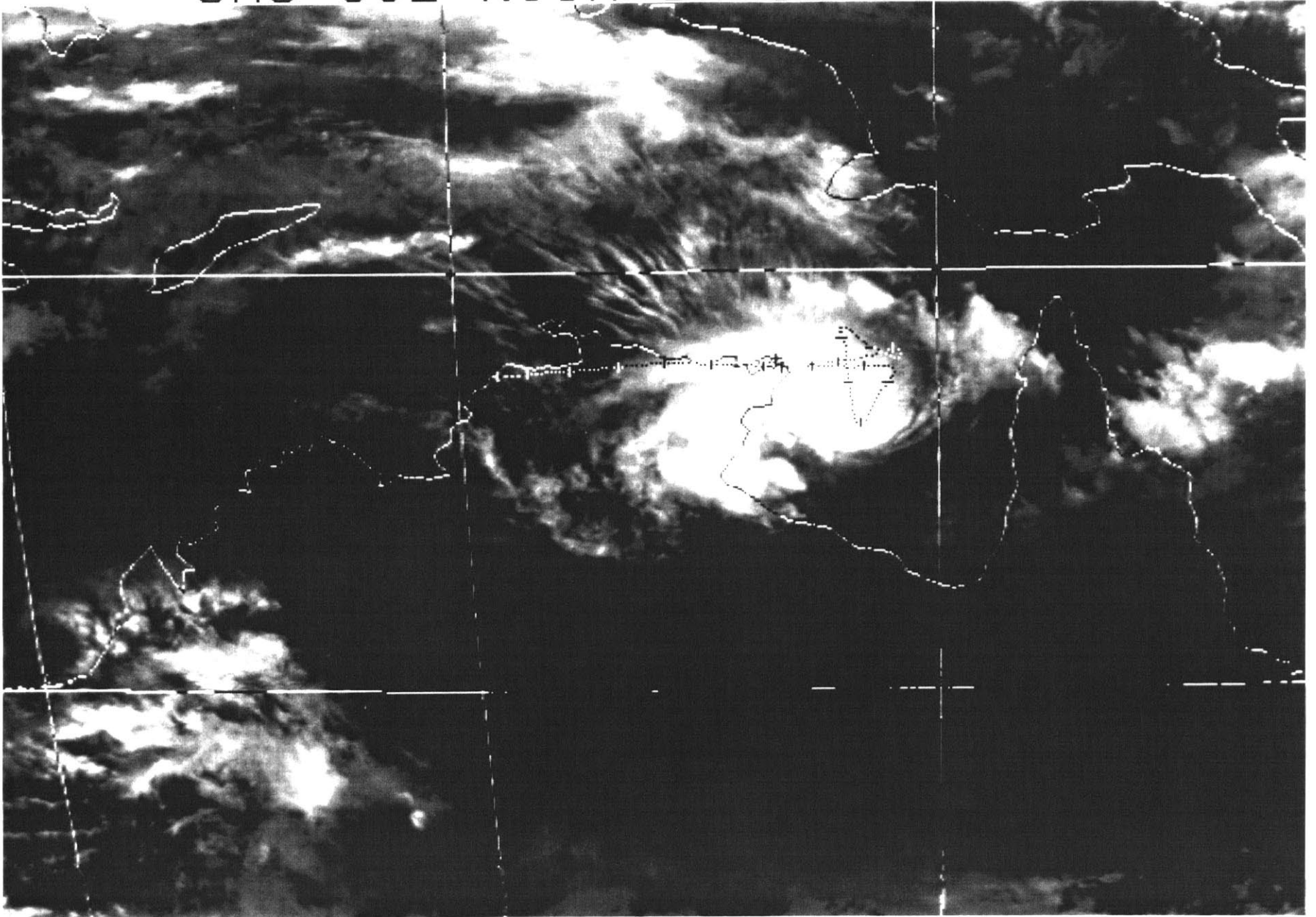


GMS 00Z N11R 87 02 05



37 / Figure 4.7

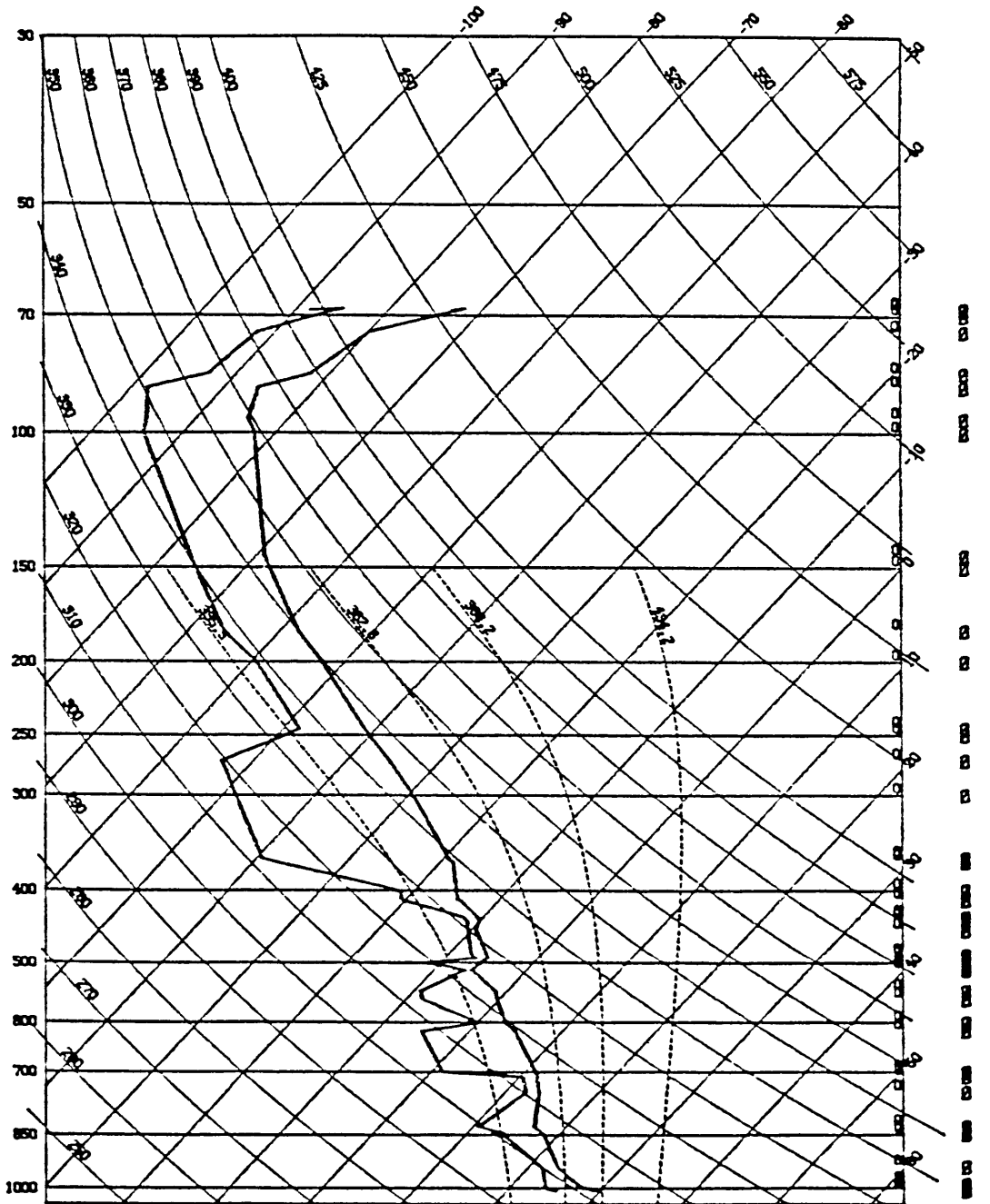
GMS 03Z N11R 87 02 08



38 / Figure 4.8

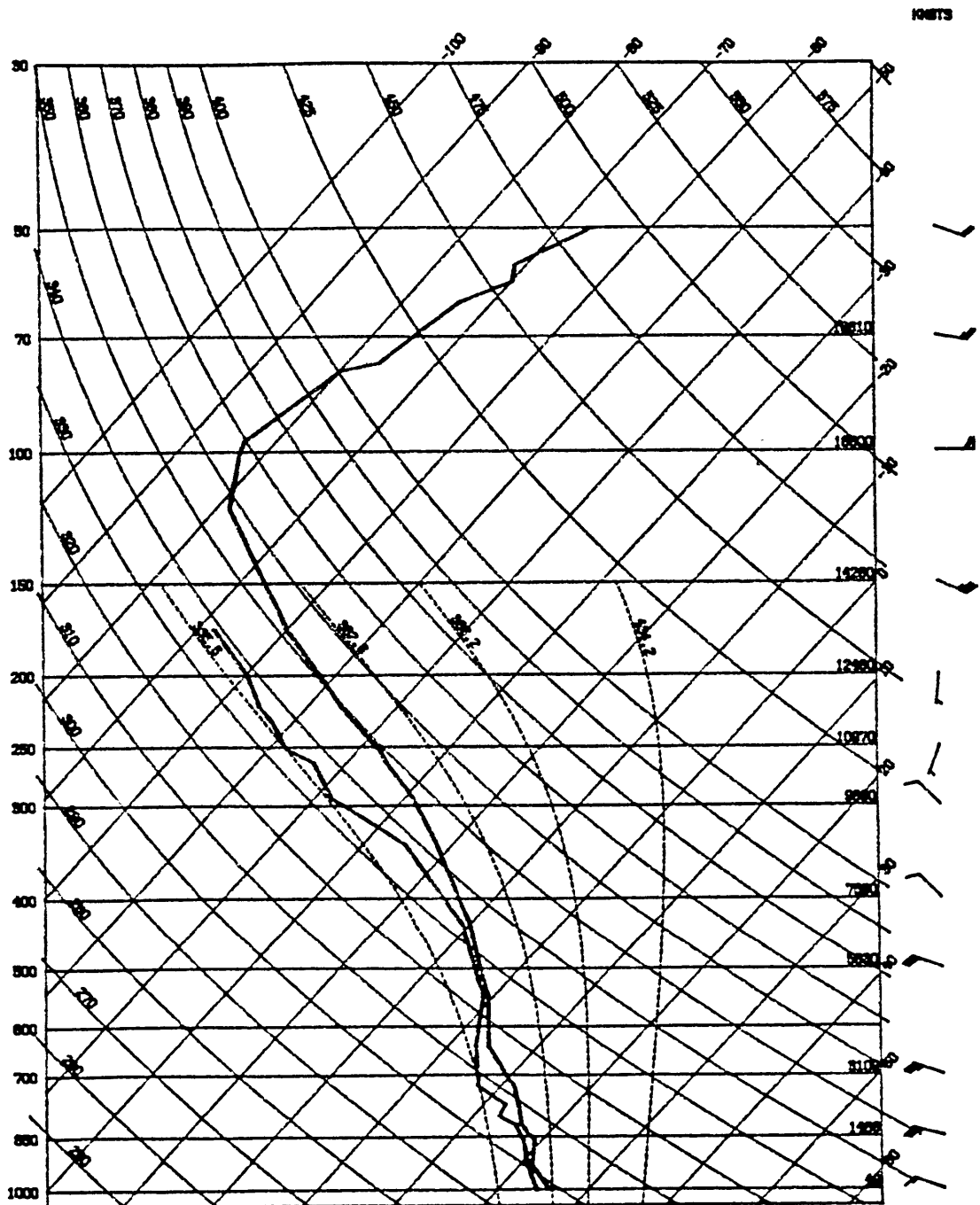
01139 CHINESE SHIP

23/01/87 23Z



94120 DARWIN

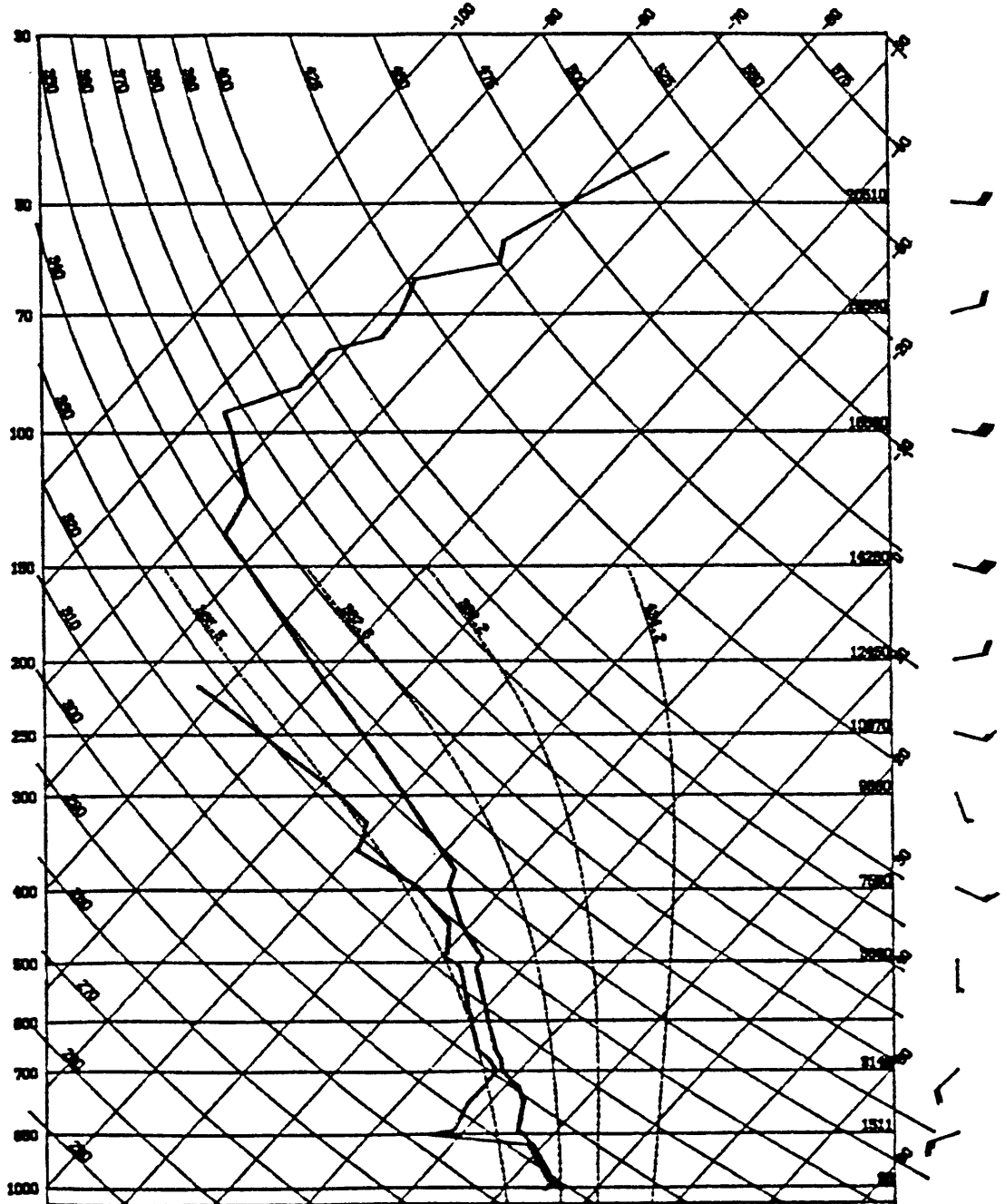
30/01/87 22Z



94150 GØVE

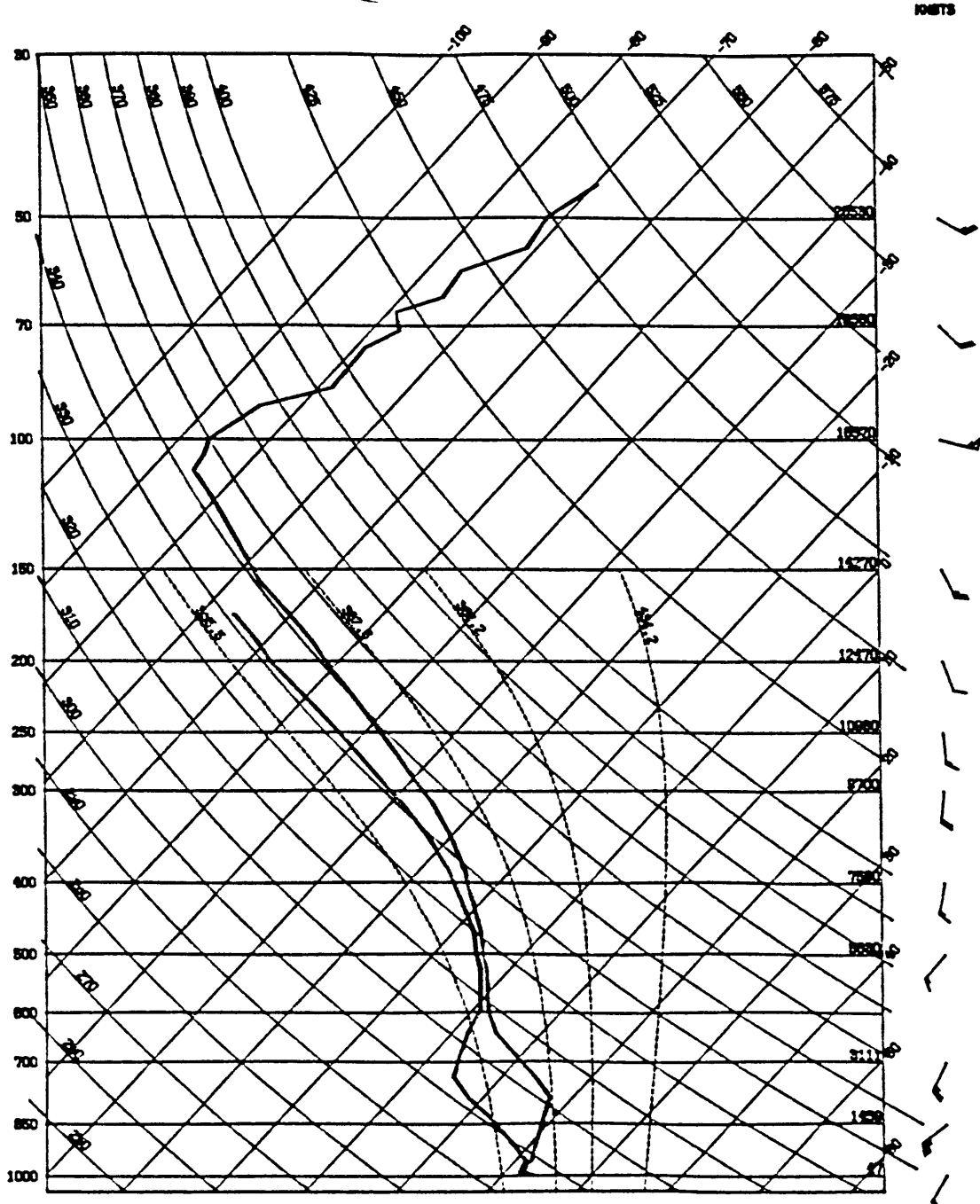
02/02/87 22Z

10473



94150 GØVE

07/02/87 22Z



5. Sensitivity of the model

Accurate model results depend on accurate model input. Discrepancies between model results and the observed fluxes could be due to errors in the atmospheric profile used as input to the model. This was tested in several ways.

First, the input temperature and humidity profiles were varied within expected accuracy, and the output compared with the results from an unmodified profile. The accuracies of the temperature and humidity sensors of the Vaisala sonde, taken from Hummel et al (1985), are $T = T_{\text{true}} \pm 0.5 \text{ K}$, and $U = U_{\text{true}} \pm 2\%$. It was assumed that the errors would be systematic rather than random.

The cloudless profile used for flight 7, shown in Figure 4.5, was modified in several ways: low/high humidity, low/high temperature, and combinations of "errors" in humidity and temperature. The errors in the net thermal fluxes did not exceed two percent at any level, and generally were a very small fraction of a percent. The two cases with the largest errors are shown in Figures 5.1 and 5.2. The errors in the upwelling solar fluxes were always much smaller than one percent.

Single bad data points in the profile, and non-systematic fluctuations caused by random errors, also do not change the fluxes significantly. The calculated layer heating rates are affected to a greater degree, since they depend on the flux divergence.

Because the information about clouds used in this study was limited to those clouds visible from the surface, it is quite possible (and in the tropical atmosphere considered, highly probable) that clouds may be present above the highest reported cloud level in

overcast skies. For example, the sounding from the ship in the Gulf of Carpentaria on February 2 suggests a cloud layer near 460 mb, even though the highest reported cloud was at 645 mb (Figure 5.3). Observations on other days, and at other stations in the northern coastal region of Australia, record large (in horizontal extent) altostratus layers at levels around 460 mb. The February 2 sounding was used to calculate the net thermal flux and the upwelling solar flux, with and without a layer of cloud from 493-430 mb. The upper and lower boundaries of the extra cloud were chosen somewhat arbitrarily, and it was assumed to cover the sky completely. The result is shown in Figures 5.4a and b.

The effect of an added higher cloud layer is to decrease the net upwelling thermal radiation at levels above the cloud. This is because of the T^4 dependence of the re-emitted radiation; the higher cloud is cooler and thus the outgoing radiation is decreased. It is clear that a layer of high cloud, such as cirrus, would decrease the upwelling thermal radiation to an even greater degree. The computed flux only changes by 5% with the added altostratus, but addition of a cirrus layer can decrease the net upwelling thermal flux by much more. Figure 5.5a shows the thermal flux profile calculated using a cirrus layer from 150-110 mb; the net upwelling radiation above the cloud is about half of its original value.

The computed upwelling solar radiation, in Figure 5.4b, is much more sensitive to an added altostratus layer than the computed thermal flux, increasing by 10% in this test case. The solar flux above the cloud level is less sensitive to cirrus, however, since the reflectivity used here for cirrus is low. Figure 5.5b shows the

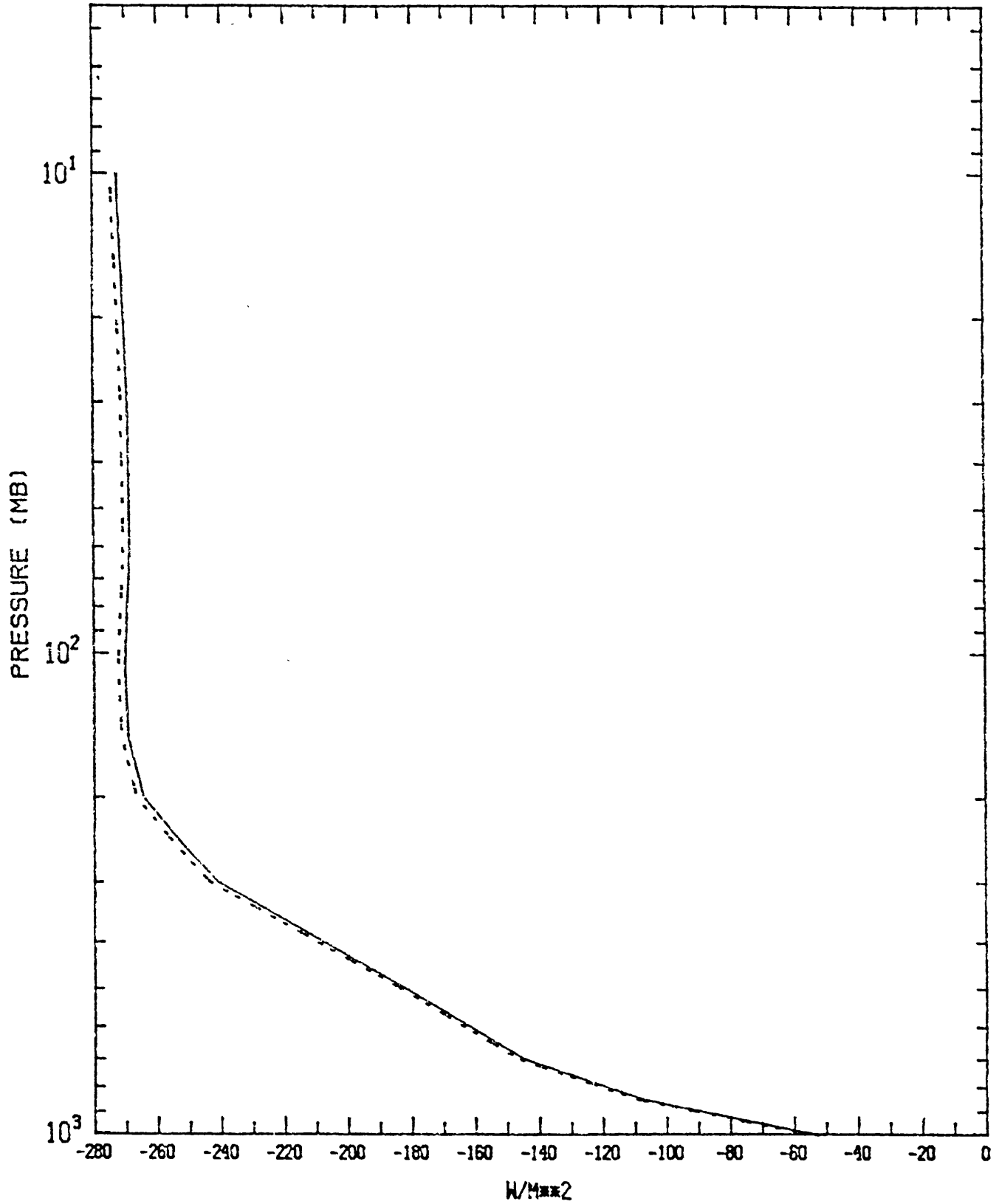
upwelling solar flux profile calculated with the added cirrus layer. It will be seen in section 6 that the thermal flux above the highest cloud is essentially determined by the height of that cloud only, while the solar flux is sensitive to all cloud layers.

Only the heights of the bases of clouds, not of the tops, are available from surface synoptic reports. The February 2 profile was modified by increasing the height of the cloud top of the highest reported cloud. The results are shown in Figure 5.6a and b. The solid line marks the flux calculated with a cloud between 645 and 500 mb; the dashed line shows the flux resulting from moving the cloud top to 466 mb. For infrared radiation, the effect is similar to that of adding a higher layer of cloud; the cloud top is higher and therefore cooler, so it radiates less. The upwelling solar flux is only slightly increased by a thicker cloud. Since rays only interact with clouds at their upper and lower boundaries, extending the highest cloud does not change the number of reflections, as happens when discrete cloud layers are added.

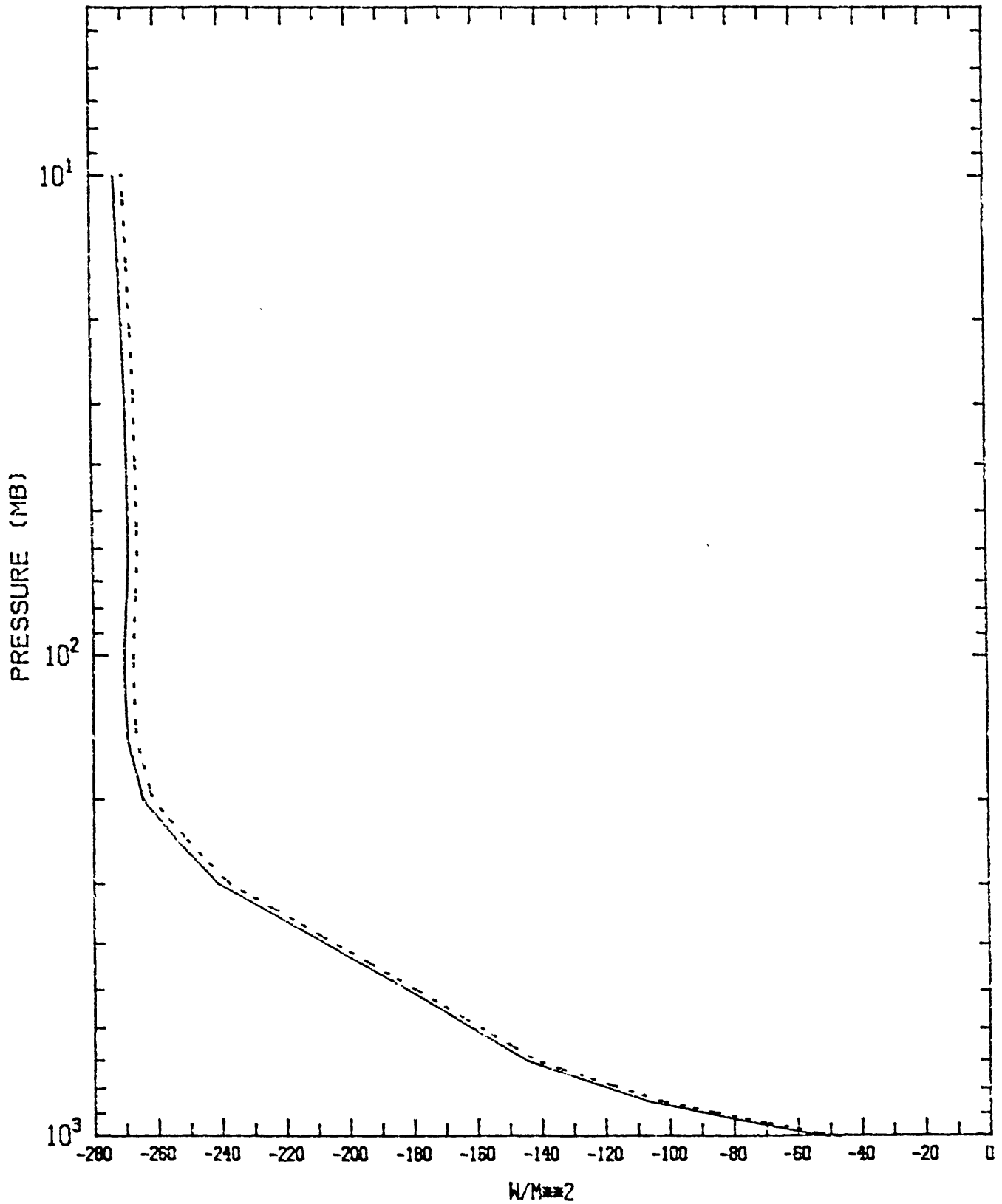
Figure captions

- 5.1 Computed infrared fluxes for the sounding in Figure 4.6. The solid line is the unmodified profile; the dashed line is for a profile with 0.5 higher temperature and 2% lower relative humidity.
- 5.2 As in 5.1; the dashed line is for 0.5 lower temperature and 2% higher relative humidity.
- 5.3 Sounding at the Chinese ship for February 2. Reported cloud layers are between 946-934 mb (10% sky coverage), 775-700 mb (70%) and 645-500 mb (100%)
- 5.4 Computed net thermal infrared (a) and upwelling solar (b) fluxes for the sounding in Figure 5.3. The solid line is for the unmodified profile; the dashed line is for a profile with an extra cloud between 493-430 mb.
- 5.5 As in 5.4; the dashed line is for a profile with an extra cloud between 150-110 mb.
- 5.6 As in 5.4; the dashed line is for a profile with the highest cloud from 645-466 mb (instead of 645-500 mb).

NET FLUXES
CHINESE SHIP 23 JAN 23Z
THERMAL FLUX IN CLEAR SKY NORMAL (SOLID) AND LOW U + HIGH T (DASH)

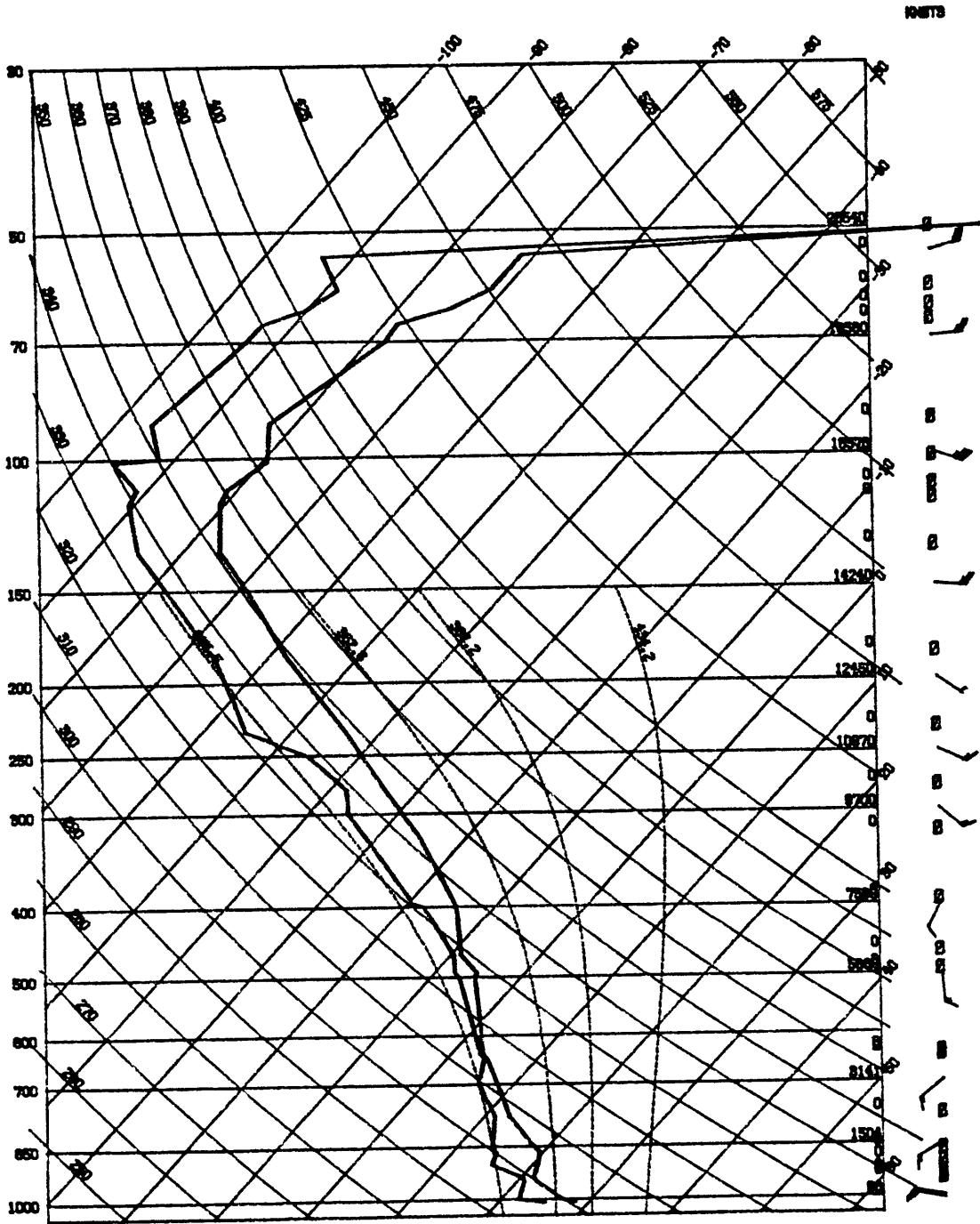


NET FLUXES
CHINESE SHIP 23 JAN 23Z
THERMAL FLUX IN CLEAR SKY NORMAL (SOLID) AND HIGH U + LOW T (DASH)

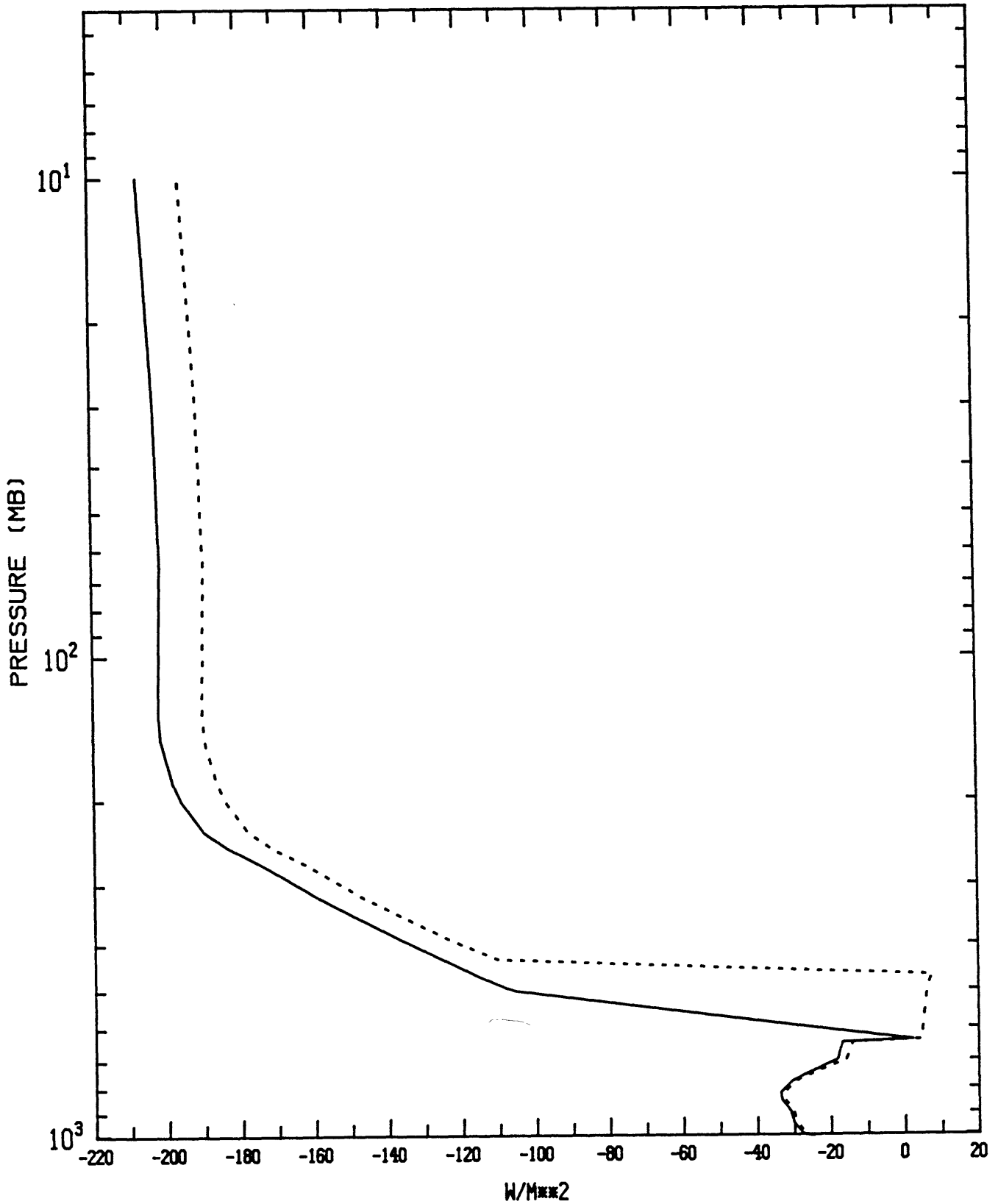


01139 CHINESE SHIP

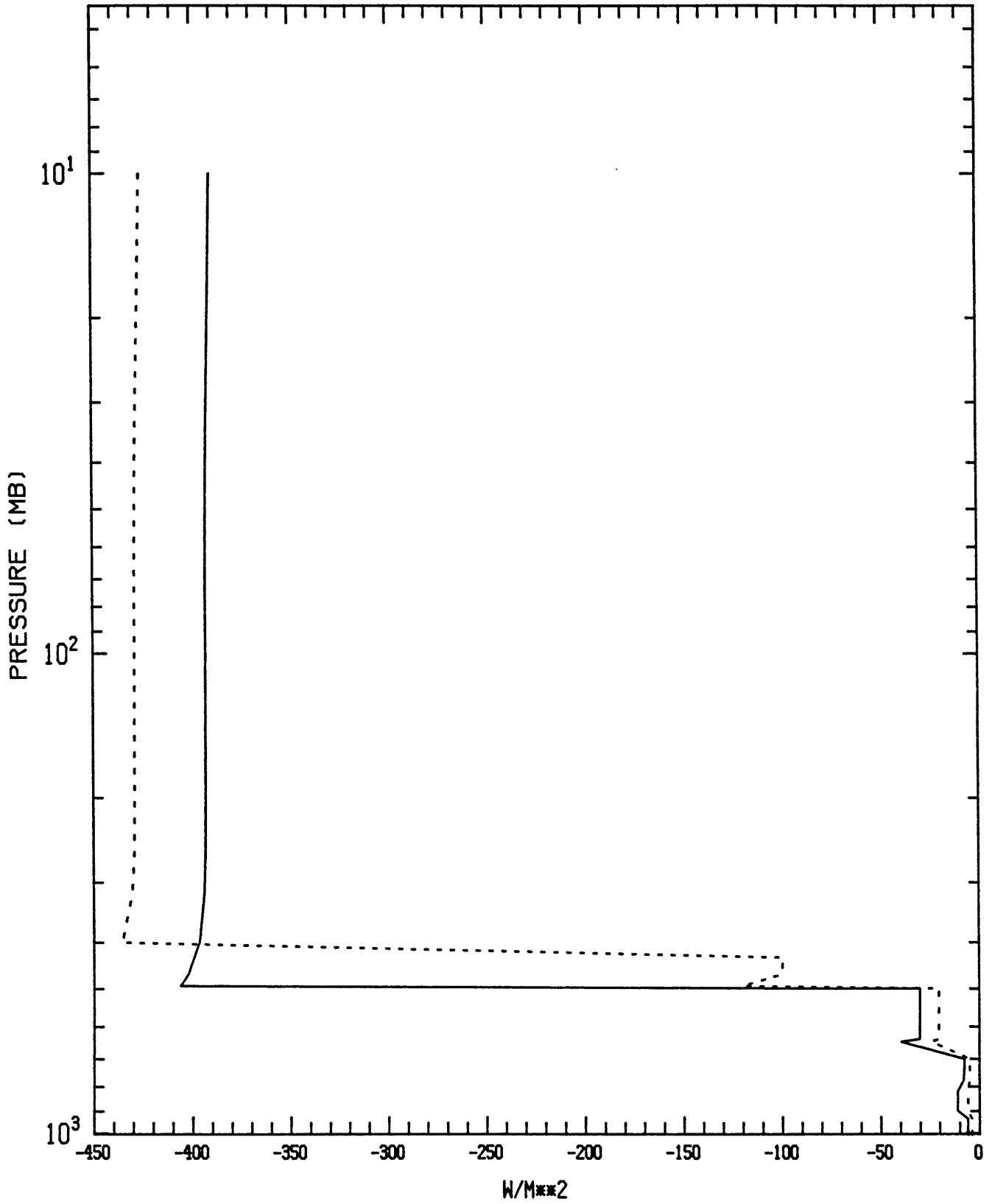
02/02/87 23Z



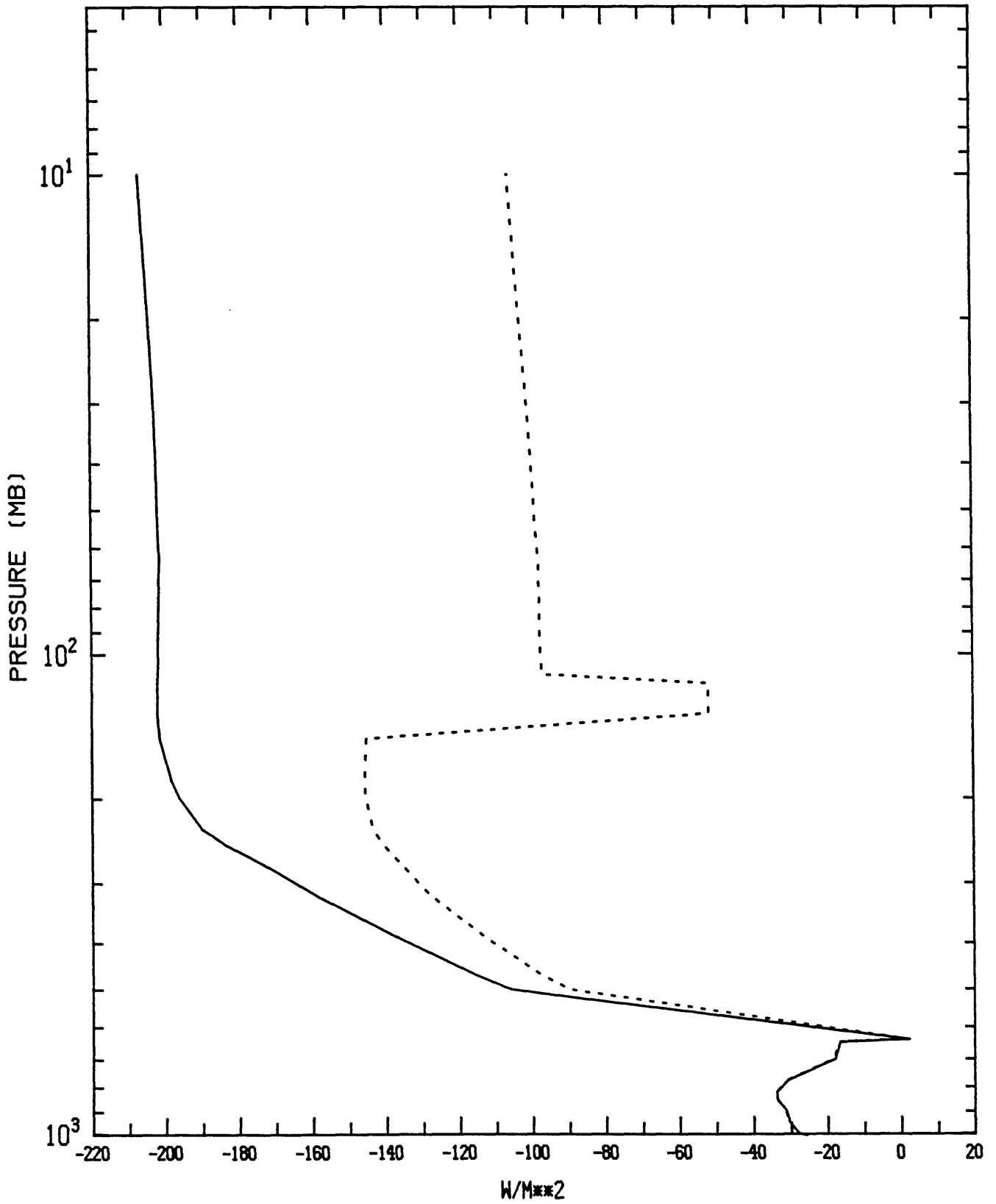
NET FLUX
01139 CHINESE SHIP 03 FEB 00Z FLIGHT 10
THERMAL FLUX WITH (DASH) AND WITHOUT (SOLID) CLOUD LAYER 493-430 MB



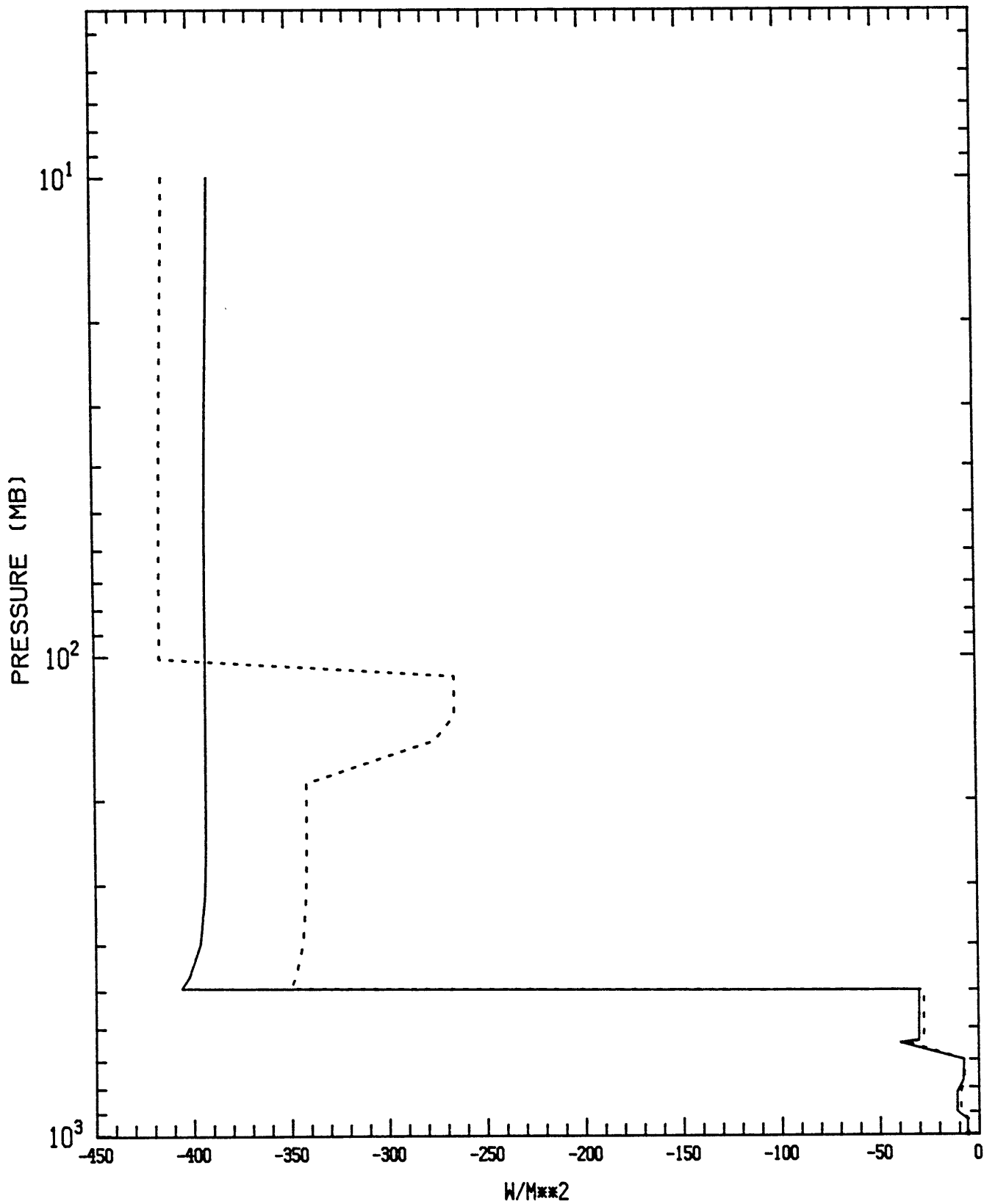
UPWELLING SOLAR FLUX
01139 CHINESE SHIP 03 FEB 00Z FLIGHT 10
SOLAR FLUX WITH (DASH) AND WITHOUT (SOLID) CLOUD LAYER 493-430 MB



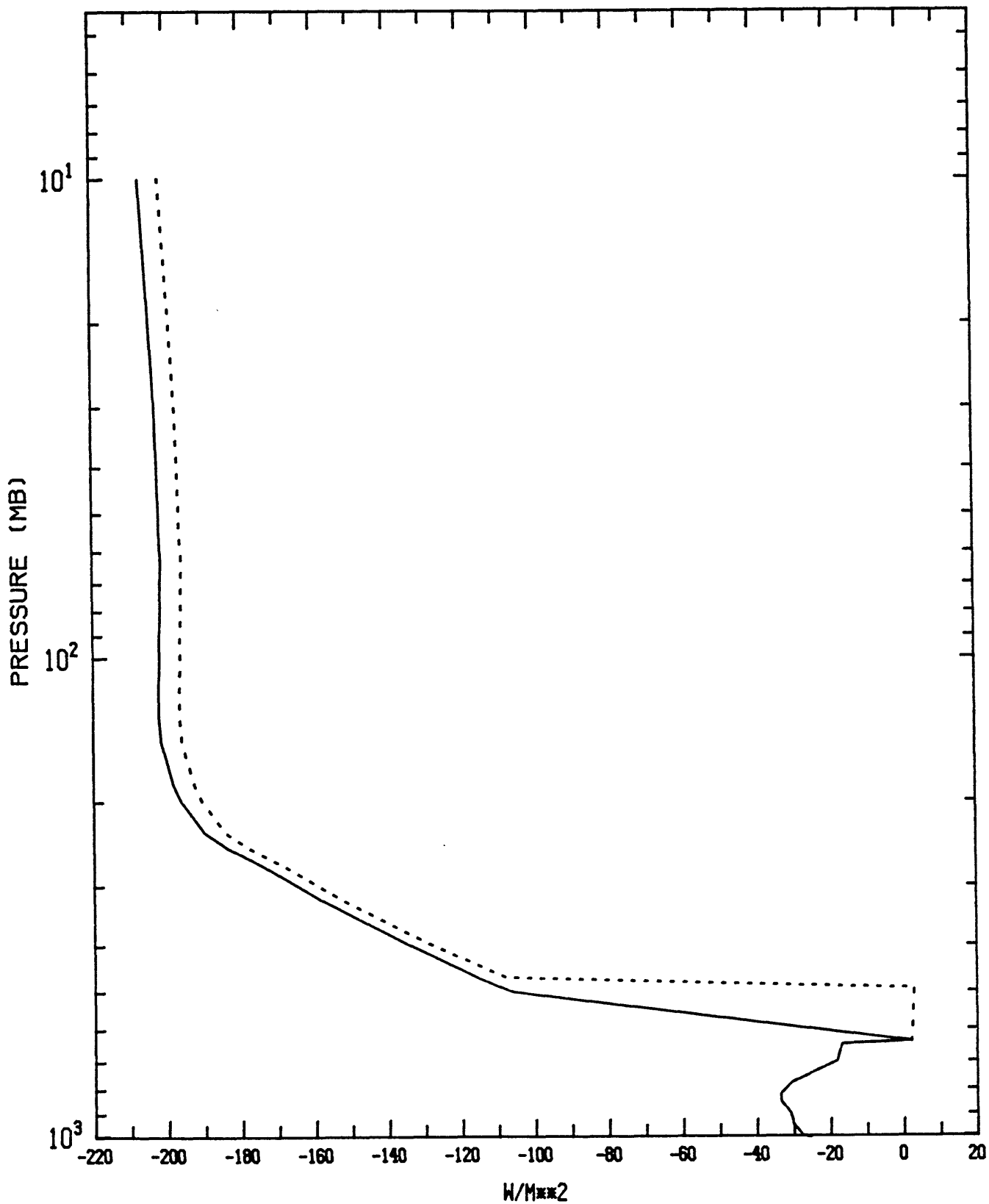
NET FLUX
01139 CHINESE SHIP 03 FEB 00Z FLIGHT 10
THERMAL FLUX WITH (DASH) AND WITHOUT (SOLID) CLOUD LAYER 150-110 MB



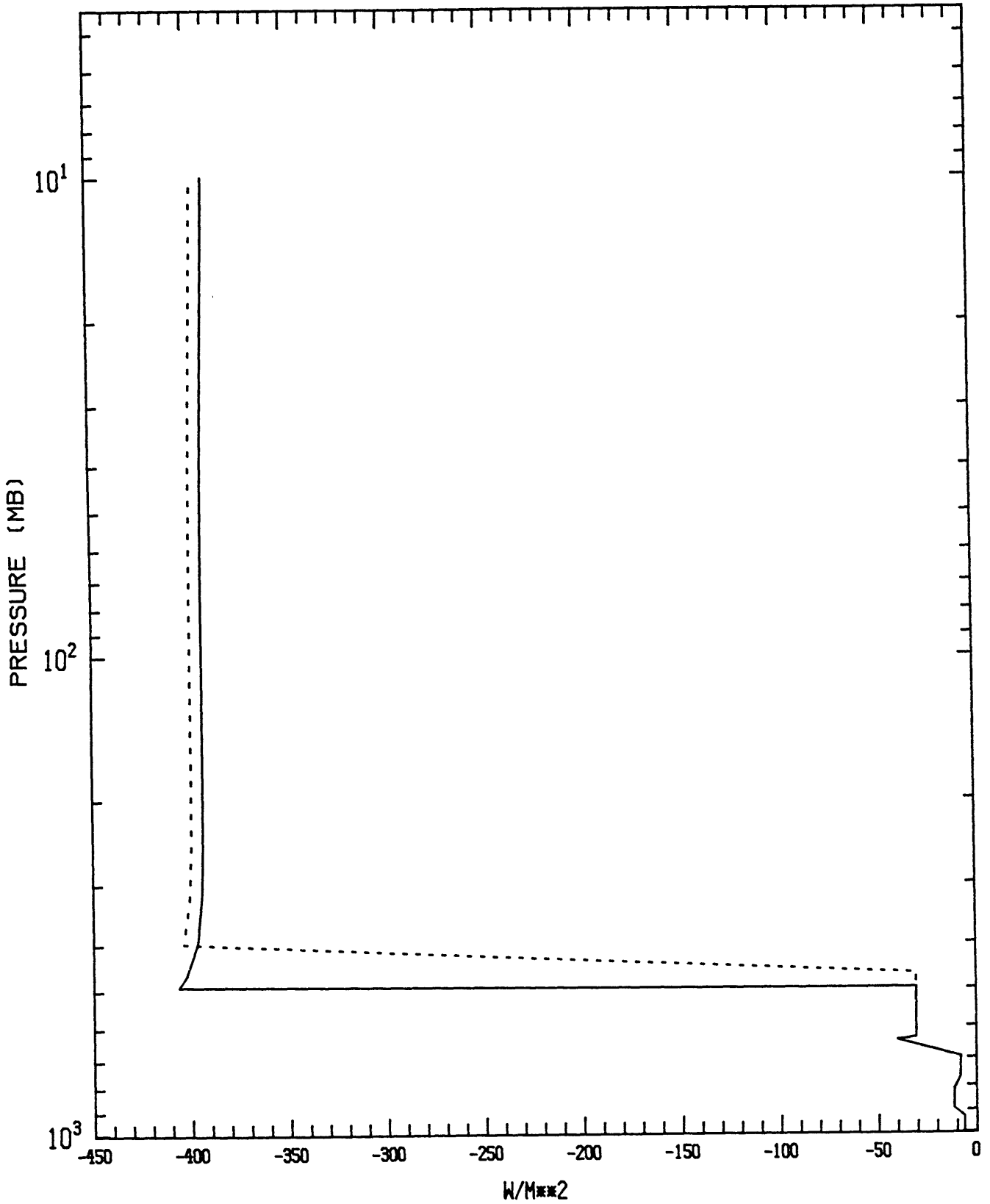
UPWELLING SOLAR FLUX
01139 CHINESE SHIP 03 FEB 00Z FLIGHT 10
SOLAR FLUX WITH (DASH) AND WITHOUT (SOLID) CLOUD LAYER 150-110 MB



NET FLUX
01139 CHINESE SHIP 03 FEB 00Z FLIGHT 10
THERMAL FLUX WITH THICK (DASH) AND THIN (SOLID) HIGHEST CLOUD LAYER



UPWELLING SOLAR FLUX
01139 CHINESE SHIP 03 FEB 00Z FLIGHT 10
SOLAR FLUX WITH THICK (DASH) AND THIN (SOLID) HIGHEST CLOUD LAYER



6. Comparison of computed and measured fluxes

6.1. A first comparison

A preliminary comparison was made by running the radiation model for each flight with the assumption that the field of view sees a random ensemble of clouds representative of the total cloud cover. The combination of radiosonde and aircraft data described in section 4.2 was used for flights 10 and 12, while radiosonde data only was used for flight 9, as the aircraft data were unavailable. The computed radiative flux is shown in Figures 6.1-6.3a and b as a function of pressure. The negative values reflect the coordinate system used; downward flux is positive, so net upwelling radiation is shown as a negative flux.

The fluxes obtained by the radiometer on those flights are shown in Figures 6.1-6.3c and d. These plots are of observed net upwelling flux (for the thermal band) or upwelling flux (for the solar band) as a function of time; Figures 6.1-6.3e are plots of the pressure measured at aircraft altitude for each flight. Each flight is discussed individually below.

Flight 9: The target cloud for this flight was the upper level outflow from the dissipating Cyclone Connie to the west, which lay over lower clouds. The ER-2 traversed the cloud several times at different heights; Flight track data indicate that the periodic variation of observed net upwelling flux is due to crossing back and forth over the cloud band; inspection of Figures 6.1c and e shows no identifiable dependence on height (pressure). The computed flux also does not vary much with pressure between 150 and 50 mb, averaging 209 Wm^{-2} for computed thermal flux. This is much

higher than the average observed thermal flux, but comparable to the largest observed values, which correspond to regions of low cloud. The average computed upwelling solar flux over the same vertical region is 262 Wm^{-2} , which is close to the average observed upwelling solar flux.

Flight 10: The ER-2 flew to an active cumulonimbus band northeast of Gove. There is an apparent pressure dependence seen in figures 6.2c and d as the flight level changes from about 72 mb to 86 mb and from 72 mb to above 58 mb. However, the fluxes from the first flight segment at 72 mb (prior to 87500 GMT seconds) differ from those from the second (around 91000 GMT seconds), by about 70 Wm^{-2} for the infrared instrument and 200 Wm^{-2} for the solar radiometer, which suggests that there is no real pressure dependence. The apparent correlation is probably because the pilot approached the high cloud and ascended in order to fly over it.

The relationships between the observed and computed fluxes for this flight sharply contrast with those from flight 9. The calculated thermal flux averages 204 Wm^{-2} , which is much lower than the largest observed values. The calculated upwelling solar flux averages 396 Wm^{-2} ; this is comparable to the largest observed values, which correspond to the region directly above the cumulonimbus band.

Flight 12: The target of this flight was Cyclone Jason, in the Gulf of Carpentaria. The average computed thermal flux of 208 Wm^{-2} is somewhat higher than the peak observed value, 185 Wm^{-2} ; the computed upwelling solar flux averages 344 Wm^{-2} , which is higher than the average observed upwelling solar flux, but

closer to the average than to the maximum. These relationships are similar to those found for flight 9.

The calculated net upwelling thermal flux was nearly the same in each case; since clouds are modeled as thermally black, the flux above a cloud depends most strongly on the height of the highest cloud top, decreasing with higher cloud. The level of the highest cloud top ranged from 597 mb (flight 12) to 433 mb (flight 9), although in the latter case, the cloud did not cover the entire sky, so the resulting thermal flux was greater than would be expected for a cloud of that height. In all cases, the calculated thermal flux was greater than the average observed flux. For flights 9 and 12, the calculated flux was comparable to the highest observed values, which suggests that there were higher clouds present that were not reported in the synoptic observations. The greatest observed thermal flux was measured during flight 10; this value is consistent with the satellite photograph for that segment of the flight, which indicates low cloud or clear sky. Since the composite cloud profile for flight 10 does not include any fraction of low cloud alone, or clear sky, the computed flux is lower than the highest observed values. Again, this implies that the actual cloud height for the cloud band was higher than that used for the model. This is supported by the satellite photographs, which were received after much of this work had been completed.

It is more difficult to assess the solar results; since clouds partially transmit in this part of the spectrum, all cloud layers are important. Although in general the computed upwelling solar flux increases with the height of the highest cloud, adding lower level

clouds increases the flux also, since this increases the effective surface albedo. Therefore, the solar calculations are more sensitive to the assumed cloud structure than the thermal calculations are. Adding cloud above the highest reported cloud level moves the modelled values away from the average measured flux, but this depends somewhat on the sky coverage, height and thickness assumed for the added cloud.

Clearly, the assumption of a representative cloud ensemble in the field of view is not appropriate for these flights, since the cloud boundaries are apparent in the measurements. It is misleading to match these calculated profiles with the average measured flux; the cloud distribution over the flight path is not likely to be the same as that observed at any station, since these flights focus on particular clouds. For this reason, fluxes were calculated for the cloudiest regions, and compared with the observations from these regions only.

6.2 Comparison over maximum cloud

Based on the satellite photographs and brightness temperatures, the segment of each flight over the highest, densest cloud was identified. In each case, the observed flux did not vary much during that flight segment, and represented a clear extreme -- a minimum for the thermal flux, a maximum for the upwelling solar flux. The location of each "maximum cloud" segment, and the average net infrared flux and upwelling solar flux observed in that segment, is given in Table 6.1.

The cloud was modelled using the second scheme described in Section 4.4, and assumed to fill the entire field of view of the radiometer (effectively 100% sky coverage). Since the cloud profile represents only a "best guess", several possible profiles were created for each flight; a summary of the profiles appears in Table 6.2. The cloud structures were not specifically "tuned" to produce the best results; however, several model runs were made for each flight, with different combinations of the cloud layers which were likely to be present (since the satellite picture only gives information about the highest level of cloud), and those resulting in fluxes differing from the measurements by more than 50% were not used. Each flight is discussed individually below.

Flight 9: Because the ER-2 traversed the cyclone outflow several times, at different heights, there were many segments of maximum cloud at nearly regular intervals. Three were chosen as examples; one at 115 mb, one at 105 mb, and one at 70 mb. Figure 6.4a shows the thermal flux computed using two possible cloud profiles. There is little difference between the results of the two profiles, and the average computed flux over the three levels is equal to the average of the flux measurements at those levels, although the variation with height is much smaller. Figure 6.4b shows the upwelling solar flux calculated from the same profiles; again, the variation with height of the observed flux is large, but the computed flux does not change with height above the highest cloud. The large variation in measured values may be partially because of the time between the steps of the profile; an hour passed between 115 mb

and 105 mb, and more than two hours between the 105 mb and 70 mb steps, during which the cloud could evolve.

Flight 10: The location of the cumulonimbus band is easily seen in the data. The large "bumps" in the data at approximately 89000 and 90000 GMT seconds correspond with turns made by the aircraft; the segment of maximum cloud lies between these two turns. Figures 6.5a-b show the thermal and solar flux calculated for this flight with three different possible cloud profiles. Again, there is more variation among the results of the solar calculations than of the thermal calculations. The computed thermal flux tends to be low; it could be increased by assuming a lower cloud top for the highest cloud or a lower emissivity.

Flight 12: The flight track crosses Cyclone Jason several times, with the segment of maximum cloud just after a turn, seen as a bump in the data at approximately 9600 GMT seconds. Figures 6.6a-b show the thermal and solar flux calculated using two possible cloud profiles. In contrast to the previous flight, the computed infrared flux is a little high, but still well within instrument error. The solar results are much better for the second profile.

The summary of computed and observed fluxes in Table 6.3 suggests that they correspond to within instrument error. This result, however, is largely due to the assumptions about cloud locations and properties. Conceivably, an a posteriori cloud model could be devised which would result in a perfect match between measured and calculated fluxes, but there would be no guarantee that this cloud structure was actually present.

Table 6.1. Locations of flight segments over maximum cloud, and the average observed flux in those segments.

Flight	Start GMT sec	End GMT sec	Pressure (mb)	Measured flux (Wm^{-2})	
				Thermal	Solar
9	84510	84780	115	75	250
	86970	87750	105	85	350
	96330	96750	70	115	480
10	88960	89620	87	115	400
12	9685	10105	92	110	480

Table 6.2. Summary of assumed maximum cloud profiles.

Flight	Profile	Low cloud	Middle cloud	High cloud
9	1	935-769	640-433	250-119
	2	none	640-433	250-119
10	1	989-879	655-508	396-136
	2	none	655-508	396-136
	3	989-879	none	396-136
12	1	none	597-424	173-110
	2	990-955	597-424	173-110

Table 6.3. Results of the radiation program for "maximum cloud".
 T=thermal, S=solar flux in Wm^{-2} .

Flight 9:

Pressure (mb)	Profile 1		Profile 2		Measured	
	T	S	T	S	T	S
115	91	436	91	377	75	250
105	91	436	91	377	85	350
70	92	435	91	375	115	480

Flight 10:

Pressure (mb)	Profile 1		Profile 2		Profile 3		Measured	
	T	S	T	S	T	S	T	S
87	97	426	96	367	104	373	115	400

Flight 12:

Pressure (mb)	Profile 1		Profile 2		Measured	
	T	S	T	S	T	S
92	116	375	117	450	110	480

6.3. Less dense cloud

While the highest, densest cloud was easily identified and modelled, it was harder to find a match between observed and computed fluxes over the peripheral parts of the cloud bands. Part of the reason was that it was difficult to tell from the satellite pictures if these clouds were less dense or simply lower than the maximum cloud; these cases would have to be modelled differently. Attempts to construct cloud profiles were abandoned when it became clear that this was a case of fitting the data to match the model.

6.4. The clear air flight

Solar data only was available for the single clear air flight, flight 7. The target for this flight was a cumulonimbus anvil over the southeastern edge of the Gulf of Carpentaria, but much of the flight (prior to 90000 GMT seconds) was in apparently clear skies. Figures 6.7a-b show the calculated upwelling solar flux profile and the observed upwelling solar flux as a function of flight time.

Clearly, the computed values for the upwelling solar flux are much smaller than those observed; the small values are due to the low sea surface albedo (3%) used in the model. There are several possible explanations. First, it is evident from the measurements that there is some spatial variation in flux. This could be from small clouds; 1/8 cloud was reported by the Chinese ship, and there appears to be low cloud in the satellite picture. Low cloud would be so far below the aircraft that, in contrast to the cases discussed above, where high cirrus was always present, the instrument's field of view would never be cloud-filled or cloud-free. In addition to

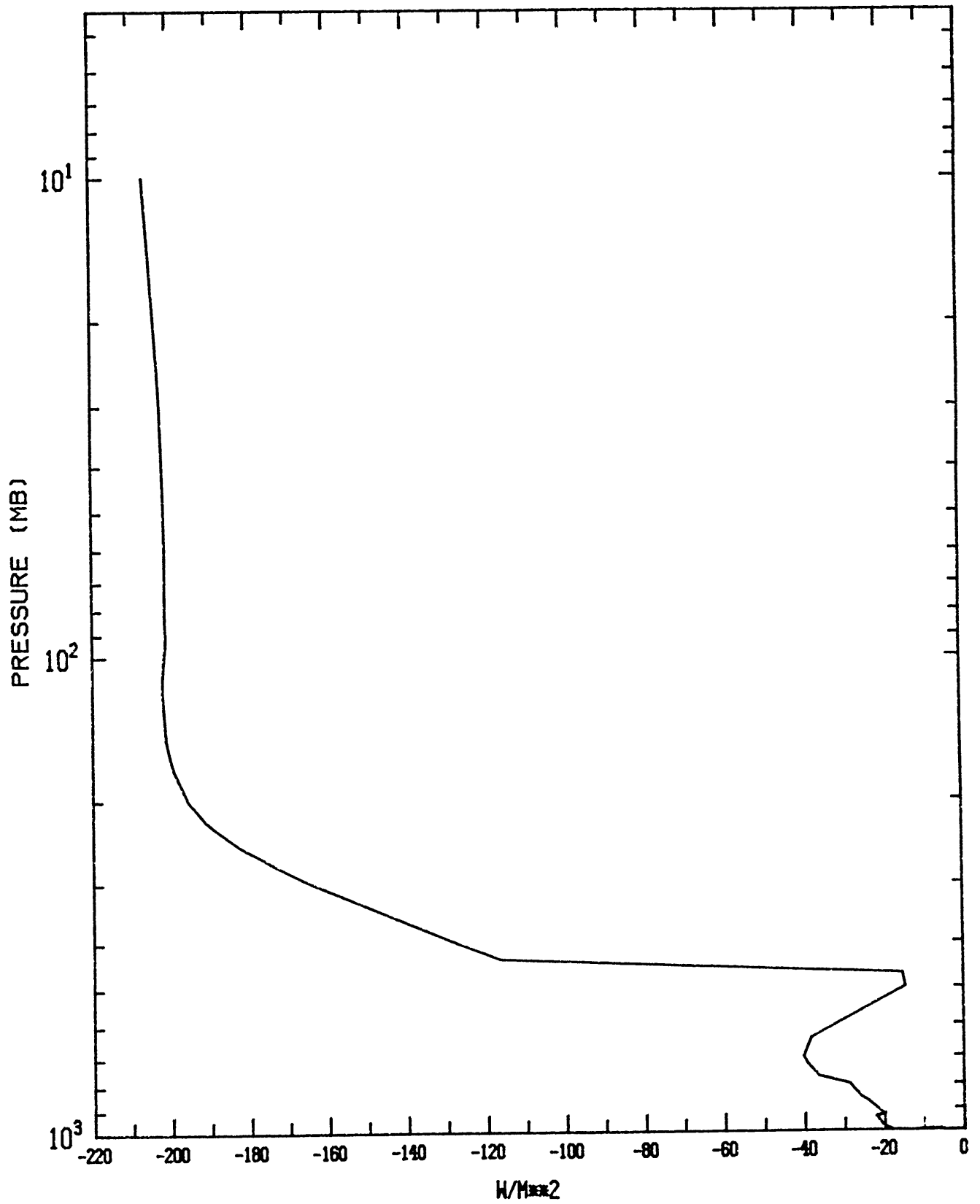
contributing to the total albedo, the clouds would make the solar beam diffuse; the sea surface albedo for diffuse radiation is about triple the albedo for the nearly normal beam (Payne, 1972). This would explain why even the lowest observed values are significantly higher than the computed fluxes. If a layer of low cloud between 970 and 930 mb, covering 1/8 of the sky, is added to the profile, the computed solar upwelling flux increases to 50 Wm^{-2} .

Some increase in the effective albedo may be due to the aerosol, which is neglected in the model. Houghton (1985) gives the transmissivity of the aerosol over ocean as 0.86-0.94. The partition of the remainder into absorption and scattering is uncertain; he cites several computations which indicate that the amount of upward scattering is very small.

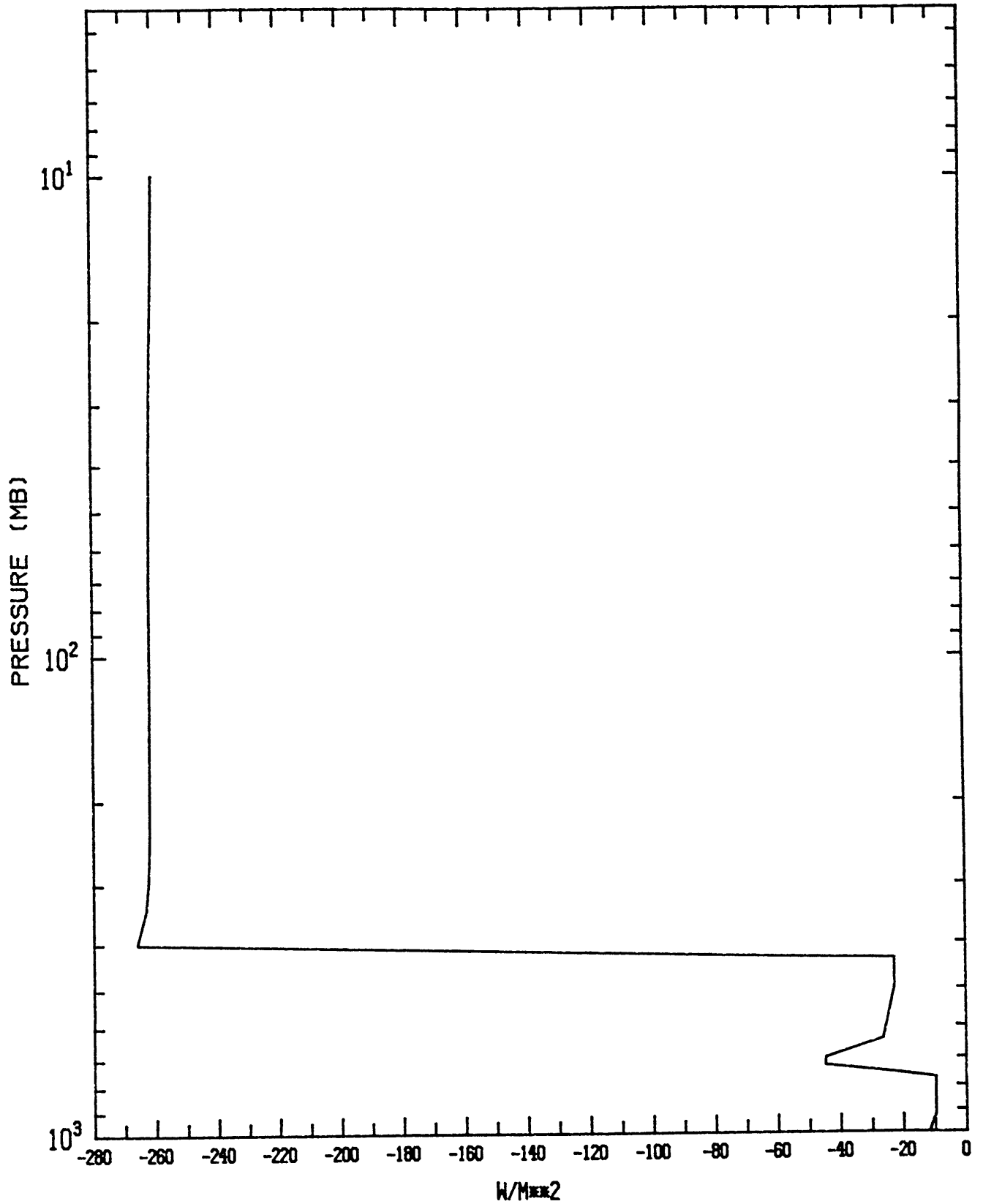
Figure captions

- 6.1 Computed net thermal infrared (a) and upwelling solar (b) flux as functions of pressure, measured net thermal infrared (c) and upwelling solar (d) flux as functions of flight time, and measured pressure as a function of flight time (e), for flight 9.
- 6.2 As in 6.1, for flight 10.
- 6.3 As in 6.1, for flight 12.
- 6.4 Computed net thermal (a) and upwelling solar (b) flux for flight 9, using two possible cloud profiles. The flux for profile 1 is shown by a solid line; that for profile 2, by a dotted line. The structure of each cloud profile is given in Table 6.2.
- 6.5 As in 6.4, for flight 10. The irregularly dashed line is the flux for profile 3.
- 6.6 As in 6.4, for flight 12.
- 6.7 Computed upwelling solar flux as a function of pressure (a) and measured upwelling solar flux as a function of flight time (b) for flight 7.

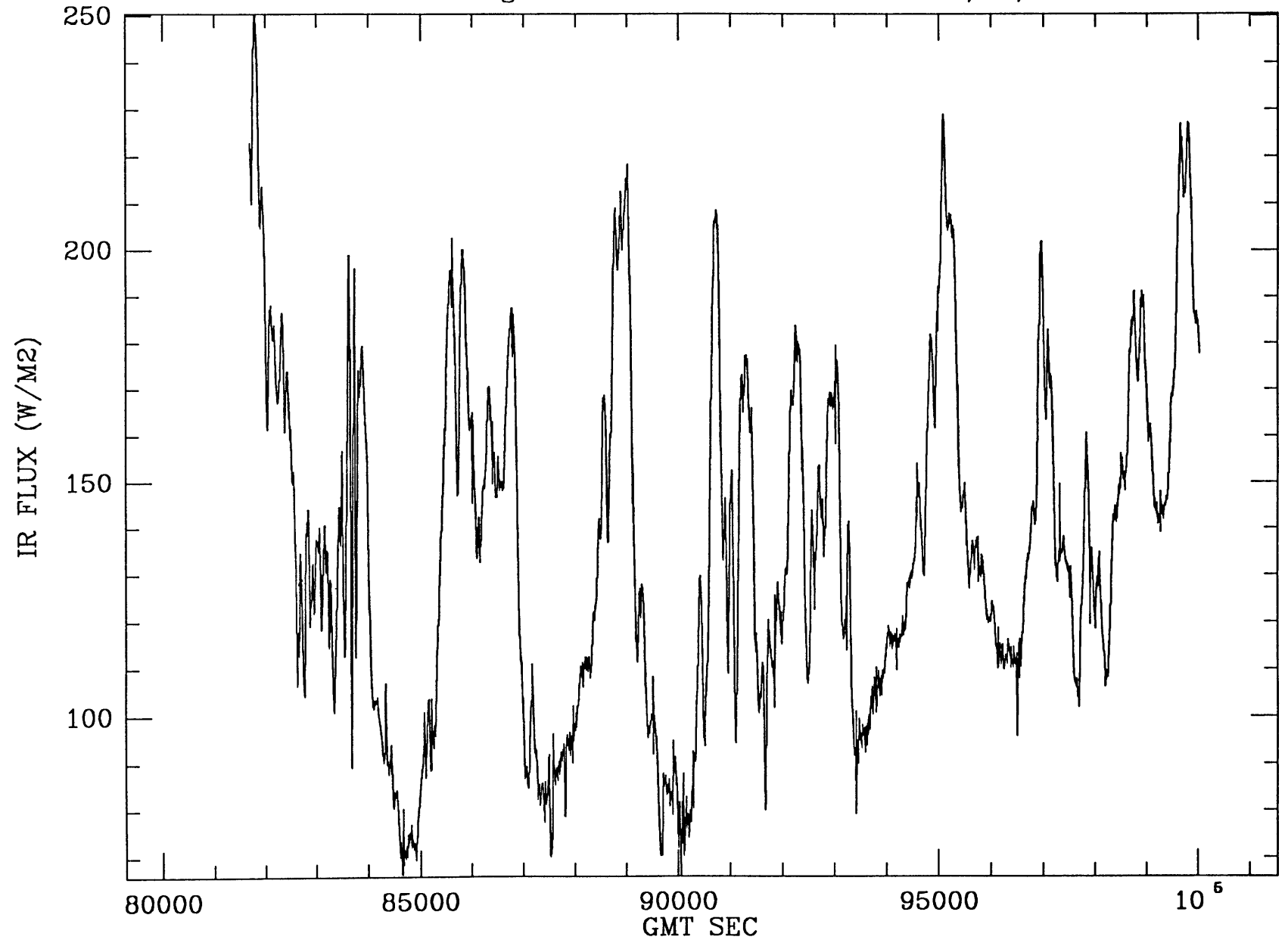
NET FLUX
94120 DARWIN 31 JAN 00Z FLIGHT 9
THERMAL FLUX



UPWELLING SOLAR FLUX
94120 DARWIN 31 JAN 00Z FLIGHT 9
SOLAR FLUX

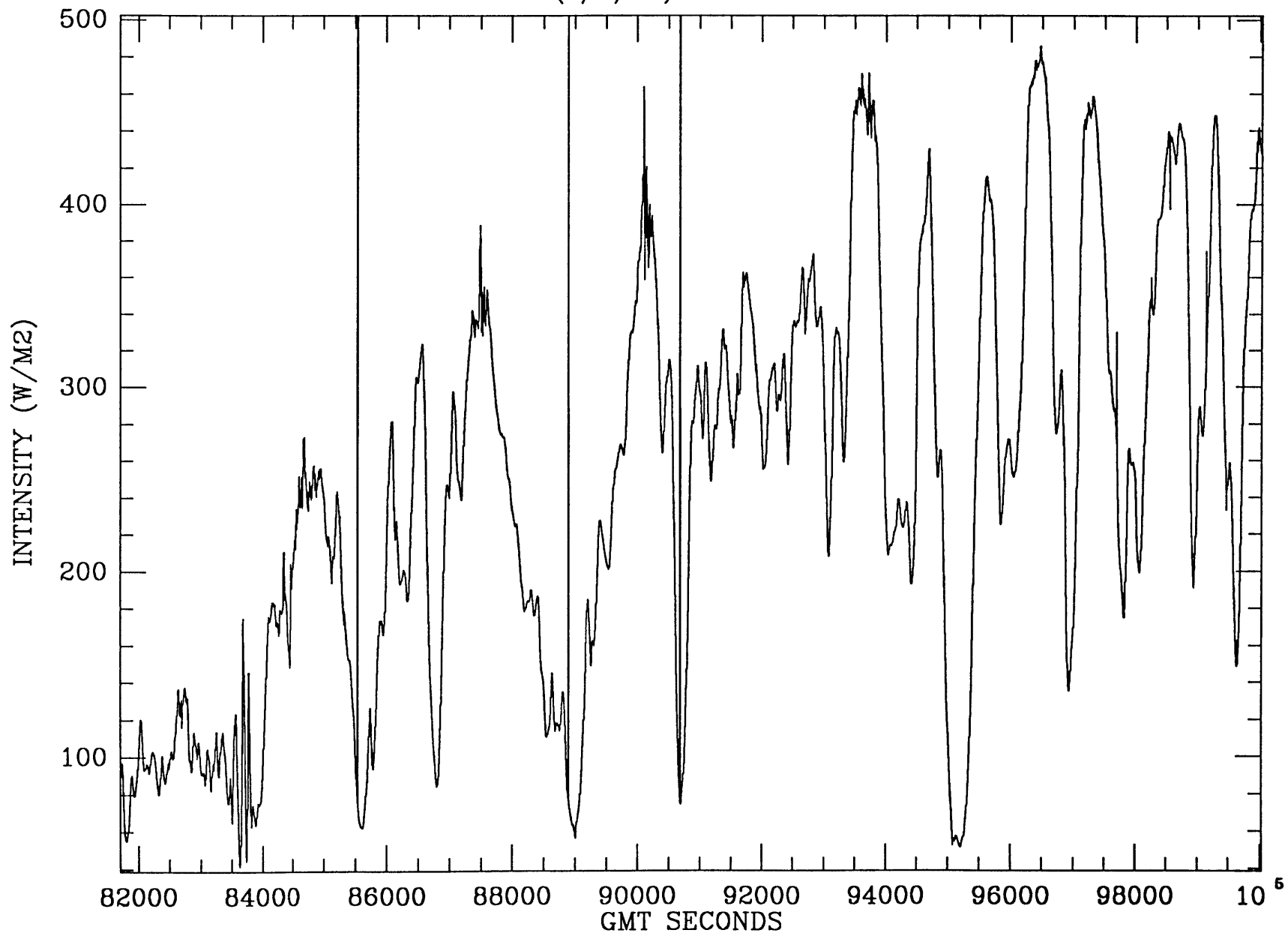


STEP <I> flight 9 NET UPWEL. IR FLUX: 02/01/87

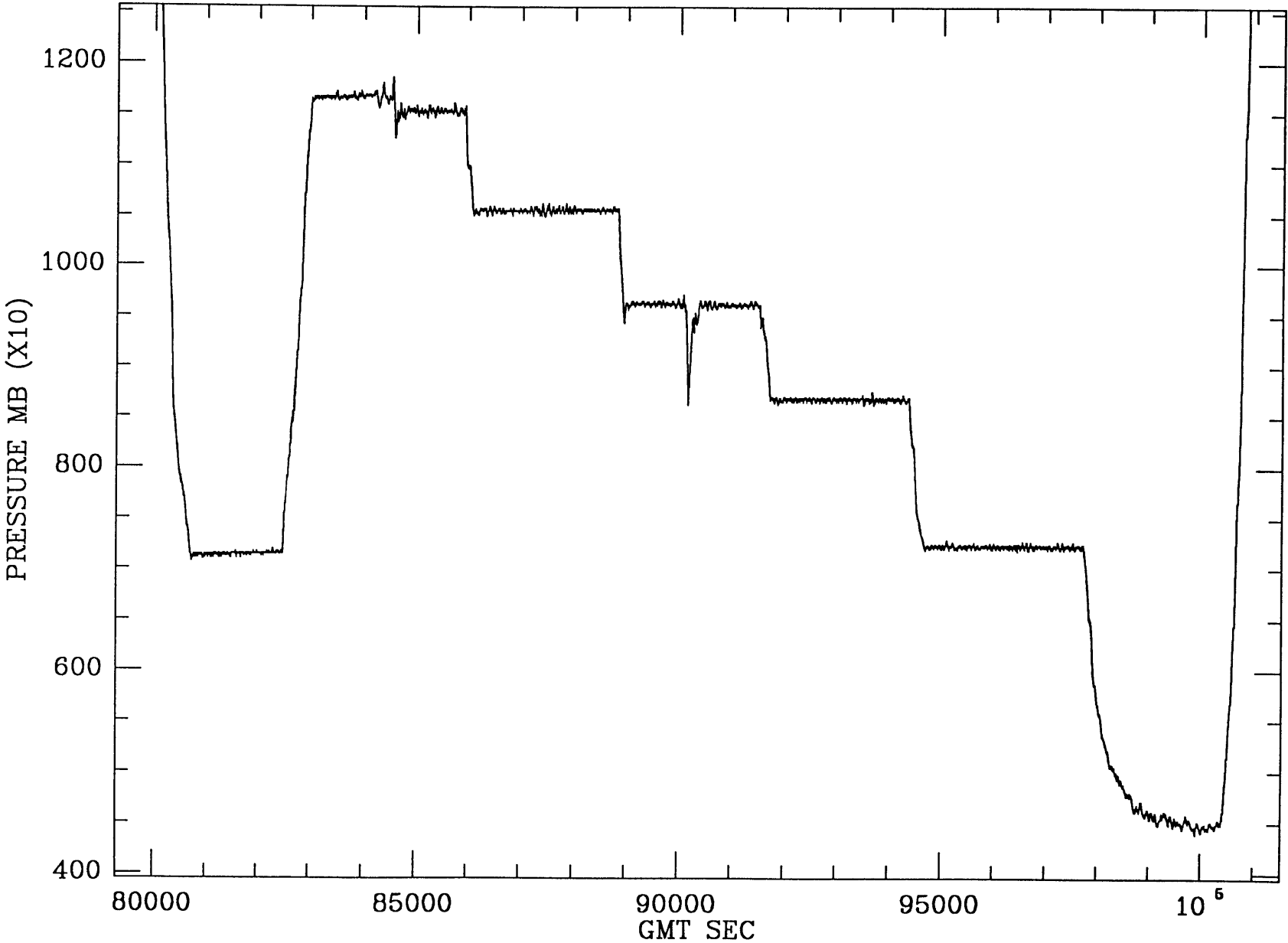


69 / Figure 6.1c

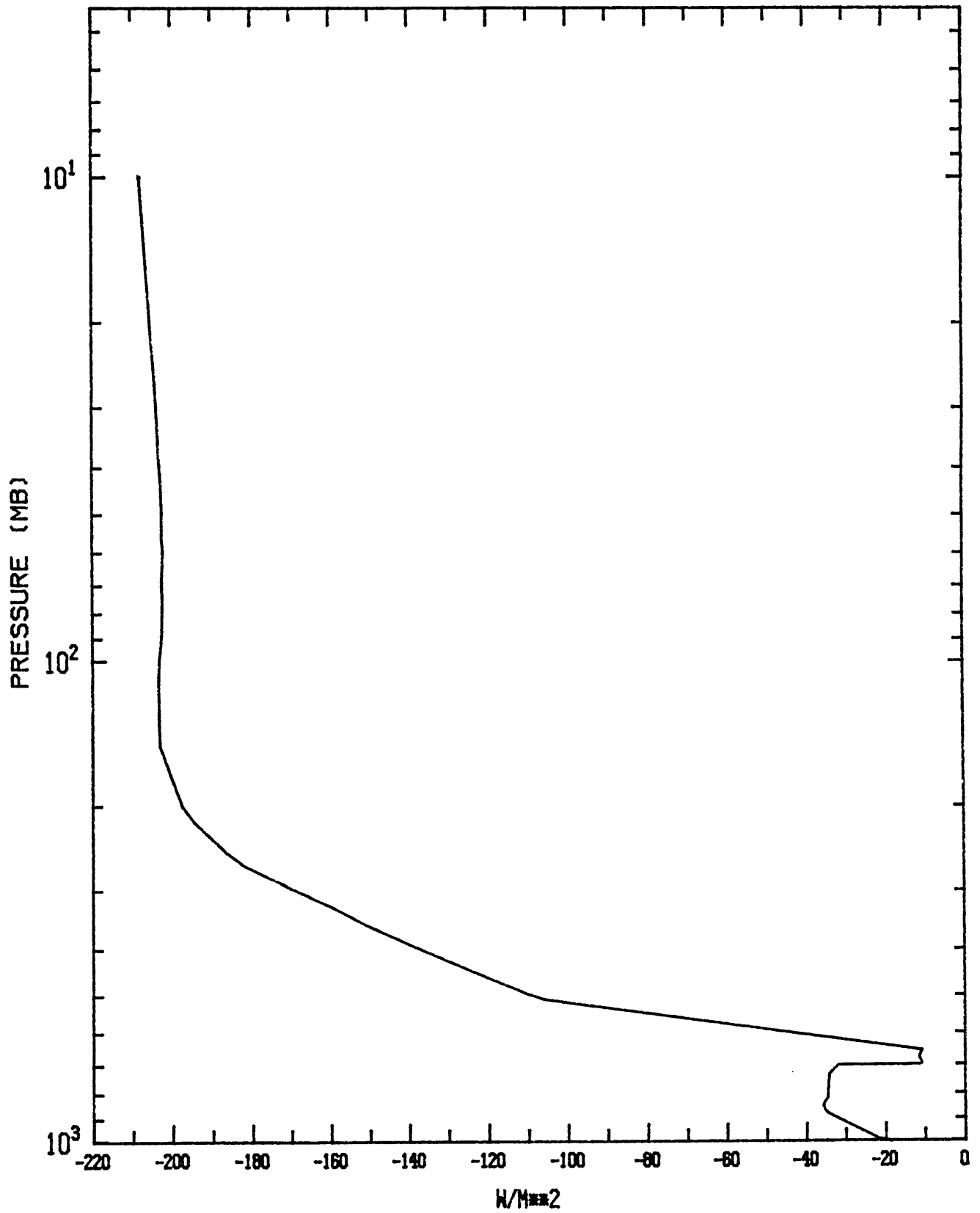
STEP FLIGHT 9 (2/1/87) - UPWELLING SOLAR FLUX



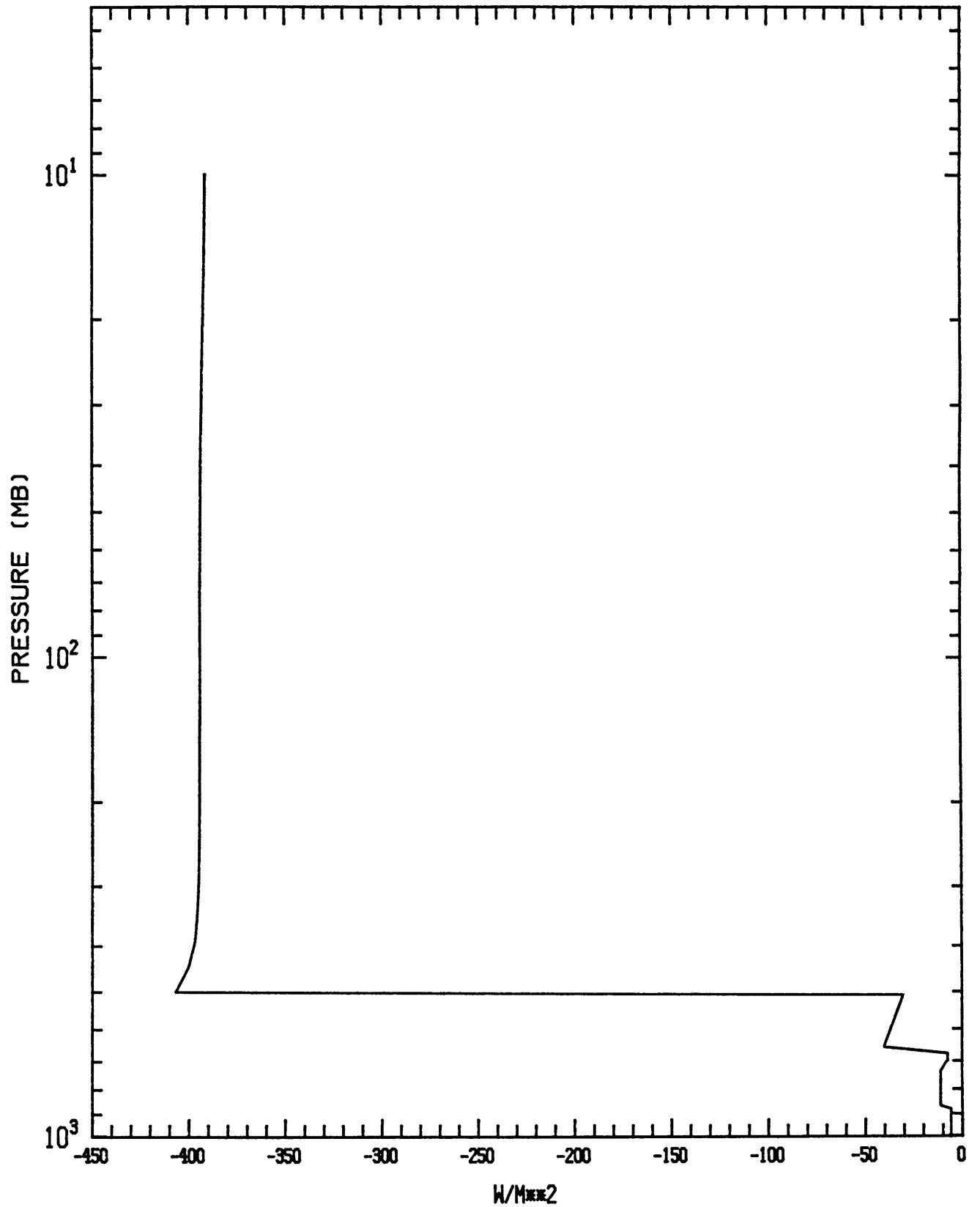
Pressure mb (x 10) ("PT" DATA): 02/01/87



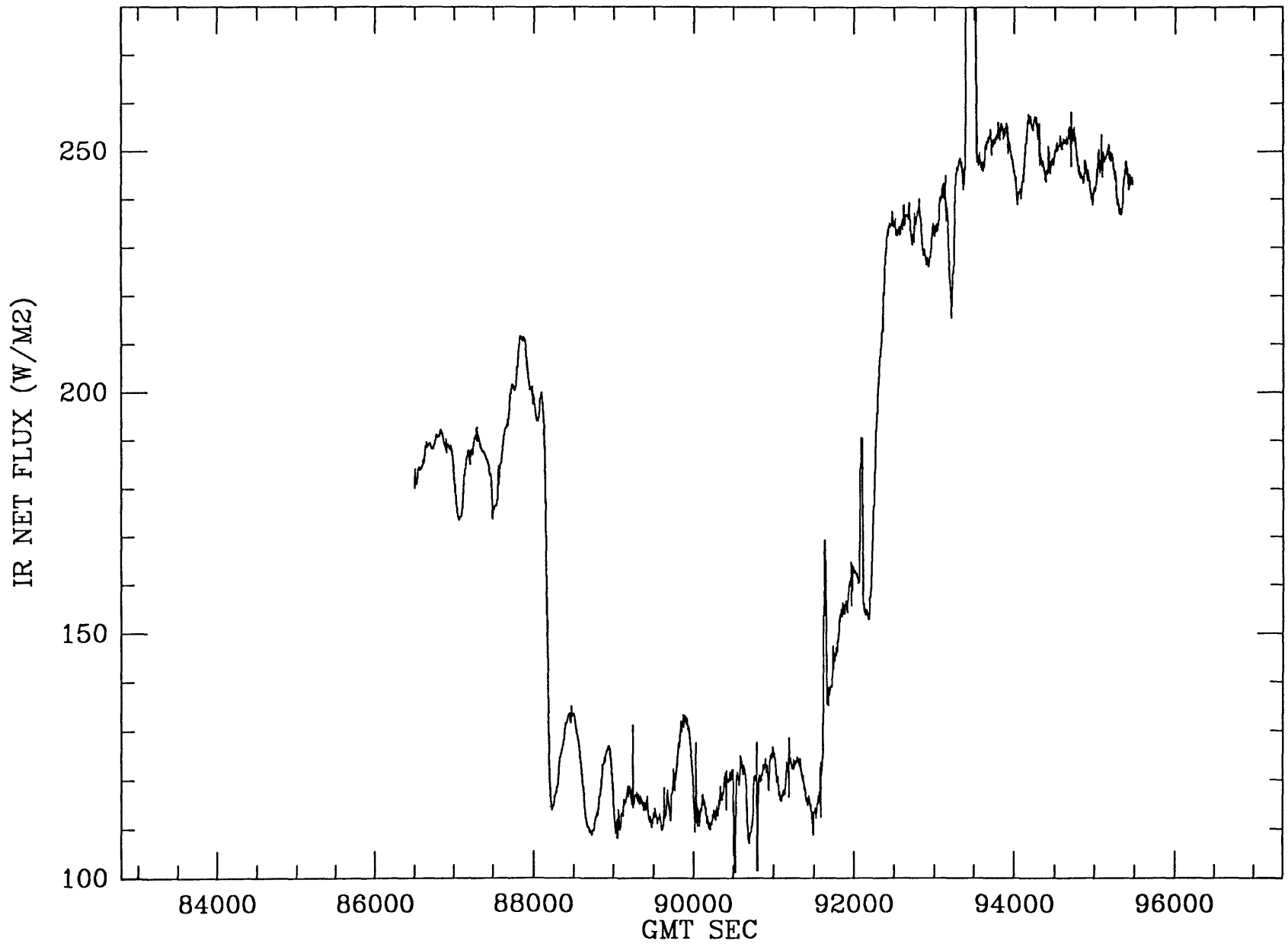
NET FLUX
94150 GØVE 03 FEB 00Z FLIGHT 10
THERMAL FLUX



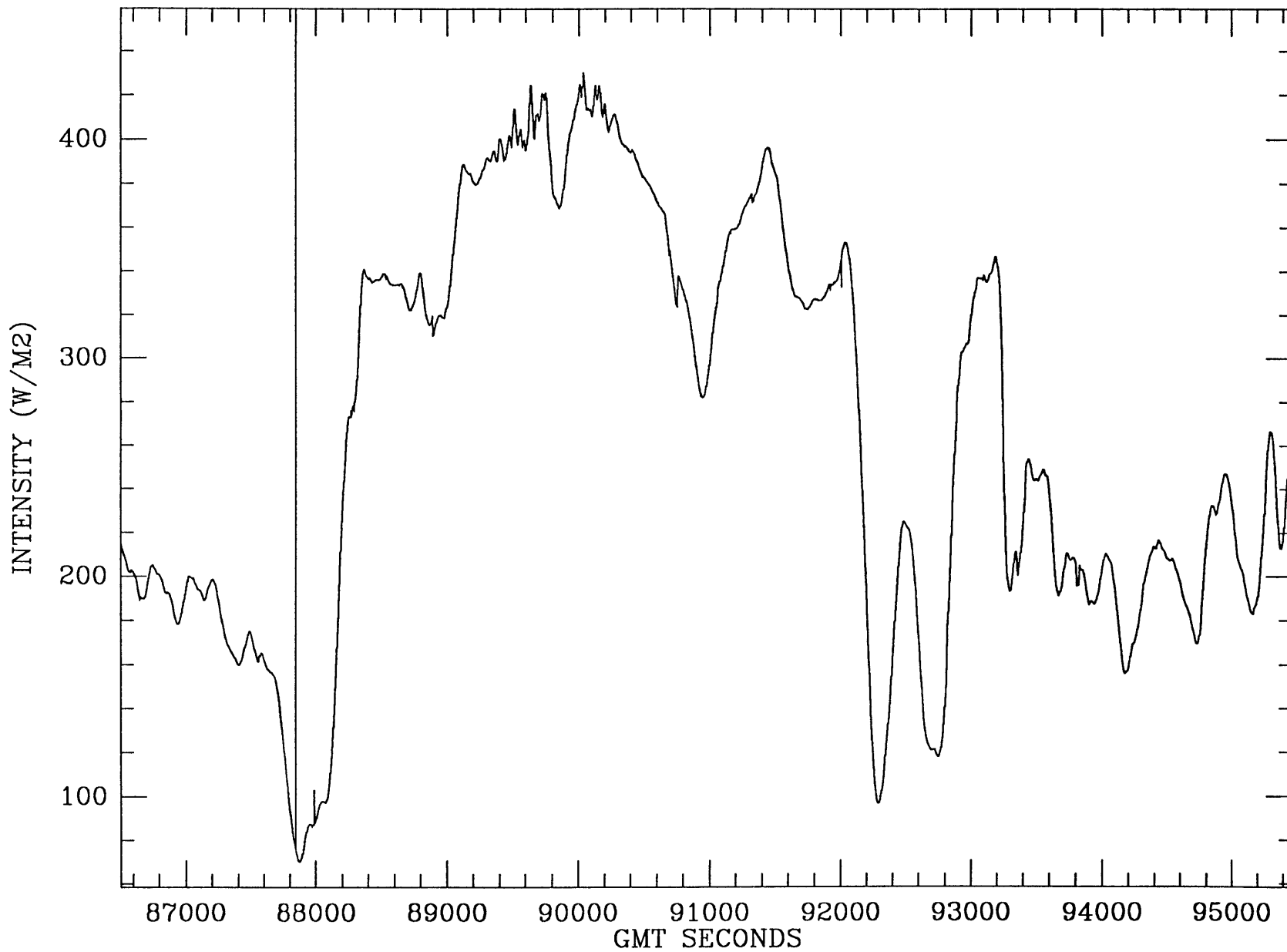
UPWELLING SOLAR FLUX
94150 GØVE 03 FEB 00Z FLIGHT 10
SØLAR FLUX



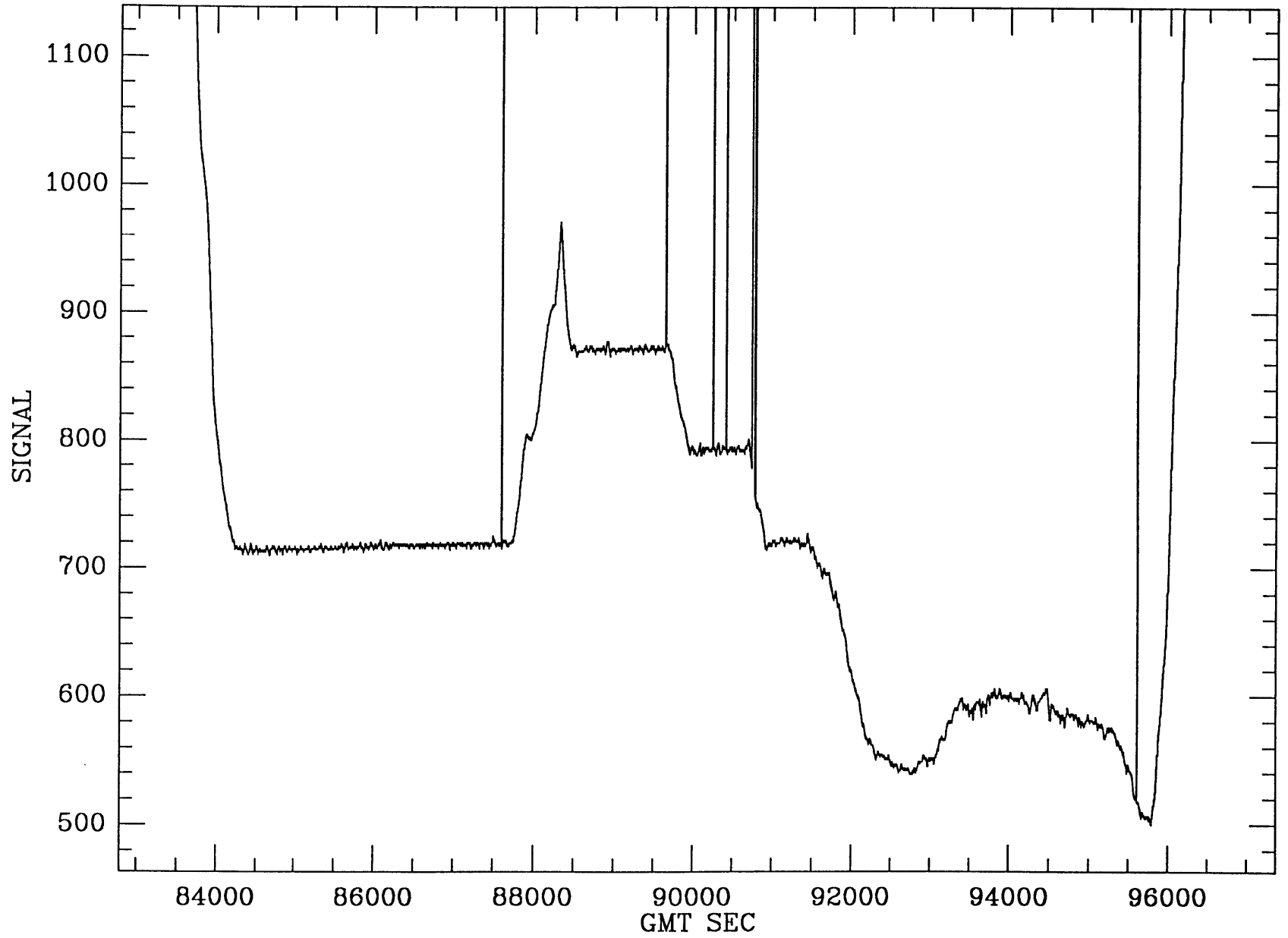
STEP <I> flight 10 NET UPWEL. IR FLUX: 02/03/87



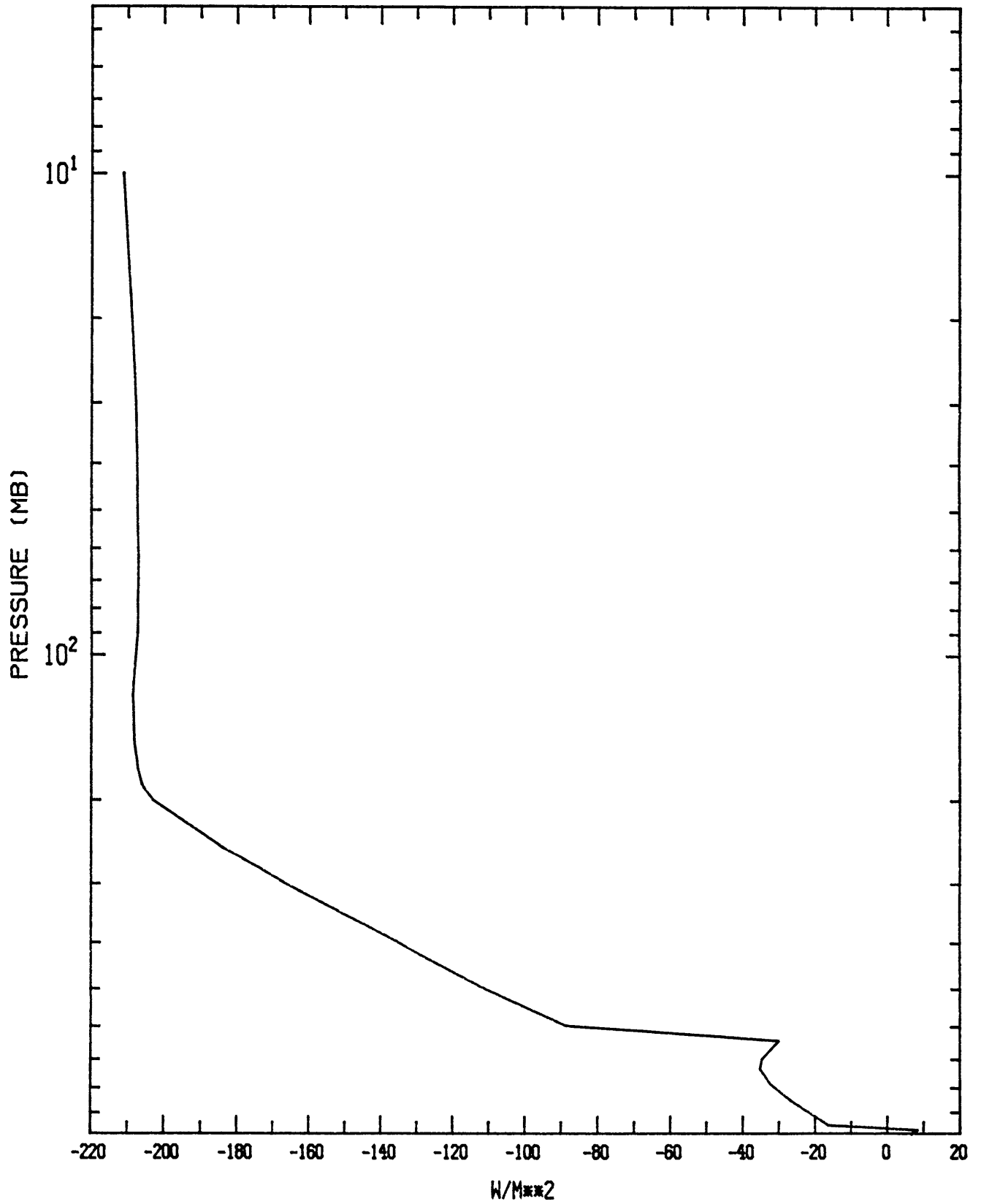
STEP FLIGHT 10 (2/3/87) - UPWELLING SOLAR FLUX



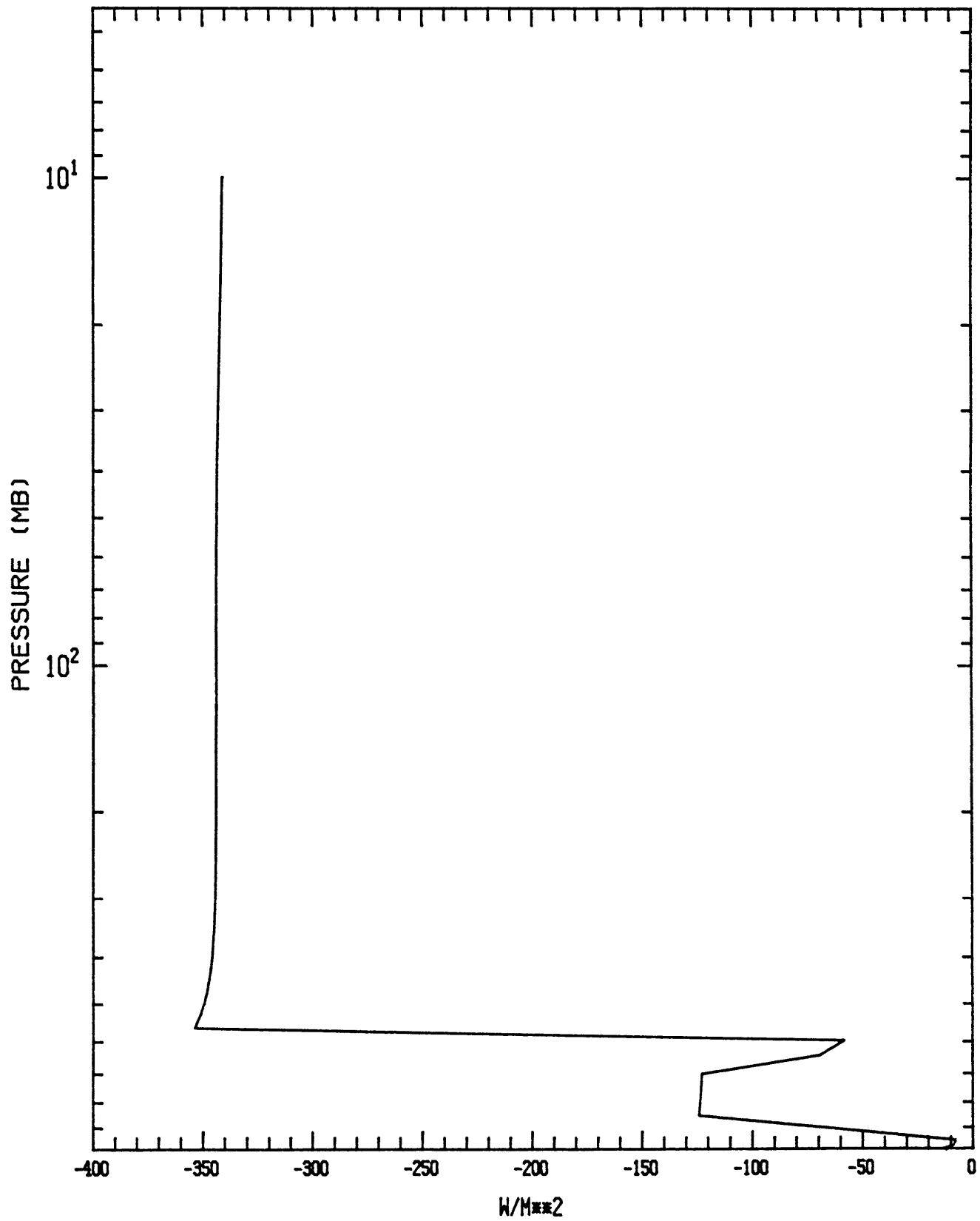
Pressure mb (x 10): 02/03/87



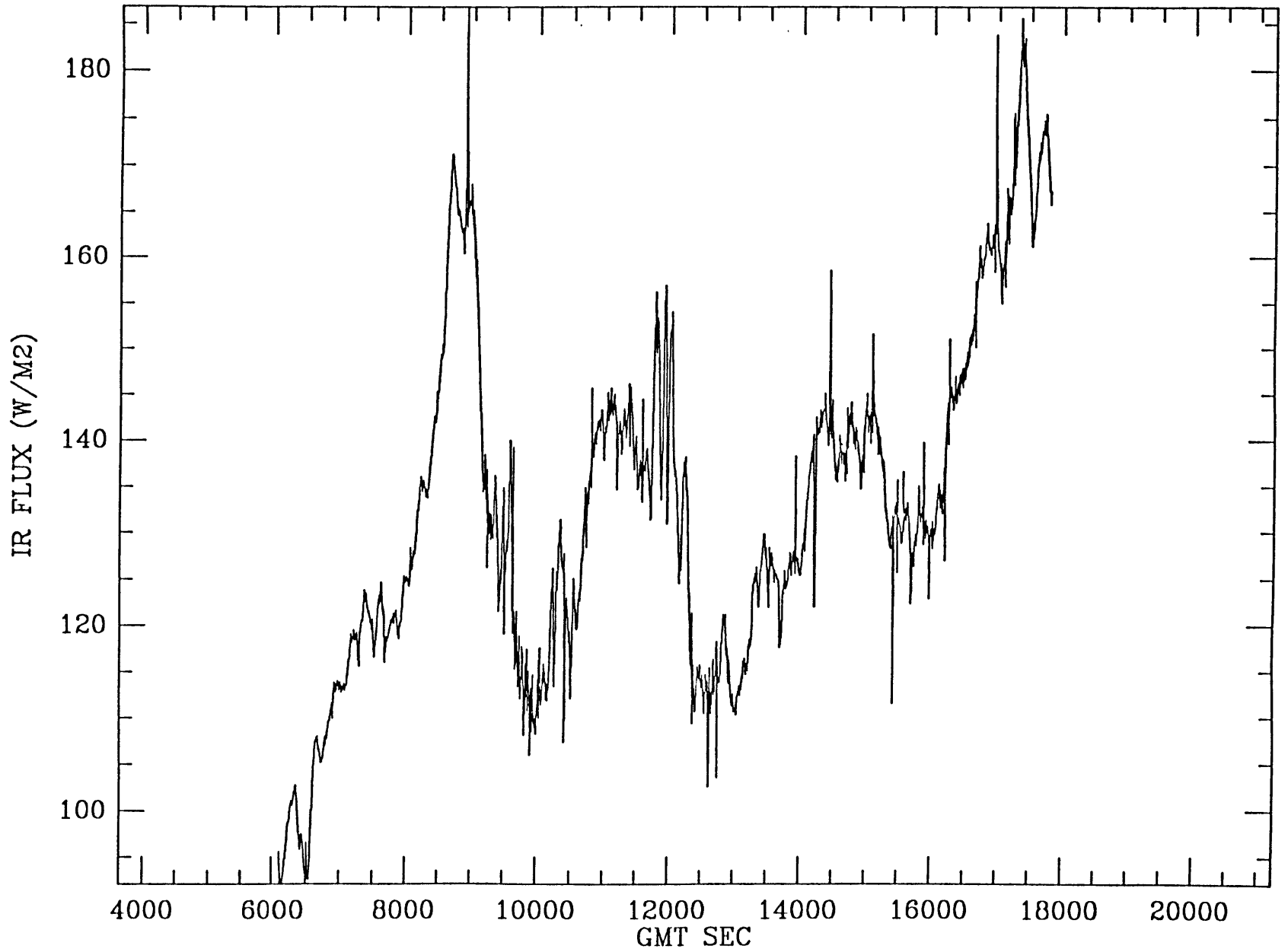
NET FLUX
94150 GØVE 08 FEB 00Z FLIGHT 12
THERMAL FLUX



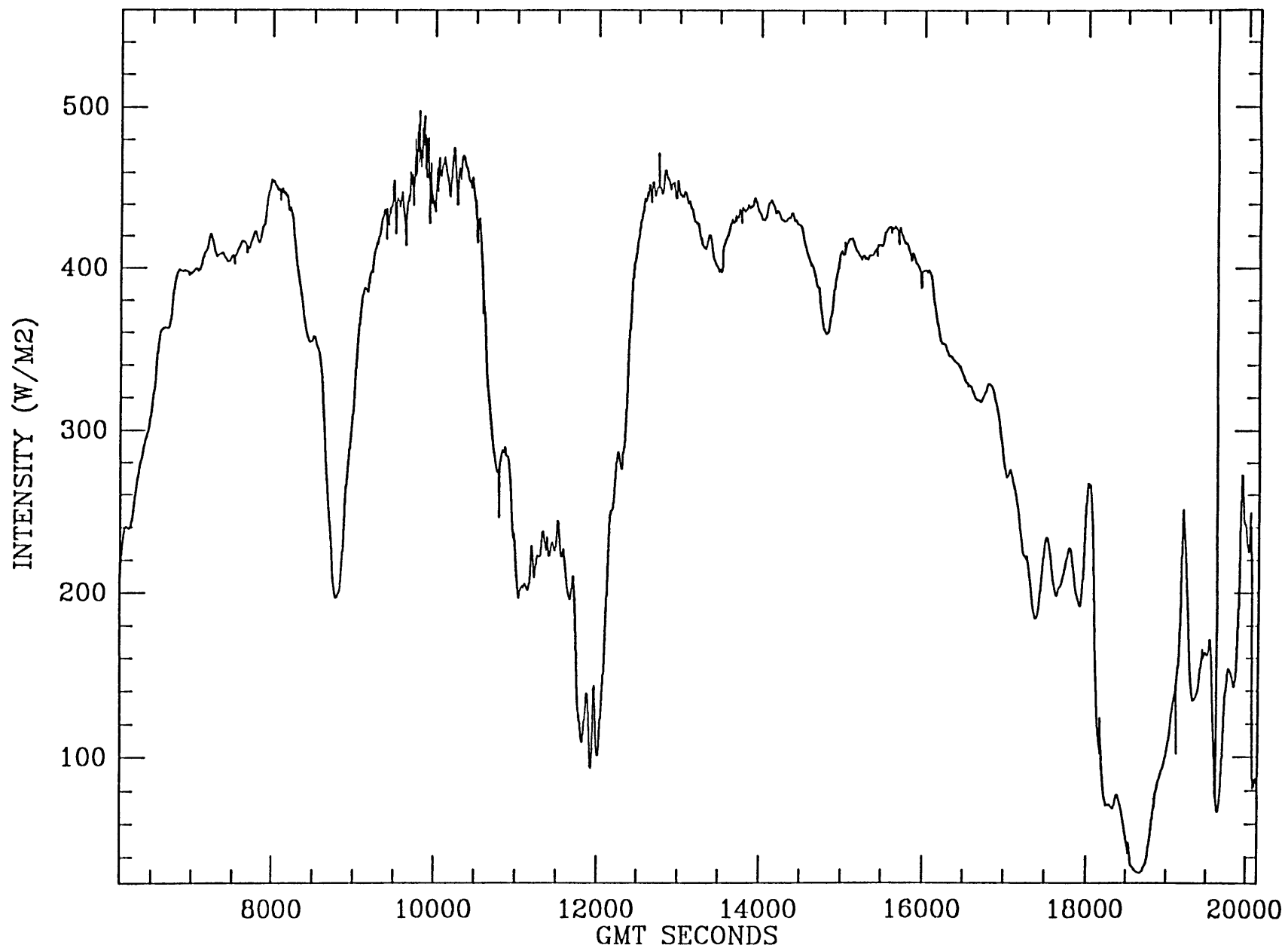
UPWELLING SOLAR FLUX
94150 GØVE 08 FEB 00Z FLIGHT 12
SØLAR FLUX



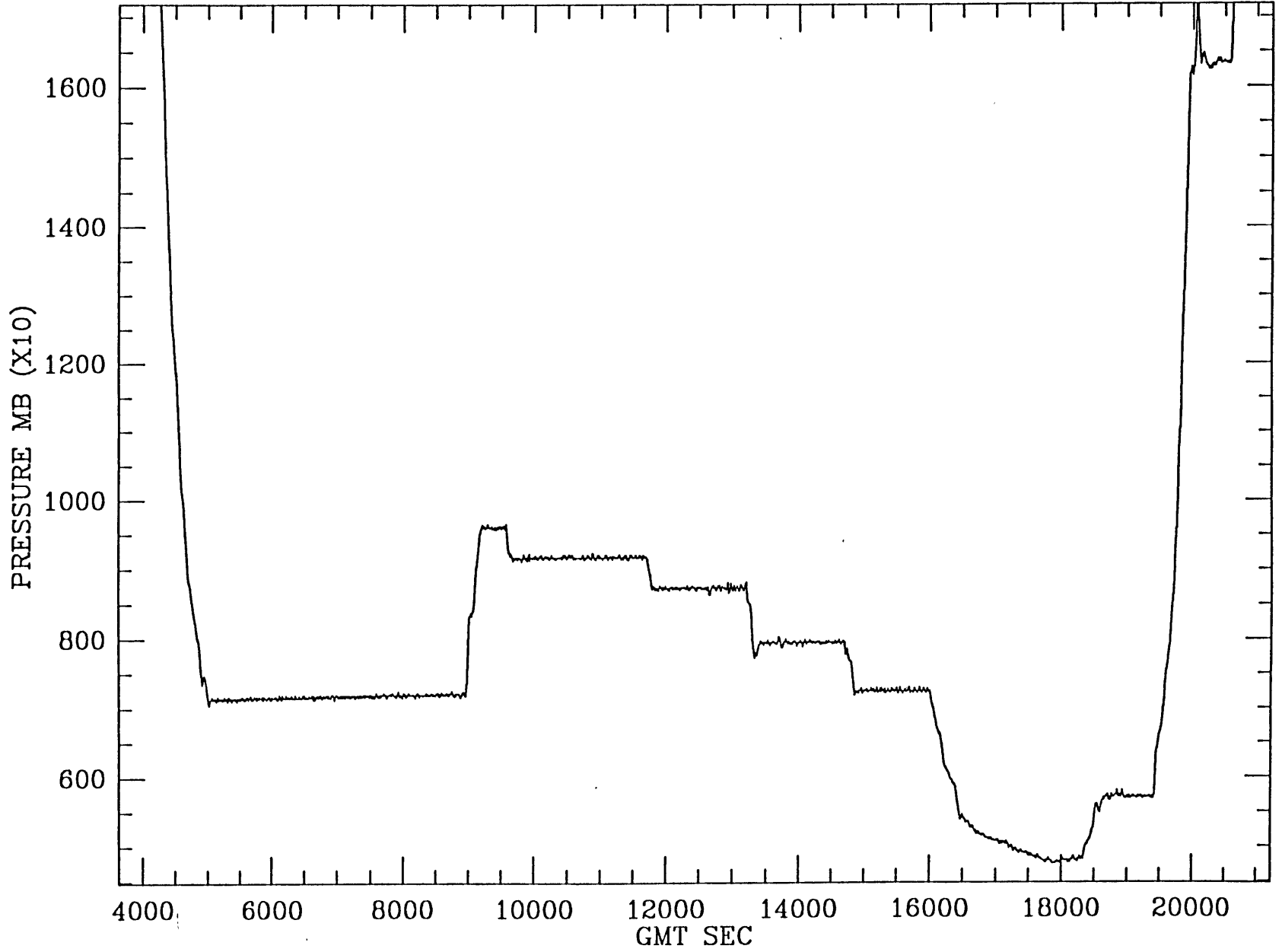
STEP <I> flight 12 NET UPWEL. IR FLUX: 02/08/87



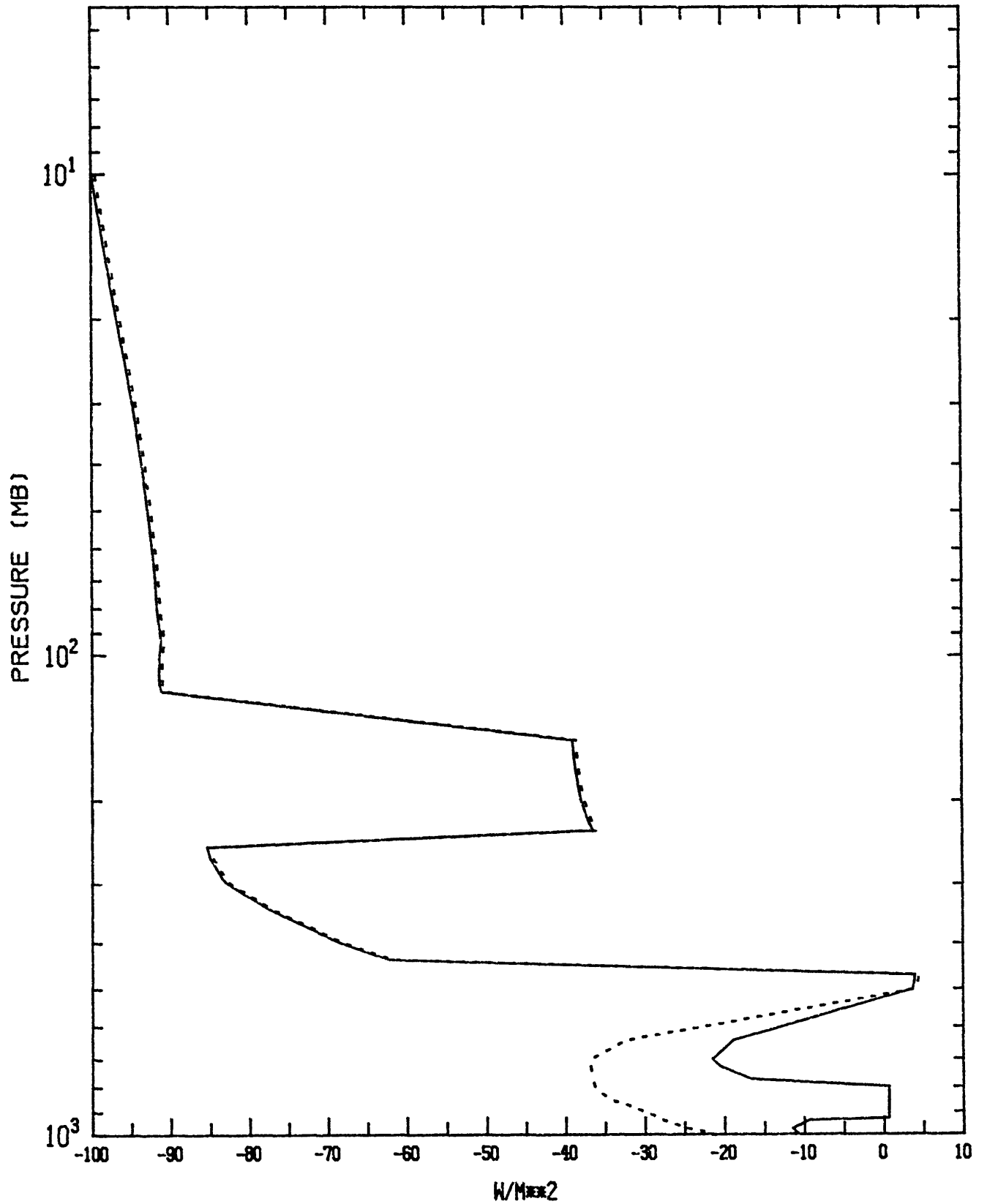
STEP FLIGHT 12 (2/8/87) - UPWELLING SOLAR FLUX



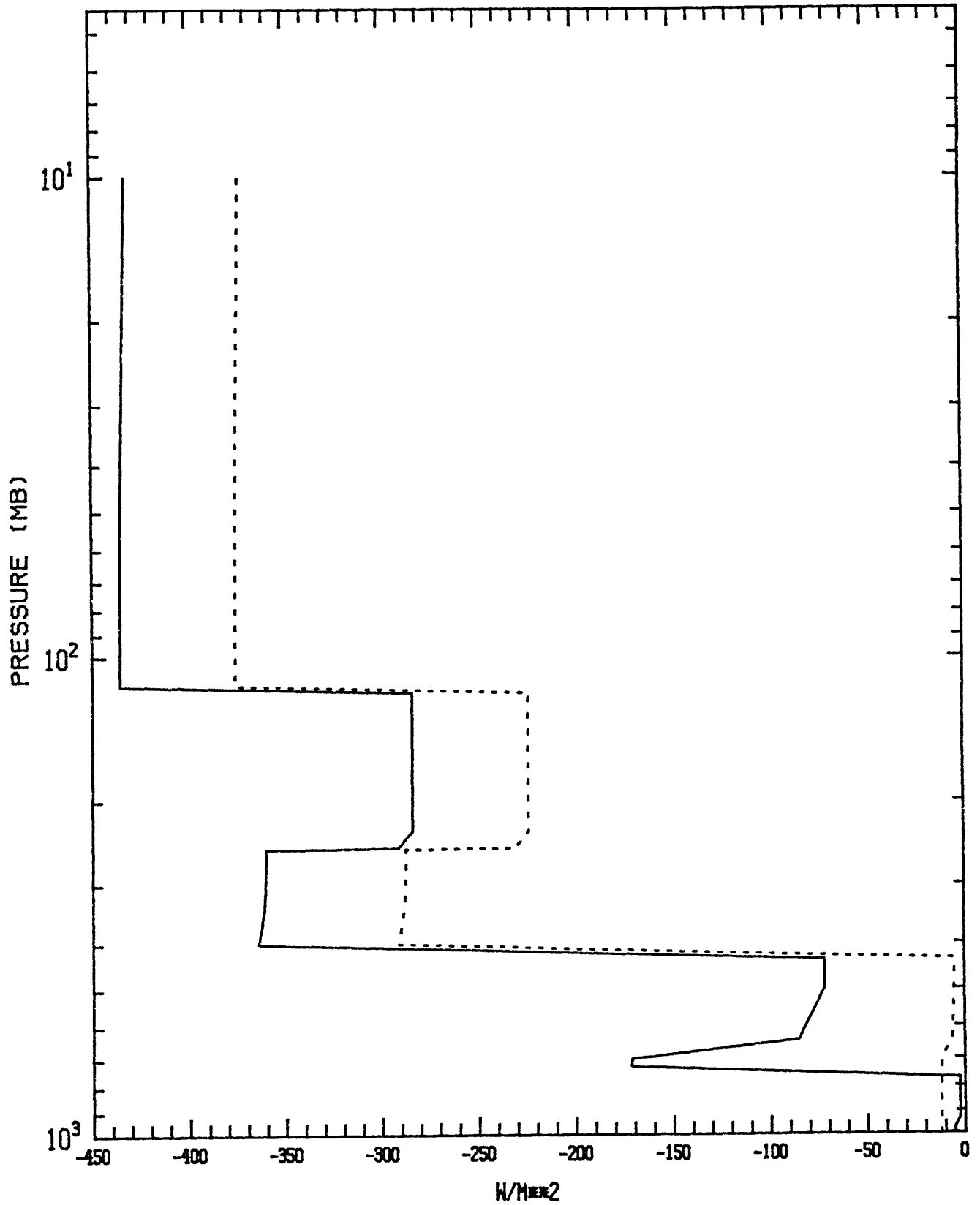
Pressure mb (x 10): 02/08/87



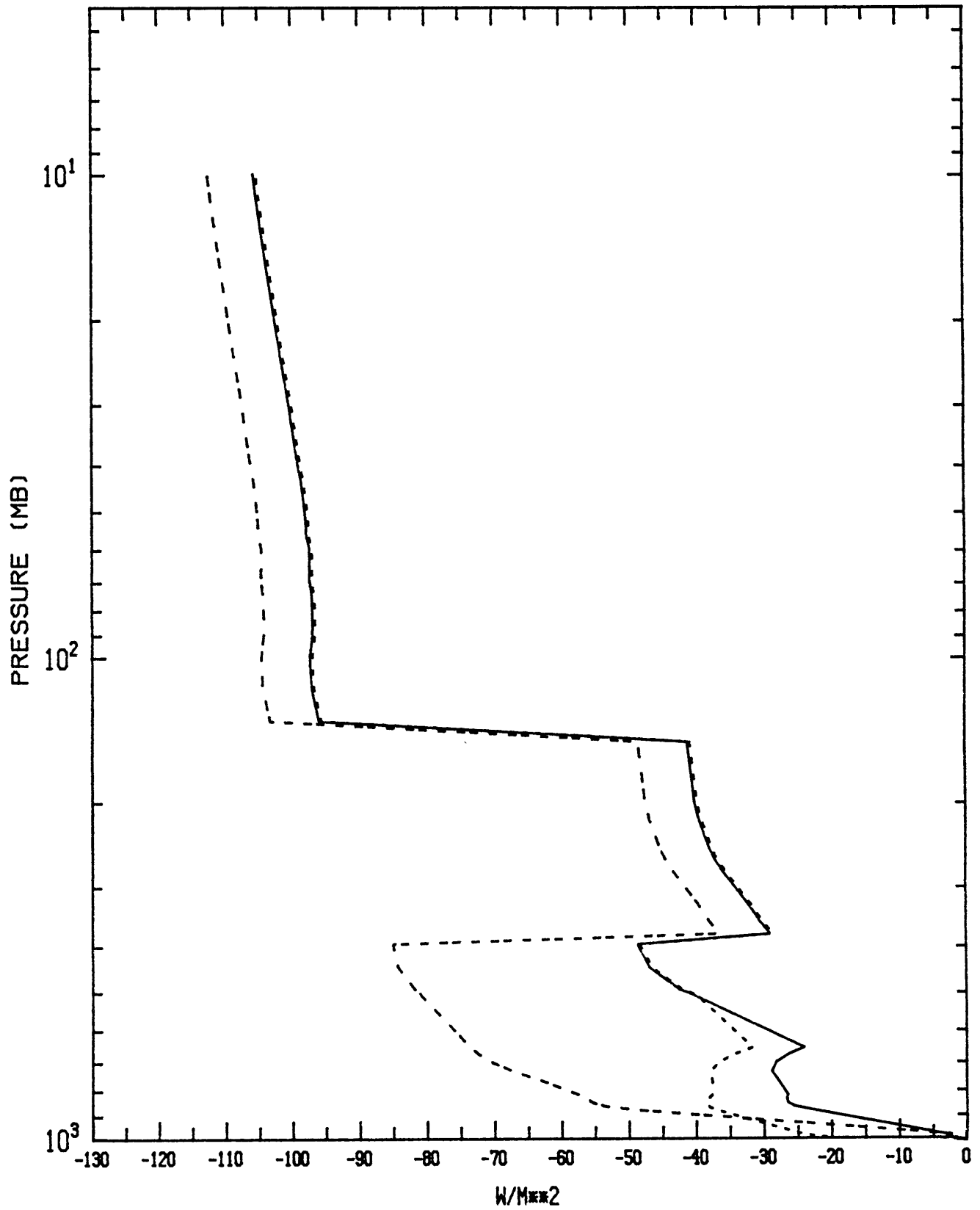
NET FLUX
94120 DARWIN 31 JAN 00Z FLIGHT 9
THERMAL FLUX OBTAINED USING TWO POSSIBLE CLOUD PROFILES



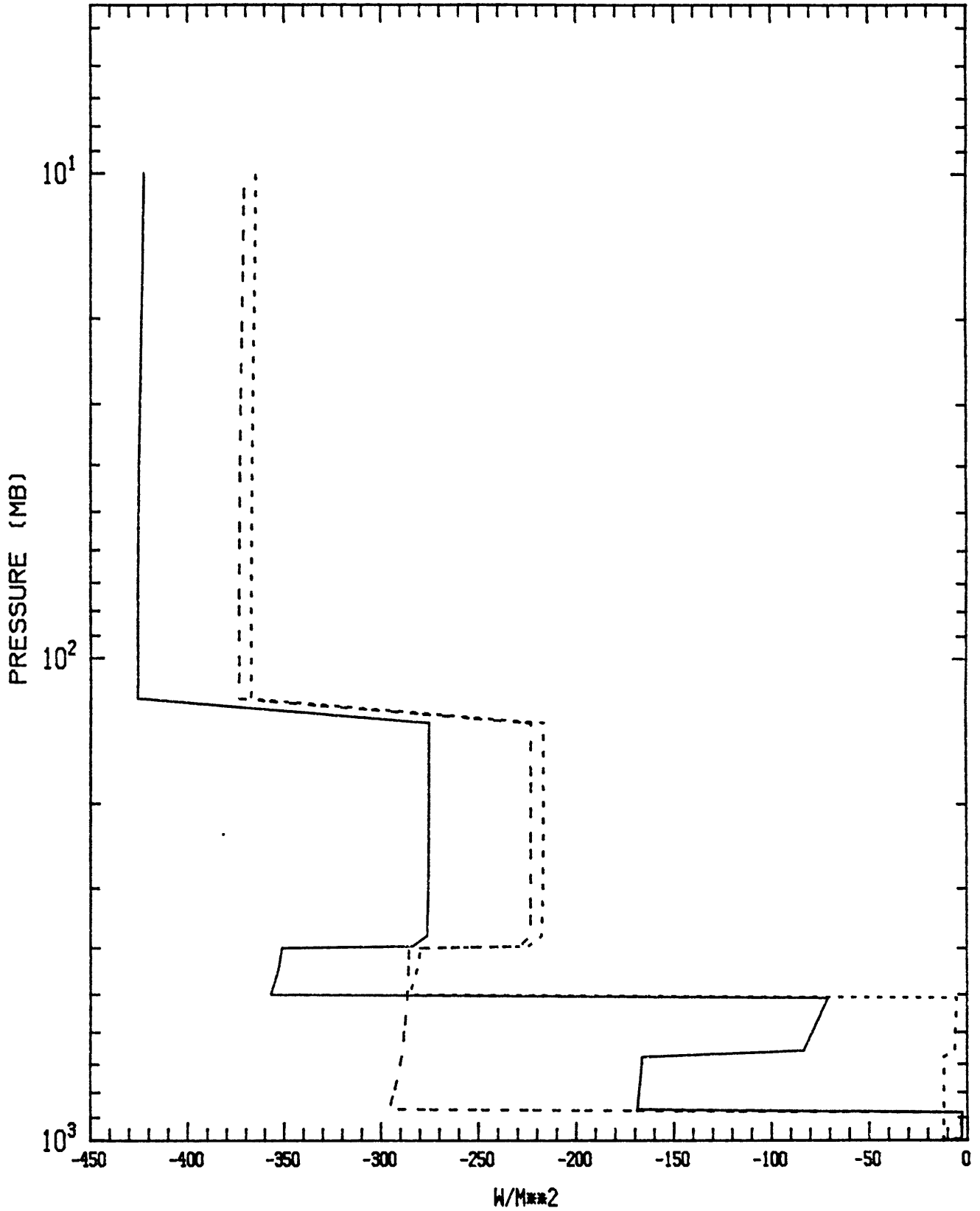
UPWELLING SOLAR FLUX
94120 DARWIN 31 JAN 00Z FLIGHT 9
SOLAR FLUX OBTAINED USING TWO POSSIBLE CLOUD PROFILES



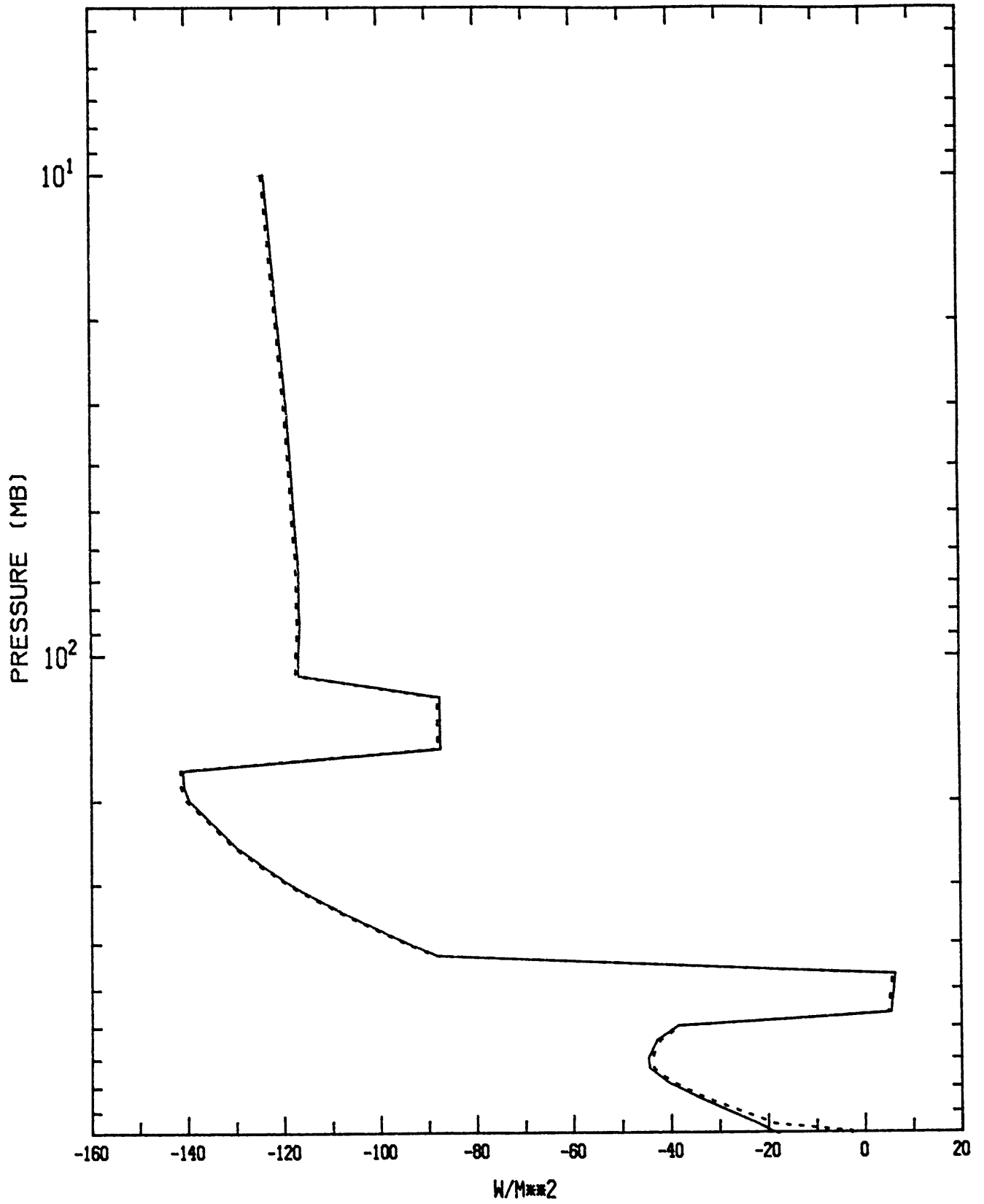
NET FLUX
94150 GØVE 03 FEB 00Z FLIGHT 10
THERMAL FLUX ØBTAINED USING THREE POSSIBLE CLØUD PRØFILES



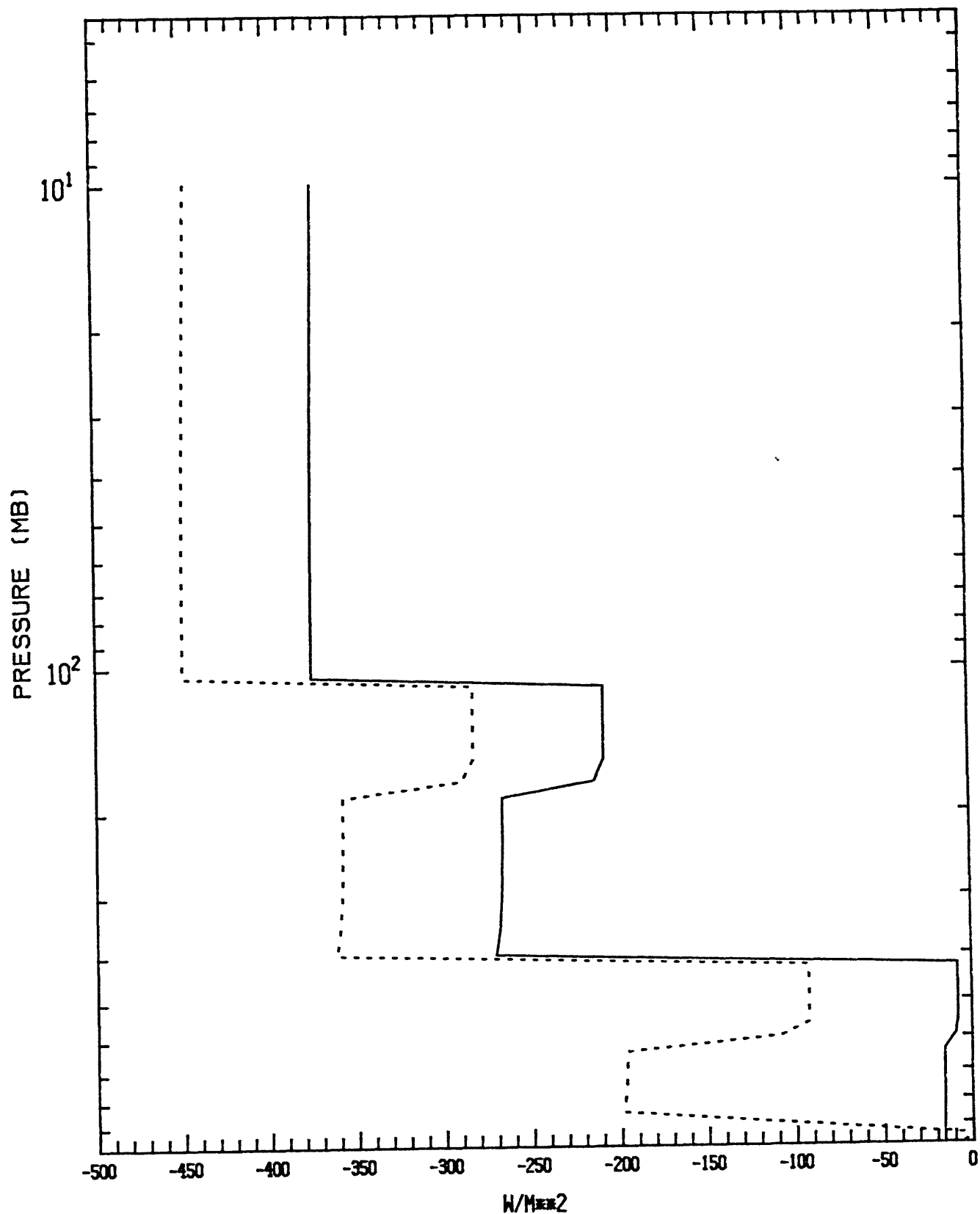
UPWELLING SOLAR FLUX
94150 GØVE 03 FEB 00Z FLIGHT 10
SØLAR FLUX ØBTAINED USING THREE PØSSIBLE CLØUD PRØFILES



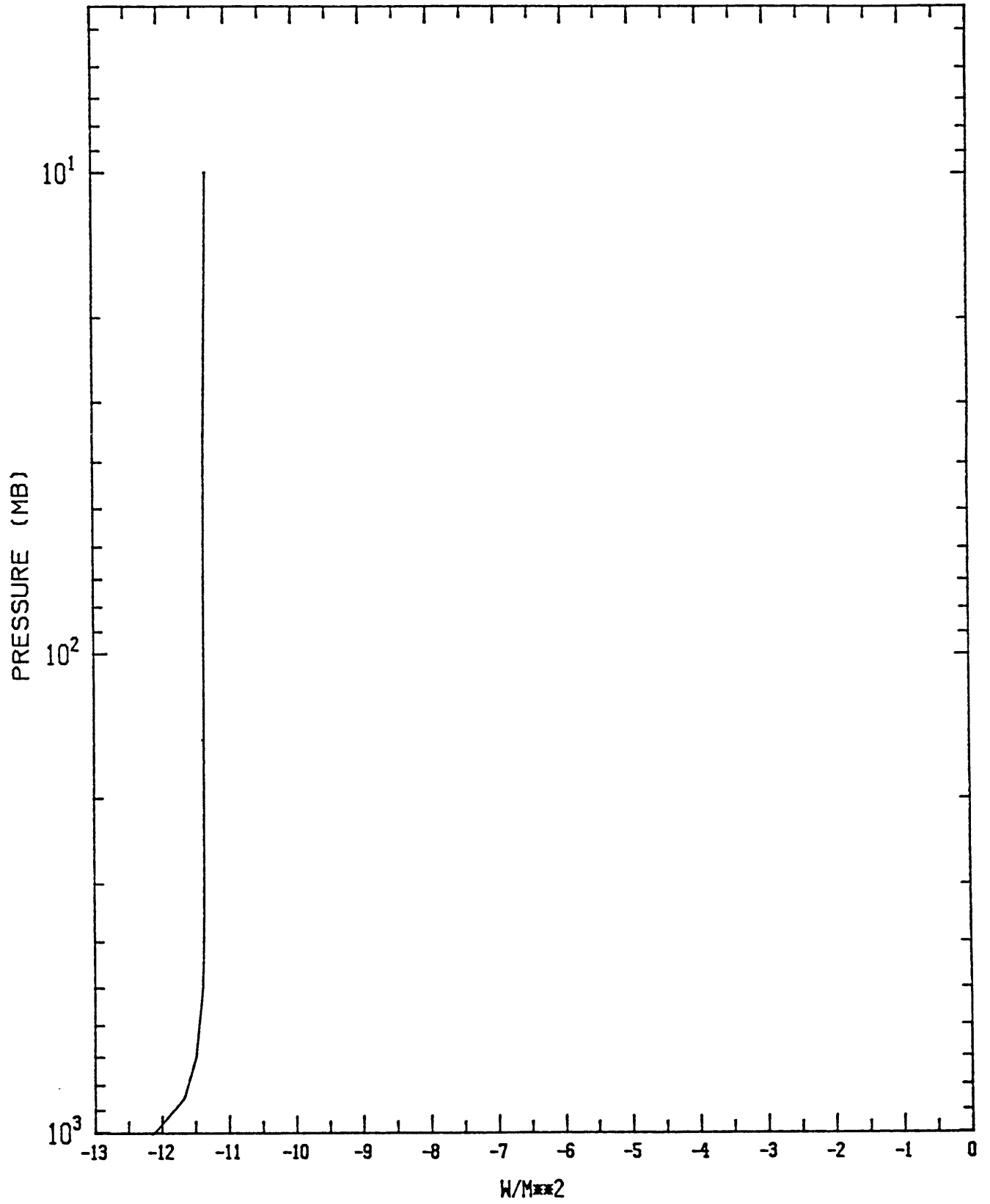
NET FLUX
94150 GØVE 08 FEB 00Z FLIGHT 12
THERMAL FLUX ØBTAINED USING TWO POSSIBLE CLØUD PRØFILES



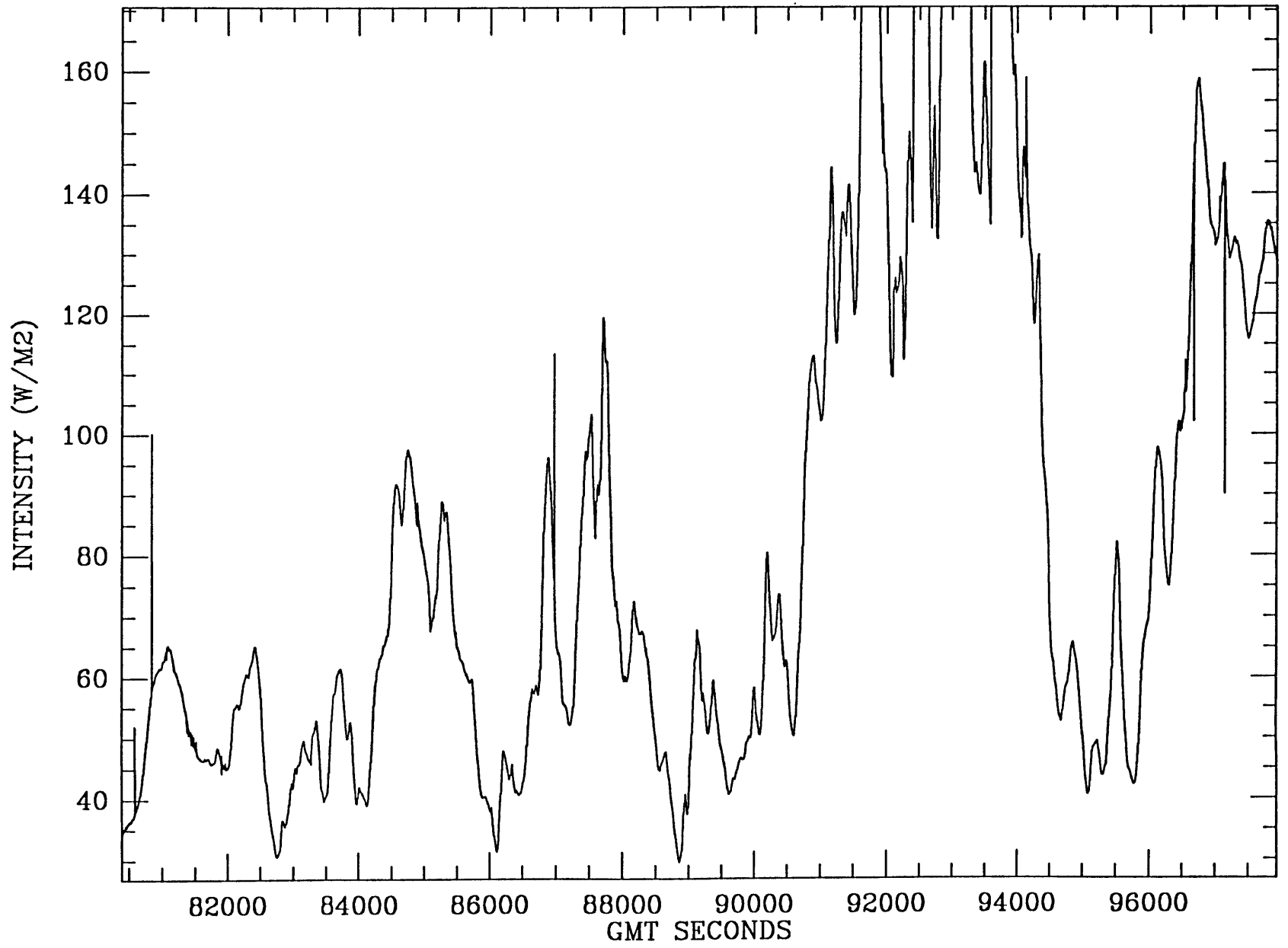
UPWELLING SOLAR FLUX
94150 GØVE 08 FEB 00Z FLIGHT 12
SØLAR FLUX ØBTAINED USING TWO POSSIBLE CLØUD PRØFILES



UPWELLING SOLAR FLUX
01139 CHINESE SHIP 24 JAN 00Z FLIGHT 7
SOLAR FLUX



STEP FLIGHT 7 (1/24/87) - UPWELLING SOLAR FLUX



7. Concluding remarks

The model gives reasonable values for thermal infrared and upwelling solar fluxes in a cloudy atmosphere. The fine structure due to small-scale variations in cloud amounts and properties cannot be reproduced because of the one-dimensional character of the model, but this is not necessary for assessment of radiative balances based on zonally or globally averaged climatological data.

Clouds are radiatively important, yet they are poorly reported in the data and poorly modeled by the computer program. This is a greater problem with the solar spectral region than the infrared, since clouds are considered black bodies in the latter case but partial reflectors in the former. Thin clouds and cirrus may be far from black, however. Because only one comparison is for a cloudless sky, the results must be interpreted with caution. The real performance of the model (e.g. aptness of the assumption of no scattering, or accuracy of the band approximations to real absorption spectra) needs to be determined by a comparison in a cloudless atmosphere.

If one were designing an experiment for the sole purpose of a radiation intercomparison, one would want the measurements of all quantities required by the model to be made from the same platform as the radiation measurements. These measurements would also ideally be made at many levels, in as close to a vertical profile as possible. This would suggest a balloon-borne experiment, such as the one described by Suomi et al. (1958). In addition, a particle counter, such as the Knollenberg instrument which was aboard the ER-2, could provide information about cloud heights and water content. Measurements should be made under as many different conditions

as possible; over land and water, in all seasons, and in arid as well as moist climates. Cloudless days would provide data for evaluation of the basic radiative transfer code, while data from cloudy days would be used to assess the cloud algorithm. The various radiative transfer models could be tested against this data set in order to determine the reasons for the differences found between their results.

The major problem with this "ideal experiment" is that broadband flux measurement errors are too large. In the present study, for example, the uncertainty in the longwave radiation measurements is larger than the spread between the lowest and highest computed values from models in the ICRCCM comparison for net flux at the tropopause in a tropical atmosphere. The expected error in the solar measurements is even larger. Although broadband radiometers are theoretically accurate to 5%, operational errors are generally larger (Albrecht and Cox, 1977).

This points to the same conclusions reached by the ICRCCM workers. On the one hand, it is important that radiative transfer models be tested against measured values of radiative flux in the atmosphere, since comparison of results from many models which use essentially the same algorithms shows a large spread in values. Even very detailed models can not claim to be absolutely correct, as the exact absorption line shapes are not always known. On the other hand, the accuracy of measured fluxes is not sufficient to test these models. For these reasons, the ICRCCM recommendation was to measure spectral radiances at high spectral resolution, which can be done with much higher accuracy than broadband measurements (Luther et al, 1988), and compare these with computed values. A

carefully planned, dedicated observing program, which tests the radiation models under a wide range of conditions, should be able to assess the accuracy of current models and resolve the discrepancies among them.

Acknowledgements

I would like to acknowledge the following people for providing the data used in this paper:

Dr. Francisco Valero, Dr. Philip Hammer, and the rest of the radiometer team (NASA Ames Research Center, Moffett Field, CA) for the radiometer data, and for the information about the radiometer characteristics;

Mr. Roger Atkinson (Bureau of Meteorology, Melbourne, Australia) for the ozonesonde data;

Dr. Roland Chan (NASA Ames Research Center) for the temperature and pressure data from the ER-2;

Dr. Ken Kelly (NOAA Aeronomy Laboratory, Boulder, CO) for the humidity data from the ER-2;

Dr. Lenny Pfister (NASA Ames Research Center) for the satellite photographs and flight track information;

Dr. Mike Proffitt (NOAA Aeronomy Laboratory) for the ozone data from the ER-2, and also for the plots which were used to get the ozone, temperature, and water vapor measurements from the ER-2.

Participation in the STEP program was funded by NASA under grant NAGW-703. This thesis was written while the author was supported by NASA Ames University Consortium Joint Research Interchange NCA2-327.

References

- Ackerman, T. P., Liou, K.-N., Valero, F. P. J., and L. Pfister, 1988: Heating rates in tropical anvils. J. Atmos. Sci. **45**, 1606-1623.
- Albrecht, B., and S. K. Cox, 1977: Procedures for improving pyrgeometer performance. J. Appl. Meteor., **16**, 188-197.
- Brewer, A. W. and J. T. Houghton, 1956: Some measurements of the flux of infra-red radiation in the atmosphere. Proc. Roy. Soc. (A) **236**, 175-186.
- Danielsen, E. F., 1982: A dehydration mechanism for the stratosphere. Geophys. Res. Lett., **9**, 605-608.
- Doherty, G. M., Newell, R. E., and E. F. Danielsen, 1984: Radiative heating rates near the stratospheric fountain. J. Geophys. Res. **89**, 1380-1384.
- Dopplick, T. G., 1970: Global radiative heating of the earth's atmosphere. Report no. 24, Planetary Circulations Project, Department of Meteorology, MIT, Cambridge, Mass., 128 pp.
- Dopplick, T. G., 1972: Radiative heating of the global atmosphere. J. Atmos. Sci. **29**, 1278-1294.
- Hoffman, R. N., 1981: A computer program which calculates radiative fluxes and heating rates in model atmospheres. Sci. Report no. 4, Department of Meteorology and Physical Oceanography, MIT, Cambridge, Mass., 124 pp.
- Houghton, H. G., 1985: Physical Meteorology. MIT Press, Cambridge, Mass., 442 pp.
- Hummel, J. R., Shelton, C. M., and S. T. Hanley, 1985: Field test evaluation of Vaisala Marwin/Digicora and Beukers W-8000 upper air systems, Volume I: Test results and analysis. US Army Atmospheric Sciences Laboratory, White Sands Missile Range, New Mexico, 73 pp.

- Kennedy, J. S., 1964: Energy generation through radiative processes in the lower stratosphere. Report no. 11, Planetary Circulations Project, Department of Meteorology, MIT, Cambridge, Mass., 116 pp.
- Kondratyev, K. Ya., 1969: Radiation in the Atmosphere, Academic Press, New York, 912 pp.
- London, J., and T. Sasamori, 1971: "Radiative energy budget of the atmosphere," in Man's Impact on the Climate, W. H. Matthews, W. W. Kellog, and G. D. Robinson, eds., MIT Press, Cambridge, Mass., pp. 141-155.
- Luther, F. M., Ellingson, R. G., Fouquart, Y., Fels, S., Scott, N. A., and W. J. Wiscombe, 1988: Intercomparison of Radiation Codes in Climate Models (ICRCCM): Longwave clear-sky results -- a workshop summary. Bull. Amer. Meteor. Soc. **69**, 40-48.
- Manabe, S. and R. T. Wetherald, 1967: Thermal equilibrium of the atmosphere with a given distribution of relative humidity. J. Atmos. Sci. **24**, 241-259.
- Newell, R. E., and T. G. Dopplick, 1970: The effect of changing CO₂ concentration on radiative heating rates. J. Appl. Meteor. **9**, 958-959.
- Payne, R. E., 1972: Albedo of the sea surface. J. Atmos. Sci. **29**, 959-970.
- Platt, C. M. R., 1976: Infrared absorption and liquid water content in stratocumulus clouds. Q. J. Roy. Meteor. Soc. **102**, 553-562.
- Rodgers, C. D., 1967: The radiative heat budget of the troposphere and lower stratosphere. Report no. A2, Planetary Circulations Project, Department of Meteorology, MIT, Cambridge, Mass., 99 pp.
- Rodgers, C. D., 1968: Some extensions and applications of the new random model for molecular band transmission. Q. J. Roy. Meteor. Soc. **94**, 99-102.

Rodgers, C. D., and C. D. Walshaw, 1966: The computation of infrared cooling rate in planetary atmospheres. Q. J. Roy. Meteor. Soc. **92**, 67-92.

Walshaw, C. D., and C. D. Rodgers, 1963: The effect of the Curtis-Godson approximation on the accuracy of radiative heating-rate calculations. Q. J. Roy. Meteor. Soc. **86**, 122-130.